Generation and characterization of short-duration and high-brightness laser-driven neutron sources

Laura Vassura

SAPIENZA
UNIVERSITÀ DI ROMA

Thèse de doctorat

Discipline: Physique

Présentée à l'Ecole Polytechnique pour obtenir le grade de

DOCTEUR DE L'ECOLE POLYTECHNIQUE

par

Laura VASSURA

Generation and characterization of short-duration and high-brightness laser-driven neutron sources

Soutenance publiquement le 4 Décembre 2015
devant le Jury composé de:

Stefano ATZENI	Rapporteur
Franck GOBET	Rapporteur
François AMIRANOFF	Examinateur
Dimitri BATANI	Examinateur
Erik LEFEBVRE	Examinateur
Patrick MORA	Examinateur
Julien FUCHS	Directeur de thèse
Luigi PALUMBO	Directeur de thèse

Contents

Preface

The work presented in this thesis has been performed within a "cotutela" agreement between the *Laboratoire pour l'Utilisation des Lasers Intenses* (LULI) of the *Ecole Polytechnique* and the department of *Scienze di Base e Applicate per l' Ingegneria* (SBAI) of *Sapienza*, University of Rome. It has been mainly funded by a DGA-MRIS scholarship.

For many aspects, the research topic was new both for the LULI laboratory and the SBAI department, and it has permitted the creation of close and fruitful collaborations with other research groups: the CENBG in Bordeaux, the Institute of Atomic Physics (IFIN-HH) of Bucharest-Magurele and the Queen's University of Belfast. Therefore, the work presented here is the result of the effort of all these collaborators and it could not have been realized without their contribution.

I have personally contributed to the planning and the implementation of both experimental campaigns presented in this manuscript, as well as to a partial analysis of the data (in particular for the micro lens device).

This work was an experimental investigation on the possibility to generate and modify a laser driven neutron source. Therefore, the manuscript contains topics of nuclear physics, as well as plasma physics and particle acceleration. The majority of these topics were completely new for me. Even if I did not have a solid background in plasma physics or nuclear physics, I hope I have presented this project in a clear and interesting way, also to spotlight all the fruitful work realized by my collaborators.

As in every new path, initial difficulties arose like a barrier at the entry of the new scientific investigation. Many detectors have been tested for the first time in new experimental conditions and not all of them worked as expected, innovative set-ups have been tried, but not all with the results desired, and unexpected problems arose along the way. The first campaign at ELFIE had to be postponed and we lost three weeks of experimental time out of five. Due to the US government shutdown in 2013 that blocked all the US national laboratories, we lost one week out of five in the second campaign at TITAN. With fewer unexpected

events, the work presented here would have answered to more questions. Nevertheless, new results have been achieved [Higginson *et al.*, 2015] and it seems to me that interesting perspectives have been opened by our investigation.

Due to the deferment of the neutron experiments, I worked for half of my PhD on completely different subjects. I contributed to the studies on stimulated Brillouin backscattering for laser-plasma interaction in the strong coupling regime. I participated in two experimental campaigns (5 weeks each) and to the analysis of the experimental data. Although it has been part of my PhD job during these years, all this work and the results achieved are not included in this manuscript [Lancia *et al.*, 2015].

Collaborations with external groups have given me the opportunity to participate in additional experimental laser campaigns. I worked on proton acceleration from micro-structured grating targets [Ceccotti *et al.*, 2013], [Sgattoni *et al.*, 2013] and micro-sphere layered targets [Floquet *et al.*, 2013], on the characterization of deuterium spectra from laser driven multi-species sources [Alejo *et al.*, 2013], on selective deuterium ion acceleration [Krygier *et al.*, 2015], and on the calibration of time of flight detectors using laser-driven neutron sources [Mirfayzi *et al.*, 2015].

This manuscript is composed of three main chapters plus a final chapter of conclusions and perspectives.

The first chapter is a very general introduction on the two main topics of this thesis: neutron sources and laser-accelerated proton beams.

In the second chapter I introduce the concept that has inspired our experimental investigation and I describe all the diagnostics used during the experiments.

Finally, in the third chapter I present the two experiments carried out at ELFIE and at TITAN. I detail the analysis that we performed and I discuss the results that we obtained.

Chapter 1

Introduction

Abstract This first chapter is a general introduction on the topics discussed in the thesis. The first section gives the reader a brief overview of the principal characteristics of neutrons, showing some of their properties and possible applications. The second section presents the principal types of neutron sources currently used and the third section introduces the concept of a laser driven neutron source, with all the possible approaches exploitable to produce neutrons using a high-intensity laser pulse. Since using lasers constitutes one of the more promising methods for producing bright and short duration neutron sources, the current framework of ion acceleration based on laser-plasma interaction is discussed in the last section.

1.1 Introduction to the Neutron

Discovery

The neutron is a subatomic particle with many unique attributes that make it very attractive for research. Even though it is one of the fundamental constituents of the atom, the discovery of the neutron occurred well after the discovery of the electron, by J. J. Thomson in 1897, and of the proton, theorized by William Prout in 1815 and discovered by Ernest Rutherford in 1917–1919. In 1920 for the first time Rutherford proposed a close combination of an electron and a proton forming a neutral doublet, which he postulated would have novel properties including the ability to move freely through matter, be difficult to detect, and perhaps impossible to contain in a vessel [Rutherford 1920].

In 1931 in Germany, Walther Bothe and Herbert Becker found that if the very energetic alpha particles emitted from polonium fell on certain light elements,

specifically beryllium, boron, or lithium, an unusually penetrating radiation was produced. At first this radiation was thought to be gamma radiation, although it was more penetrating than any gamma ray known, and the details of the experimental results were very difficult to interpret on this basis.

It was James Chadwick that in 1932, while performing a series of experiments at the University of Cambridge, showed that the gamma ray hypothesis was untenable and suggested that the new radiation consisted of uncharged particles of approximately the mass of the proton. Chadwick was awarded the 1935 Nobel Prize in Physics "for his discovery of the neutron". In the same year, the first experiment in neutron radiography was carried out by H. Kallamann and E. Kuhn.

Throughout the later half of the 20th century, particle physicists have developed the Standard Model and, until now, a wide variety of experimental results have confirmed the validity of this model. According to the Standard Model, the neutron is defined as a hadron of the family of baryons, as a composite subatomic particle made up of three quarks. The proton belongs to the same family of the baryons. Protons and neutrons make up most of the mass of the visible matter in the universe, and they differ from each other only for the flavour of the quarks composing them[1]. A neutron is composed of one up (+2⁄3) quark and two down (-1/3) quarks resulting in a null charge, while the proton is composed of two up quarks and one down quark resulting in a +1 charge. Quarks can change flavour via the weak interaction force, therefore a neutron can decay into a proton (p^+), an electron (e^-) and an electron antineutrino ($\overline{\nu_e}$):

$$n \longrightarrow p^+ + e^- + \overline{\nu_e}\,. \tag{1.1}$$

This process, named beta minus decay, can take place in the nucleus and allows the atom to move closer to the optimal ratio of protons and neutrons. Outside the nucleus, free neutrons are unstable and undergo β^- decay with a half-life of about 10 minutes.

Classification of neutrons

One of the topics of this thesis is the study of a neutron source, i.e. it is concerned with free neutrons that move in space. Such neutrons are usually classified according to their kinetic energy, as shown in Table 1.1.

[1] The model counts six flavours of quark named up (u), down (d), strange (s), charm (c), bottom (b), and top (t). Depending on its flavour, a quark can have fractional electric charge values either -1⁄3 or +2⁄3 times the elementary charge.

Neutron classification	Energy Range	Velocity (m/s)	λ (nm)
Cold	< 0.025 eV	< 2200	< 0.18
Thermal	0.025 eV	2200	0.18
Slow neutrons	1 – 10 eV	[1.38 10^4 - 4.37 10^4]	[0.03 - 0.01]
Fast neutrons	1 – 20 MeV	[1.38 10^7 - 6.18 10^7]	[3 10^{-5} – 6 10^{-6}]
Relativistic neutrons	> 20 MeV	> 6.18 10^7	> 6 10^{-6}

Table 1.1 *Neutron classification.*

The kinetic energy[2] E, of a neutron is given by $mv^2/2$, which is conventionally related to a temperature via the *Boltzmann constant*, $k_B = 1.381\times10^{-23}\ JK^{-1}$, according to the equation:

$$E = \frac{mv^2}{2} = k_B T\,. \tag{1.2}$$

Knowing the neutron velocity, it is possible to define its *de Broglie wavelength*[2], another important parameter that characterizes the neutron behaviour. The de Broglie wavelength, in units of nm, is given by:

$$\lambda_{[nm]} = \frac{h}{m_n v}\times10^9 = \frac{395.6}{v}\,. \tag{1.3}$$

Where $h = 6.6261\times10^{-34}\ m^2kg\ s^{-1}$ is *Planck's constant*, m_n is the mass of neutron equal to $1.6749\times10^{-27}\ kg$ and v is the neutron velocity in m/s. Thermal neutrons correspond for example to a room temperature of 20°C, with a velocity of 2200 m/s and a wavelength approximately equal to 1.8 Å = 0.18 nm. Therefore the thermal neutrons wavelength is similar to inter-atomic distances, so mechanisms such as refraction or diffraction can be used to enhance images or to produce indirect images.

General characteristics of neutron interaction with matter

Depending on their energy, neutrons interact differently with matter. As Rutherford anticipated, because the neutron is uncharged, it interacts primarily with the nucleus rather than with the electron shell of the atoms. The likelihood of interaction between an incident neutron and a target nucleus depends on the energy of the incident neutron, the target material, the type of nuclear reaction (scattering, fission, etc.) and the relative angle between the incident neutron and the target nucleus velocity. The probability of a particular event occurring between a neutron and a nucleus is expressed through the concept of cross section.

In Figure 1.1, the types of possible interaction with a nucleus are

[2] For a non relativistic neutron velocity.

summarized. An interaction may be one of two major types: scattering or absorption. When a neutron is scattered by a nucleus, its speed and direction change but the nucleus is left with the same number of protons and neutrons it had before the interaction. The nucleus will have some recoil velocity and it may be left in an excited state that will lead to the eventual release of radiation. When a neutron is absorbed by a nucleus, a wide range of radiations can be emitted or fission can be induced.

Each type of event has its own probability and cross section. The probability of each type of event is independent of the probabilities of the others, so the total probability of any event occurring is the sum of the individual probabilities. The sum of all the individual cross sections is the *total cross section* σ_t:

$$\sigma_t = \sigma_s + \sigma_a \, . \tag{1.4}$$

Where σ_s and σ_a are the *scattering* and the *absorption cross sections*, respectively. A cross section to each interaction is associated as shown in Figure 1.1.

The scattering and the absorption cross sections for thermal neutrons as function of the atomic number are shown in Figure 1.2. For very low neutron energies, many absorption cross sections (open circles of Figure 1.2) are proportional to $1/v$.

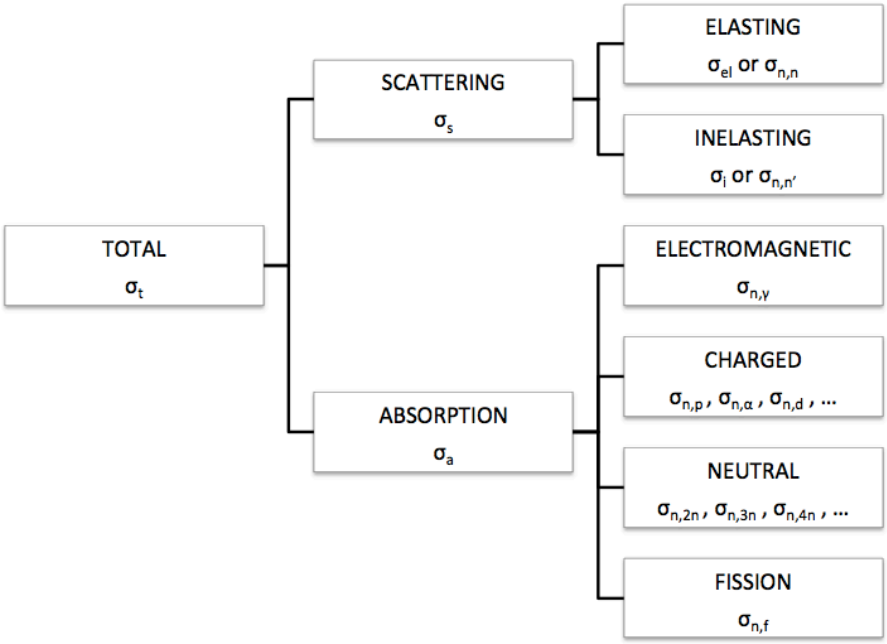

Figure 1.1 *Categories of neutron interactions with nucleus.*

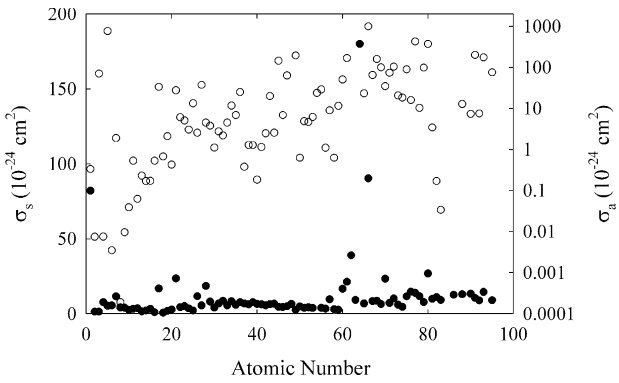

Figure 1.2 *Neutron scattering σ_s and adsorption σ_a cross section for thermal neutrons (v=2200 m/s). Open circles are adsorption cross sections and are plotted on the logarithmic scale of the right y-axis. Closed circles are the bound atom scattering cross sections plotted on the linear scale of the left y-axis. Taken from [Herwig 2009].*

To study and detect neutrons, and perform neutron applications it is important to understand the way they interact with matter. For instance a neutron detector is based on some neutron interactions with the material in the detector. Moreover, the health risk associated with neutrons is significant as they are highly penetrating and can induce secondary deep body ionizing radiation. Working with neutrons, it is important to use the appropriate shielding and limit the amount of fissile material.

As stated above, the neutron is electrically neutral and this is one of its principal and most interesting properties that, on one side, has made it so difficult to detect and discover, but on the other side, makes it also a very good candidate for probing applications, like neutron scattering and neutron imaging. Indeed, the neutron is highly penetrating and well able to investigate the interior of large assemblies, and moreover it does so non-destructively.

Unique information can be derived from the image of objects illuminated by neutrons. The amount of scattering or absorption of neutrons by atomic nuclei varies without a clear trend through the periodic table. Hydrogen in particular has a very large scattering cross section.

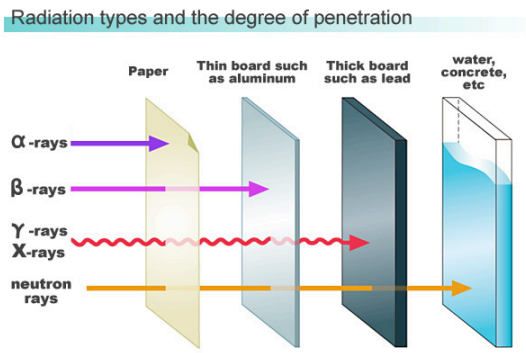

Figure 1.3 *Penetration of neutrons compared to the other radiations.*

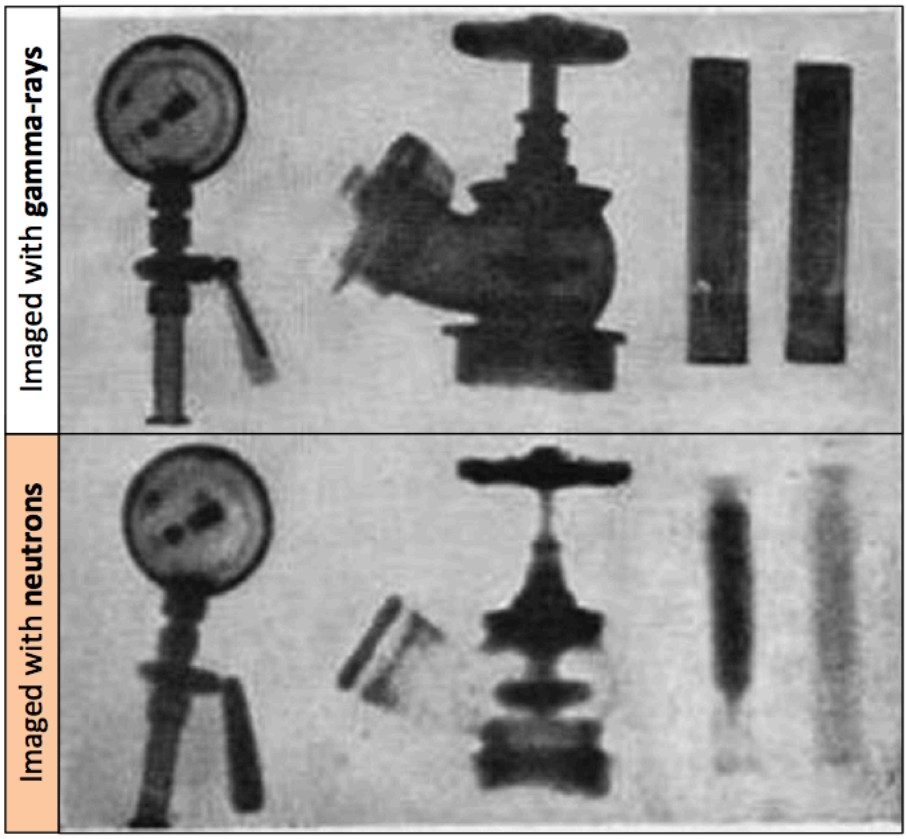

Figure 1.4 *Left to right: Pressure gauge with metal back plate; fire hydrant and test tubes filled with H_2O and D_2O imaged with gamma-rays (top) and neutrons (bottom) [Anderson, Bilheux et McGreevy 2009].*

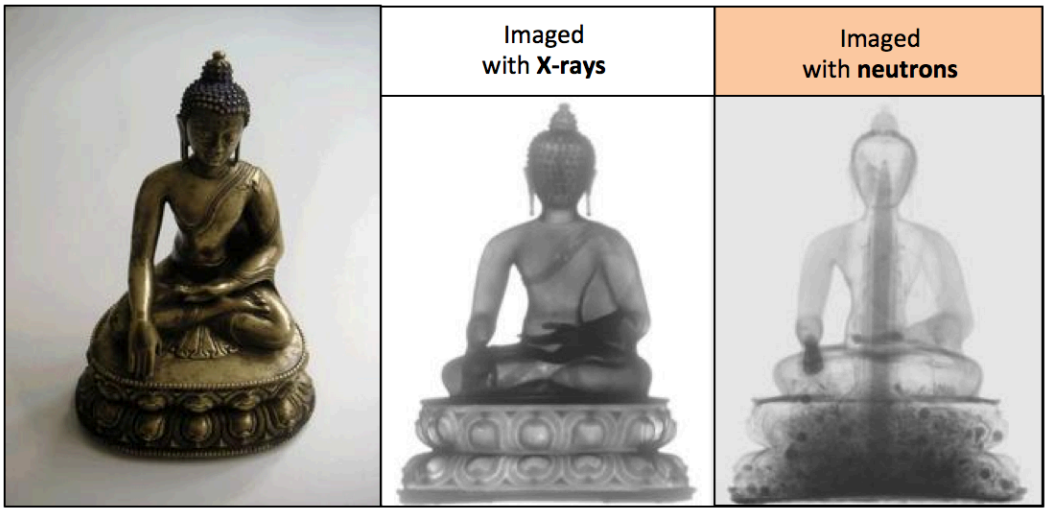

Figure 1.5 *Study of the inner content of Buddha sculptures. Photo: example of Sakyamuni, Bhumisparsa Mudra, West Tibet, 14th–15th century. The left X-ray radiography doesn't show content while the right neutron radiography provide information about the embedded organic material. Taken from [Lehmann 2010].*

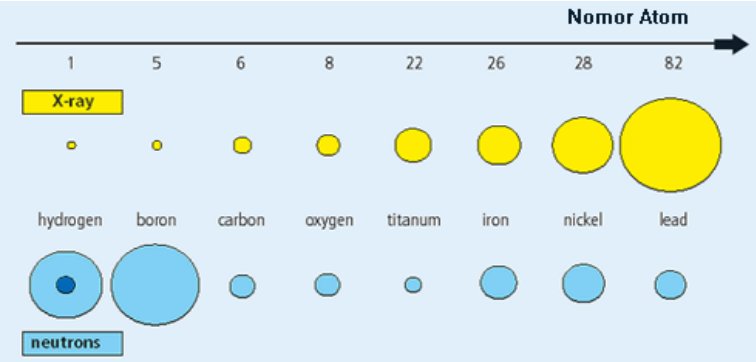

Figure 1.6 *Representation of the comparison between the neutron and X-ray cross sections.*

Therefore, neutrons can provide good contrast for light atoms in the presence of heavy atoms; this makes neutron imaging very complementary to X-ray or gamma-ray imaging, as it is shown in Figure 1.4 and Figure 1.5, and it is quite useful and interesting to combine the information derived from the two imaging systems.

Furthermore, neutrons can also distinguish between different isotopes of the same element, e.g., hydrogen has a very different scattering cross-section from its isotope deuterium. The contrast of particular elements in an image can therefore be enhanced by substituting one isotope with another. This is clearly observed in the filled tubes in Figure 1.4.

The essential difference between X-rays and neutrons may be explained as follows: X-rays interact with the atomic shell, i.e. they are scattered or absorbed by the electrons. The more electrons an element has, the more it attenuates X-rays. Neutrons, on the other hand, interact with the atomic nuclei, but show no regularity across the periodic system of elements. This interaction strongly depends on the inner structure of the atomic nuclei, and even isotopes of the same element may often provide very different levels of contrast in a projection image. The high degree of neutron scattering caused by hydrogen and the penetration capacity of neutrons for most metals are of particular industrial significance.

Obviously for all the imaging and scattering applications, the neutron cross section is a very important parameter; it determines the elements that interact more with neutrons. The visual representation of the comparison between the neutron cross section and the X-ray cross section for different atomic numbers, shown in Figure 1.6, underlines once again the better capacity of neutrons to detect light atoms, and to discern for example between hydrogen and deuterium.

Figure 1.7 shows the attenuation coefficients for various types of radiation. 120 keV X-rays exhibit obvious regularity; their attenuation is following the black

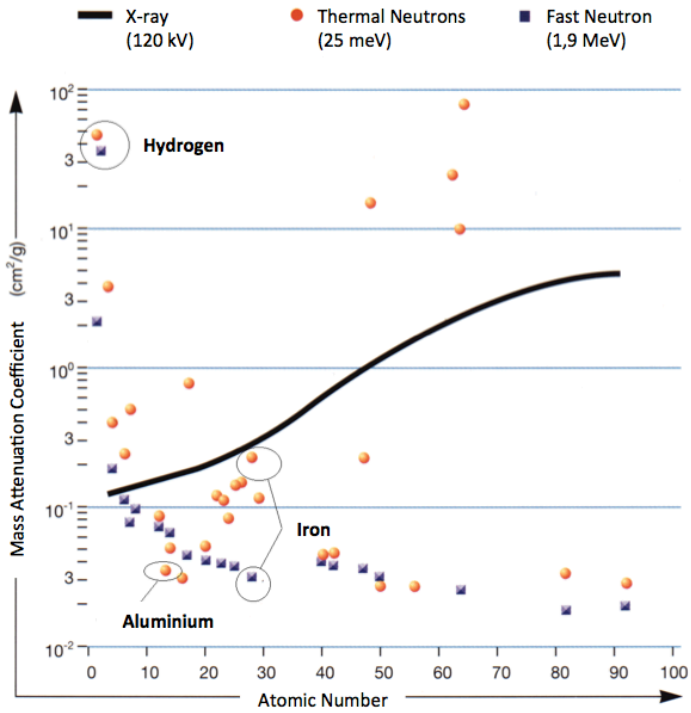

line.

Figure 1.7 *Attenuation coefficients for 120 keV X-rays (black line), thermal neutrons (red dot) and fast neutrons (blue dot). The diagram shows the relationship between the mass attenuation coefficient (attenuation at constant material thickness) and the atomic number (corresponding to the different elements) [Begovic 2007].*

The attenuation coefficient for thermal neutrons jumps up and down over the entire periodic table of elements. Fast neutrons (square symbols) exhibit a downward sloping curve. Some important metals (e.g. aluminum) attenuate neutrons less efficiently than X-rays. For iron, the attenuation strongly depends on the neutron energy (fast or thermal neutrons). Hydrogen produces virtually the largest level of attenuation.

Neutron has a magnetic moment and a magnetic scattering cross-section that is comparable to the nuclear cross-section for many atoms. Indeed, the neutron is electrically neutral but has a spin, or magnetic moment, so it is sensitive to magnetic sources in condensed matter and can be used to image magnetic structures.

1.2 Conventional Neutron Sources and Facilities

In the first section the principal features of neutrons have been briefly introduced. This short overview can give an idea why neutrons are potentially so interesting for research and applications. This second section is devoted to present existing neutron sources and facilities, before introducing in the third section the upcoming *Laser Driven Neutron Sources* and their potential.

Neutron source is a general term referring to a variety of devices that emit neutrons, irrespective of the mechanism used to produce the neutrons. Each neutron source can be characterized by:

- The energy of the neutrons emitted by the source.
- The rate of neutrons emitted by the source.
- The size of the source.
- The fabrication and maintenance cost of the source, and the governmental regulations related to the source.

Depending on its features, each of these sources finds use in several applications in areas of physics, material engineering, medicine, nuclear weapons, radiation hardness testing of materials for aerospace or for fusion/fission reactors, petroleum exploration, biology, chemistry, nuclear power and other industrial applications.

It is possible identify three principal categories of neutron source depending on the mechanism of neutron production:

1. Radioisotopes
2. Reactors
3. Accelerator Driven Neutron Sources (ADNS)

1.2.1 Radioisotopes

Using radioisotopes can be a way to generate small size neutron sources. Indeed, some isotopes undergo spontaneous fission with emission of neutrons. The radioactive isotope *californium*-252 is one of the most used spontaneous fission source. Usually, this radioactive isotope is produced by irradiating uranium or another trans-uranic element in a high-flux nuclear reactor. In this case, due to the absorption of neutrons, the initial material is transmuted into the spontaneous fission isotope.

Cf-252 neutron sources are typically of the dimension of a cylinder of 1 cm in diameter for few cm in length. Commercial new Cf-252 neutron sources emit

between 10^7 to 10^9 neutrons per second with a half-life of 2.6 years. The price of this kind of source is around 15,000 – 20,000 $.

Another common method to produce neutrons is to use a secondary process, exploiting the (α,n) nuclear reaction occurring when an alpha particle impinges on a low atomic weight isotope (like isotopes of *beryllium*, *carbon* and *oxygen*). Therefore, intermixing a radioisotope that emits alpha particles such as *radium* or *polonium* with a low atomic weight isotope, usually in the form of a mixture of powders of the two materials, it is possible to generate a neutron source. Typical emission rates for alpha reaction neutron sources is between 10^6 to 10^8 neutrons per second. A representative example is the *alpha-beryllium* neutron source that can be expected to produce approximately 30 neutrons every one million alpha particles. The lifetime of the source depends on the half-life of the radioisotope that emits the alpha particles. The size and cost of these neutron sources are also comparable to spontaneous fission sources. Usual combinations of materials are *plutonium-beryllium* (PuBe), *americium-beryllium* (AmBe), or *americium-lithium* (AmLi).

As described in the previous section, it has been exactly a source based on the (α,n) reaction that had pointed out to the first experimental evidence of neutrons. For example in the case of the ^{241}Am/Be source, the ^{241}Am undergoes α-decay, the α-particle can be absorbed by the light element *beryllium*, which then decays by neutron emission. This can be written as:

$$^{241}Am \longrightarrow {}^{237}Np + {}^{4}He\ (5.6\ MeV) \quad followed\ by$$
$$^{9}Be + {}^{4}He \longrightarrow {}^{12}C + n\ (few\ MeV)\,. \tag{1.5}$$

With a similar mechanism also gamma radiation with an energy exceeding the neutron binding energy of a nucleus can eject neutrons, it is the (γ,n) reaction. So it is possible to create a neutron source using for example radioisotopes, which decay with high-energy photons and coupled with *beryllium* or *deuterium*.

These radioactive sources have the advantage of being small and highly portable, but they have low intensity and are always "on". So they can be used for testing (e.g., of neutron detector), in medicine (e.g. activation analysis, cancer treatment with 252Cf needles), and for low-resolution/low-flux imaging. Conversely, the principal example of conventional neutron sources used for high-resolution/high-flux applications, are instead reactor sources and accelerator-based sources.

1.2.2 Reactors

Nuclear reactors use the fission process to produce neutrons. For uranium based reactors the main reaction is:

$$^{235}U + n \longrightarrow X + Y + Z\,n$$
$$(\sim 200\ MeV\ total\ energy\ release, \sim 2\ MeV\ per\ neutron). \tag{1.6}$$

Where X and Y are the fission fragments, and Z is a number between 0 and 8, with average value around 2.5.

The design of a fission reactor concerns principally the shape and size of the core, the arrangement and type of the fuel elements, control rods, coolant, moderator, reflectors and beam tubes. Depending on its particular design, a reactor can be optimized for different purposes. Basically we can distinguish between:

- Power reactors: optimized for heat extraction and efficient use of fuel.
- Research reactors facilities: optimized for high external thermal neutron flux.

A typical research reactor is designed in a way that 1 of the about 2.5 neutrons produced from the fission reaction is used to sustain the chain reaction, ~0.5 n is lost, and so one neutron is available for external use. The reactor power and source flux of various operating world-class research reactor sources, used for neutron scattering applications in particular, are shown in Table 1.2.

Country	United States	United States	Canada	France	France	Germany	Germany	Australia	Korea	Japan
Neutron source	HFIR	NBSR	NRU	HFR	ORPHEE	BENSC	FRM-II	OPAL	HANARO	JRR-3 M
Organization	Oak Ridge National Laboratory	National Institute of Standards and Technology	Atomic Energy of Canada Limited	Institut Laue-Langevin	Laboratoire Léon Brillouin	Helmholtz-Zentrum Berlin	Technische Universitat Munchen	Australian Nuclear Science and Technology Organization	Korea Atomic Energy Research Institute	Japan Atomic Energy Agency
Power (MW)	85	20	120	58	14	10	20	20	24 (present) 30 (designed)	20
Flux ($n \cdot cm^{-2} \cdot s^{-1}$)	1.5×10^{15}	3×10^{14}	3×10^{14}	1.5×10^{15}	3×10^{14}	2×10^{14}	8×10^{14}	3×10^{14}	2×10^{14}	3×10^{14}
Number of cold/hot sources	1/0	1/0	0/0	2/1	1/1	1/0	1/1	1/0	1(planned)/0	1/0
Number of instruments	9(present) + 6 (planned by 2012)	24	5	26	22	22	20 (present) + 10 (under construction)	6	6	24
Existing neutron imaging instrument		BT-2 [14]			[15]	CONRAD [16]	ANTARES [17]		NR-port [18]	TNRF [19] And TNRF-2 [20]
Facility operating since	1967	1970	1957	1972 (refurbished 1993)	1980	1973	2004	2006	1997	1990

HFIR: High-Flux Isotope Reactor [21]; NBSR: National Bureau of Standards Reactor [22]; NRU: National Research Universal Reactor, Chalk River, Canada [23]; HFR: High-Flux Reactor at ILL [1, 2]; ORPHEE: reactor at LLB [24]; BENSC: Berlin Neutron Scattering Centre [25]; FRM-II: Forschungsneutronenquelle Heinz Maier-Leibnitz [5]; OPAL: Open Pool Australian Light-water Reactor [6]; HANARO: High-flux Advanced Application Reactor [4]; JRR-3 M: Japan Research Reactor No. 3 Modified [3]. Consult the web sites for these facilities to obtain additional information and current details. A number of smaller research reactors, primarily at universities, are not listed here.

Table 1.2 *Existing medium-and high-flux reactor sources and their respective parameters [Arai and Crawford 2009].*

The world's most notable research reactor facility for neutron is the ILL I in Grenoble. This facility can emit a flux of $8\times10^{14} n\, cm^{-2}\, s^{-1}$ for a reactor power of $20\, MW$ or $1.5\times10^{15} n\, cm^{-2}\, s^{-1}$ for a reactor power of $58\, MW$. A comparable thermal neutron flux is also available at the FRM-II reactor in Munich. This reactor has been designed with a compact core with high enrichment capabilities and an optimized moderator arrangement, so it produces very high neutron fluxes outside the core for beam tube applications.

The possibility to design a reactor facility with higher flux requires higher power than at ILL and it is clearly a technical challenge that has a strong limitation with respect to the increasing safety regulation and the costly economical effort needed.

1.2.3 Accelerator Driven Neutron Sources

In the term accelerator driven neutron source (ADNS), it is possible to group the whole category of sources that are generated using an accelerator. Electrostatic tandem accelerators, cyclotrons and linear accelerators can accelerate protons or ions that can be used like projectiles thrown on a target, where neutrons are generated via a variety of nuclear reactions. Clearly the characteristics of the produced neutrons are determined by the characteristics of the accelerator used for producing the projectiles, together with the choice of the target and the type of reaction. An overview of the accelerators for neutron generation and its applications is presented in [Mank 2011].

Depending on the energy of the incident particle, the neutrons can be generated by:

- Induced nuclear reactions like (p,n), (d,n), (t,n) or (α, n) for low and medium energy particle accelerators.
- Nuclear spallation process for high-energy particle accelerators.

The induced nuclear reactions can produce quasi mono-energetic neutrons. For example, the electrostatic "sealed tube" system produces mono-energetic fast neutrons via the $D(d,n)^3He$ or the $T(d,n)^4He$ fusion reaction.

$$D + D \longrightarrow {}^3He + n\ (E_n = 2.5\ MeV)\,, \tag{1.7}$$

$$D + T \longrightarrow {}^4He + n\ (E_n = 14.1\ MeV). \tag{1.8}$$

A spallation source is a high-flux source in which protons or ions, accelerated to high energies, hit a target material, prompting the emission of neutrons. For example, a 1 GeV proton can produce approximately 25 neutrons from a lead target and only half of the proton beam power is dissipated through heat in the target, that means one order of magnitude less than in a fission

reaction producing the same time-averaged neutron flux.

Precisely, a spallation reaction is a process that occurs when a light projectile (proton, neutron or light ions) with a kinetic energy from several hundreds of MeV to several GeV interacts with a heavy nucleus (e.g. lead) and causes the emission of a large number of hadrons (mostly neutrons) or fragments.

In the spallation process, two stages can be identified: **intra-nuclear cascade** and **deexcitation**.

The intra-nuclear cascade is a fast direct stage (10^{-22} s) in which high-energy neutrons, pions, and spalled nuclei are emitted mainly in the direction of the incident projectile. During this stage, the projectile shares its kinetic energy with the target nucleons through elastic collisions, and a cascade of nucleon-nucleon collisions takes place. Some particles obtain high-enough energy to escape from the nucleus, while the rest of the energy is equally distributed among nucleons in the nucleus which is left in a highly excited state.

The following stage, deexcitation, takes place when the equilibrium is reached (10^{-16} s). During this stage the nucleus looses its energy by evaporation of lower energy neutrons or light charged fragments (e.g. d, t, α). In this case the particles are emitted isotropically. A competitive process to evaporation is fission, and the fission products also undergo evaporation. If the nucleus does not have enough energy to emit neutrons, it deexcites by γ-emission.

The scheme of Figure 1.8 illustrates these two stages in nuclear spallation by high-energy proton bombardment that usually occurs for proton energies above 100 MeV.

The energy of a small fraction of the neutrons produced in spallation processes can be as high as the incident proton energy (these neutrons require very thick shielding), but the spectrum reaches a maximum of around 2 MeV for the evaporating neutrons.

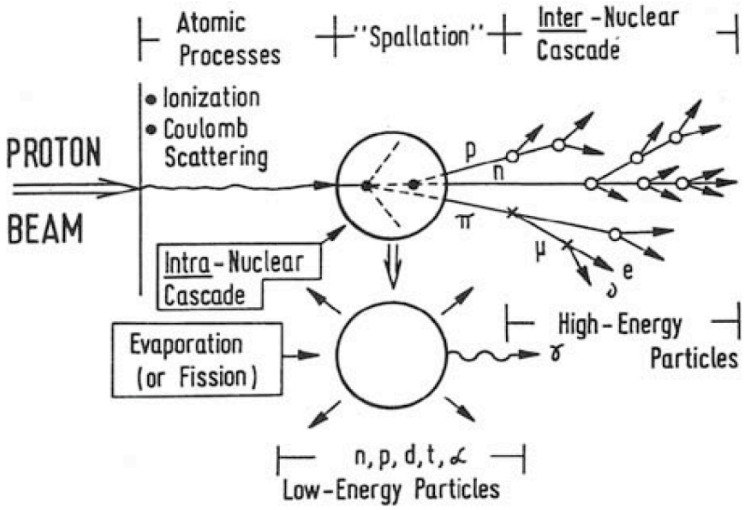

Figure 1.8 *Scheme of a spallation reaction taken from [Watanabe 2003].*

Clearly the characteristics of the produced neutrons are determined by the characteristics of the accelerator used for producing the high-energy projectiles together with the choice of the target for the spallation reaction.

Differently from the reactor sources that are continuous, for the accelerated-based sources, it is possible to obtain *short-pulse* or *long-pulse* neutron beams, depending on the pulse widths of the protons impinging on the spallation target. It is possible to obtain as well a continuous beam like in the case of the continuous cyclotron-based spallation sources (SINQ) at the *Paul Scherrer Institute* in Switzerland, that have performances similar to that of a medium-flux reactor. Short-pulse spallation neutron sources, typically delivering 1-μs proton pulse widths, require a ring structure (synchrotrons or accumulator/storage rings) in the accelerator system to provide high proton intensities in such short pulses.

Long-pulse sources typically have 1-ms proton pulse widths. No accumulator ring is required for such sources, so a very high intensity direct proton beam can be delivered from the linac to the neutron target.

Country	United States	United States	United States	U.K.	Switzerland	China	Europe	Japan	Japan
Neutron source	IPNS	LANSCE	SNS	ISIS	SINQ	CSNS	ESS	KENS	JSNS
Organization	Argonne National Laboratory	Los Alamos National Laboratory	Oak Ridge National Laboratory	Rutherford Appleton Laboratory	Paul Scherrer Institute	Institute of High Energy Physics	Undecided	High Energy Accelerator Research Organization	Japan Atomic Energy Agency
Proton energy (MeV)/ Current (μA)	450/15	800/70	1000/1400	800/200	590/1500	1600	1333/7500	500/9	3000/333
Proton beam power	7 kW	56 kW	1.4 MW	160 kW	1 MW	100 kW	5 MW	4.5 kW	1 MW
Repetition rate (Hz)	30	20	60	50/10 (2 targets)	Continuous	25	16 (long pulse)	20	25
Target material	Depleted Uranium	Tungsten	Mercury	Tantalum	Zircaloy	Tungsten	Mercury	Tungsten	Mercury
Moderator	S-CH_4/L-CH_4	L-H_2/H_2O	L-H_2/H_2O	L-H_2/L-CH_4/ H_2O	L-D_2/D_2O	H_2OL-CH_4L-H_2	L-H_2	S-CH_4/H_2O	L-H_2
Number of instruments	12	7	24 (beam ports)	22 (TS1) 7 (TS2)	15		20 (beam ports)	15	23 (beam ports)
Existing neutron imaging instrument					NEUTRA [30] and ICON [31]				
Facility operating since or planned to operate in	1981 (closed 2008)	1983	2006	1985 (TS1) 2008 (TS2)	1996	2014	Under planning	1980 (closed 2005)	2008

IPNS: Intense Pulsed Neutron Source [32]; LANSCE: Los Alamos Neutron Science Center [33]; SNS: Spallation Neutron Source [8, 9]; ISIS: [34, 35]; SINQ: Swiss Spallation Neutron Source [36, 37]; CSNS: Chinese Spallation Neutron Source [10, 11]; ESS: European Spallation Source [38, 39]; KENS: Koh-Energy-ken Neutron Source [40, 41]; JSNS: Japanese Spallation Neutron Source [8, 9]. Consult the websites for these facilities to obtain additional information and current details.

Table 1.3 *Past, existing, and future spallation source and their respective parameters [Arai and Crawford 2009].*

1.3 Laser Driven Neutron Source

The fission reactors and the spallation facilities presented in the previous section are nowadays the principal and most important sources for neutron research. Obviously building this kind of facilities is demanding with respect to the associated large dimension and high cost. In addition, the construction of new research reactors also induces political problems associated with safety.

Since the number of neutron applications is increasing, the possibility to have more affordable neutron sources will be very interesting for the research community. In [Hamm, 2008; Hamm 2010] the total number of neutron sources around the world in use today is estimated to be approximately a thousand, predicting an increase of 50 new units every year. In 2005 the International Atomic Energy Agency [IAEA 2005] has encouraged the construction and use of small and medium scale accelerators driven neutron sources ADNS. Indeed, these facilities are presented as an important alternative for the planned shutdown out of the small neutron producing research reactors. In the [IAEA 2005] technical report and in the more recent [Mank 2011] some of the reasons why the development of the neutron sources is important are illustrated with a long list of opportunities and potential applications for the neutron generation sector, for example as a test-bench for components and instrumentation designed for large neutron facilities, as "cheap" education and training tools or as home-lab sources for medium and small neutron flux applications. In this context the production of neutrons using ultra intense laser facilities can be a feasible alternative and can open new perspectives, as presented in [Alvarez 2012].

There are three main mechanisms that can be exploited for neutron production by laser:

1. **(ion,n):** light ions are accelerated from a solid target using an ultra intense laser. Neutrons can be produced either by a nuclear reaction inside the target where these ions are accelerated, or inside a secondary target irradiated by the ions.
2. **(gamma,n):** during the interaction between a solid target and an ultra intense laser, gamma rays are produced; they can excite the surrounding nuclei and produce neutrons.
3. **Implosion:** thermonuclear fusion, by the implosion of a micro capsule containing deuterium and tritium, can generate neutrons.

Depending on the type of laser used, it is possible to exploit one mechanism or another and obtain different characteristics of the source.

The laser system used can be distinguished basically in two categories:

- Very short pulse, duration in the range of tens of femtoseconds, with a few J of energy. It can be installed in a room and only costs a few million euros. It is the so-called table-top system.
- Large laser infrastructures which deliver hundreds of J per shot in a picosecond or nanosecond scale. They usually have tens of meters of amplification bays.

One of the differences between these two types of systems is that the laser repetition rate at a large facility is limited nowadays to a few shots per hour at best, whereas for small systems the shot rate is typically 1-10 Hz. However a significant increase of the repetition rate is expected for future higher energy laser facilities (e.g., Apollon or ELI at 1 shot/minute).

The features of each of the possible laser driven neutron sources will be discussed in the following paragraphs.

1.3.1 Neutron Production by Laser Produced Ion Beams

The (ion,n) reaction is surely the principal method used to produce a laser driven neutron source. The first step is the acceleration of a light ion species (proton in particular) using an ultra intense laser. Several laser driven processes can be used for this purpose and they will be discussed in detail in section 1.4.

The most common scheme used to produce neutrons via (ion,n) reaction consists in a primary target (the *pitcher*) that is irradiated by an ultra intense laser pulse wherein H or D ions are accelerated. The ion beam impinges on a secondary target (the *catcher*) where the neutrons are produced by a nuclear reaction. This scheme, also called ***dual target configuration*** or ***pitcher-cather set-up***, can be in some cases substituted by a single thicker target in which both the acceleration of ions and the nuclear reactions take place in the same material but at different depths (see Figure 1.9). In [Willingale 2011] a comparison between the two schemes is proposed in the case of the d(d,n)^{3}He reaction.

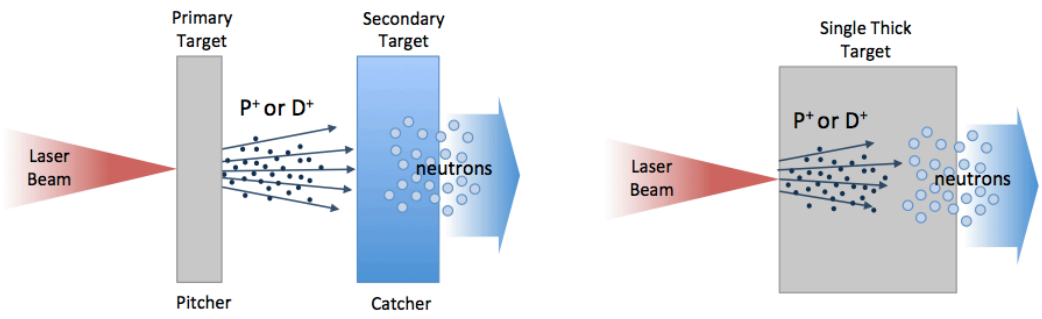

Figure 1.9 *Scheme used to produce laser driven neutrons via (ion,n) reaction.*

Neutrons can also be produced by using gaseous or cluster targets with D content. In this case Coulomb explosion plays a dominant role towards accelerating ions, which triggers the neutron generation by interaction with other D ions and neutral atoms from neighboring clusters [Ditmire 2000, Perks 2001, Madison 2003, Madison 2004]. However, the flux of these sources is very low as well as the total number of neutrons produced.

An ion-fission reaction or a spallation reaction with laser-accelerated ions can be an alternative way to produce neutrons [Mc Kenna *et al.*, 2005]. However, these two options are not very attractive. Indeed, the use of fissile element is very complex and involves a lot of safety precautions, while, as we saw in section 1.2.3, a spallation reaction requires a projectile energy above hundreds of MeV, which is far from the energies achieved nowadays by laser driven ions.

The total number of neutrons produced, in particular by laser-ion acceleration, globally follows a laser energy squared relationship [Ellison 2010], which implies that large systems typically produce three to four orders of magnitude more neutrons than table-top systems (10^9-10^{10} n/shot versus 10^6 n/shot).

1.3.2 Neutron Production by Gamma-N Processes

The interaction between an ultra-intense laser and a solid target entails the initial acceleration of electrons to relativistic speeds. These relativistic electrons are decelerated during their interaction with the bulk material and Bremsstrahlung radiation is emitted in the gamma ray range. The spectrum of photon energies produced through the Bremsstrahlung interaction is continuous. These photon energies range from zero up to a maximum value, which, for a monochromatic electron beam, is equal to the energy of the incident electron [Galy 2007]. Therefore (gamma, n) and (gamma, fission) reactions can take place in the surrounding nuclei and produce neutrons. This approach is far less effective compared to the ion drive one described previously. Indeed, the efficiency of laser light conversion to photons via electron/Bremsstrahlung is lower than one percent, while the efficiency of laser light to proton can reach up to 10%. In addition, cross-sections for (p,xn) reactions are higher than for (γ, f) or (γ, xn) reactions [Galy 2007, Galy 2009].

1.3.3 Neutron Generation by Laser Implosion

The third process that can be exploited to produce neutrons by intense laser pulses is thermonuclear fusion. Laser pulses can lead to the implosion of a microcapsule containing fusion fuel, like deuterium (D) and tritium (T), via **direct drive** or **indirect drive implosion** [Atzeni *et* Meyer-ter-Vehn 2004].

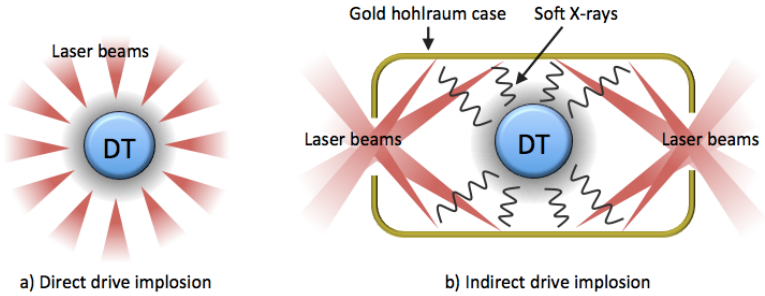

Figure 1.10 *Scheme of direct (a) and indirect (b) drive implosion.*

In Figure 1.10, a schematic representation of the two approaches is shown. Direct drive implosion means that the fuel pellet is directly irradiated by laser beams. In contrast with the indirect drive implosion where the laser beams irradiate a gold hohlraum cavity containing the fuel pellet. In this second case, the laser energy is converted into soft x-rays that are absorbed on the surface of the pellet and drive the implosion.

During the capsule implosion D(d,n)^{3}He or T(d,n)^{4}He (see section 1.2.3) fusion reactions can generate neutrons.

Due to the illumination configuration and the total laser energy required, high-flux neutron generation by implosion of fusible capsules can only be produced at large facilities with tens or hundreds of laser beams.

The neutron yield depends on the injected laser energy, and Figure 1.11 taken from [Alvarez 2012] shows some data points that are single shot results of neutron yield for different laser energies.

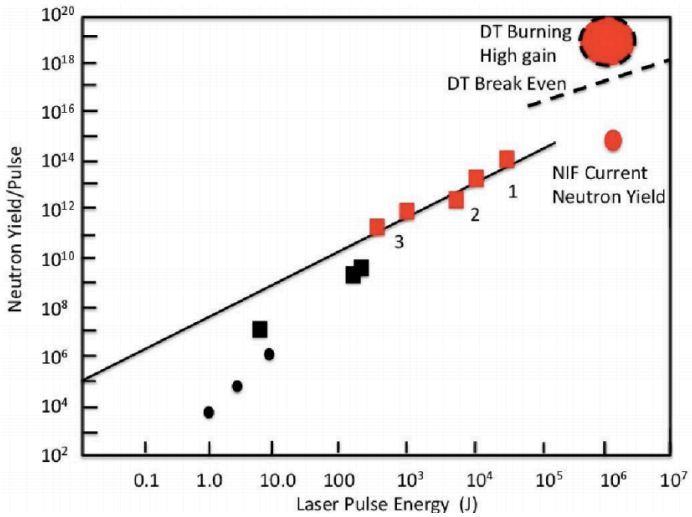

Figure 1.11 *Laser energy dependence of neutron yield. Red squares, black squares, and red circle correspond to implosion experimental neutron yields for LHART (Large High Aspect Ratio Target) [Yamanaka 1986], exploding pusher targets [Storm 1978], and NIF indirect drive [Lindl 1998], respectively. Small black circles are for the cluster fusion by using JanUSP [Madison 2003].*

1.4 Laser Accelerated Proton Beam

As anticipated in section 1.3.1, it is possible to accelerate ions using ultra intense laser pulses. In the last decade of the past century, several experiments [Clark *et al.*, 2000; Snavely *et al.*, 2000; Maksimchuck *et al.*, 2000] have reported evidence of ion acceleration from plasma produced by intense laser pulses. A wide scientific debate has been carried out during the past years to investigate the physics behind the different phenomena of acceleration. Nowadays, a general explanation is accepted by the laser plasma community, and several authors have presented overviews of the current scenario [Macchi *et al.*, 2013, d'Humières 2012, Daido *et al.*, 2012].

This section gives to the reader a summary of the principal acceleration mechanisms known up to now and the bibliography cited is a starting point for a more detailed study.

The ion acceleration process involves many complex physical phenomena: ionization, initial preplasma formation, coupling of the main laser pulse energy to electrons (absorption), plasma evolution driven by the laser and the collective plasma fields, hot electron transport in the plasma, and finally ion propagation during and after the acceleration process.

In all the experiments, an ultra intense laser pulse is focused on a target and an ion beam is accelerated depending on the characteristics of the pulse (energy, duration, intensity, presence or not of pre-pulse) and the type of target (solid foil, gas jet, cluster). The context of interest of this thesis is the interaction of short (< ps) laser pulses with solid foil targets.

The side where the laser beam irradiates the solid target is defined front surface, and the opposite side is defined rear surface. Three different types of ion beams can be identified:

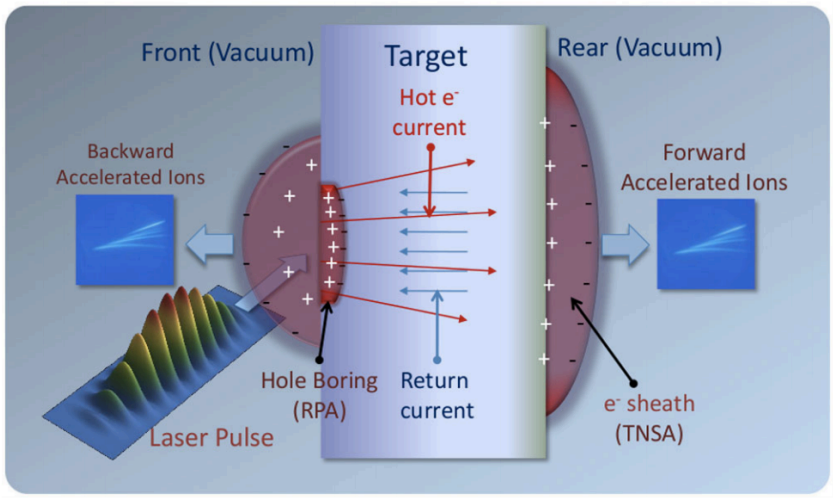

Figure 1.12 *Scheme of ion acceleration from solid target [Macchi* et al.*, 2013].*

- Forward beam generated on the rear surface.
- Forward beam generated on the front surface.
- Backward beam generated on the front surface.

The forward beams have been mostly studied and used during the experiment, since they present better characteristics (higher maximum energy, emittance, laminarity) for applications.

The type of laser pulse used in the interaction can discriminate how, in which region of the target and with which characteristics the ions are generated (see Figure 1.12). In particular, it is important to take into account the laser intensity I (W/cm^2), the wavelength λ, the polarization and the presence or not of the prepulse. Usually the main interaction laser pulse (with intensity >10^{18} W/cm^2) does not have an ideal Gaussian shape, but it can be preceded by a much longer pedestal and even by short small pulses, named pre-pulses. It is not always easy experimentally to control the presence and the shape of the pre-pulse, for this reason this is one of the major issues for the laser acceleration mechanisms.

The pre-pulse can be minimized with advanced cleaning pulse techniques (e.g. OPCPA [Kiriyama *et al.*, 2009], or plasma mirror [Doumy *et al.*, 2004]).

When a laser pulse with sufficiently high intensity (>10^{10}-10^{12} W/cm^2) interacts with a solid target, the matter is ionized and a plasma is generated. For a high-intensity laser pulse the preceding pedestal or the pre-pulse (that are usually in the range of ns or ps before) can have from 10^{-4} to 10^{-7} times the intensity of the main pulse, this means that they have sufficient intensity to form the plasma.

In a first approximate description, the laser propagates inside the plasma until the critical surface where the electron density n_e is about the critical density n_c, and the nonrelativistic critical density is given by:

$$n_c = \frac{m_e 4\pi^2}{\mu_0 e^2 \lambda^2}. \tag{1.9}$$

Where m_e is the mass of the electron, λ is the laser pulse wavelength, μ_0 is the permeability of free space and e is the electric charge of the electron.

The laser is reflected on the critical surface since the linear refractive index of the plasma is given by $\eta = \sqrt{1 - n_e/n_c}$. It possible to define an overdense region for $n_e > n_c$ where the linear refractive index η has imaginary value and the laser pulse cannot propagate. Therefore the laser plasma interaction occurs in the underdense region ($n_e < n_c$) or near the critical surface ($n_e \approx n_c$).

A population of energetic electrons[3] is generated around the critical density. These electrons are named *fast* or *hot electrons*. The generation of these hot electrons is due to different absorption mechanisms of the laser energy that are

[3] The laser accelerates first the particles with the largest charge-to-mass ratio, namely the electrons.

not being discussed in this thesis (acceleration by the ponderomotive force [Wilks 1992], resonant absorption [Estabrook 1978], the Brunel effect [Brunel 1987]).

In many cases, the energy of those hot electrons $k_B T_{e0}$ has been found to be adequately described by the Beg's experimental scaling [Beg *et al.*, 1997; Haines *et al., 2009*]:

$$k_B T_{e0} = 215 \left[\left(\frac{I_0}{10^{18}\, W cm^{-2}} \right) \left(\frac{\lambda}{\mu m} \right)^2 \right]^{1/3}. \qquad (1.10)$$

Where I_0 is the laser pulse intensity on the target in $10^{18}\, W cm^{-2}$ and λ the laser wavelength in μm. Alternative scaling have also been proposed.

The generation of the hot electrons population clearly depends on the laser and plasma parameters and differences have been observed depending on the experimental conditions. However, it is acceptable to assume the hot electron distribution to be Maxwellian with a temperature T_{e0}, which represents the average value of the electron energy, so T_{e0} is a function of the laser irradiance as $(I\lambda^2)^{1/3}$.

These hot electrons clearly move through the target, thus generating a large current j_h that must be locally neutralized by a return current j_r such that $j_h + j_r \approx 0$ [Bell *et al.*, 1997]. This return current is generated by the free, cold electrons, that can be both the conduction electrons for metals and the electrons produced by field and collisional ionization in insulators.

The hot electrons transport the absorbed energy in the overdense region (where the laser pulse cannot penetrate) and in the solid matter of the target.

From a theoretical point of view, four main regimes of acceleration have been suggested:

1. Target Normal Sheath Acceleration - TNSA
2. Radiation Pressure Acceleration - RPA
3. Collision-less Shock Acceleration - CSA
4. Transparency regime: Break-Out Afterburner - BOA

Since there are differences between theoretical and experimental conditions, it is not always easy to determine a dominant acceleration mechanism and it is important to underline that the mechanisms can be coupled.

Not only the characteristics of the laser pulse determine the acceleration regime, but clearly also the characteristics of the solid target (the material and the thickness).

An interesting representation of the zones where the different regimes can act is presented in [Daido *et al.*, 2012] (see Figure 1.13) together with examples of experimental data (see Table 1.4).

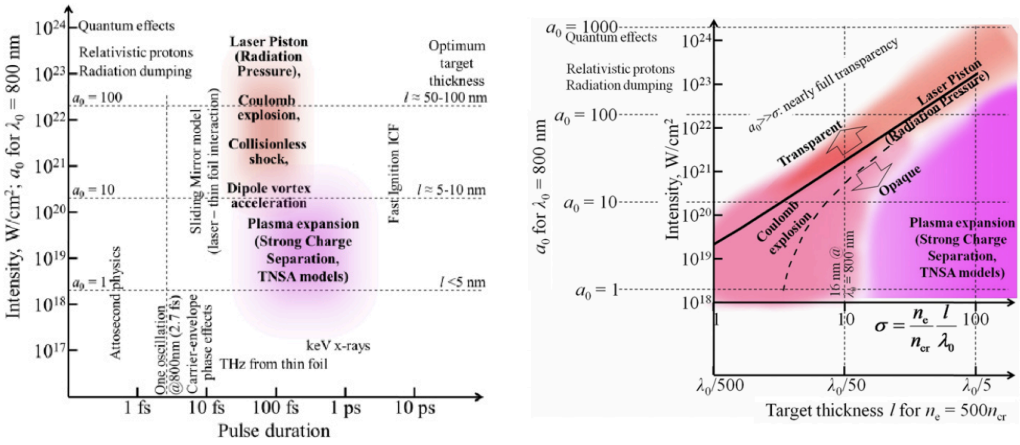

Figure 1.13 *Taken from [Daido et al., 2012]. (Left) Some of the possible regimes and applications of high-intensity short-pulse laser–plasma interaction. The regimes actually have no sharp borders, neither are they well separated; rather, they overlap with each other. (Right) Several regimes of laser-driven ion acceleration as function of target thickness and laser intensity. The borders of the regimes are not sharp; rather, there are gradual transitions between them. The solid line represents the condition of the relativistic transparency of a thin foil.*

No.	Reference	Pulse energy W_L (J)	Pulse duration τ (fs)	Irradiance I_0 (W cm^{-2})[a]	Contrast	Target and thickness (μm)	Incidence angle (°)	Proton/ion energy $\mathcal{E}_{p(i)}$, (MeV/nucleon)
1	Snavely *et al* (2000)	423	500	3×10^{20}	1×10^{4}	CH 100	0	58
2	Krushelnick *et al* (2000b)	50	1000	5×10^{19}		Al 125	45	30
3	Nemoto *et al* (2001)	4	400	6×10^{18}	5×10^{5}	Mylar 6	45	10
4	Mackinnon *et al* (2002)	10	100	1×10^{20}	1×10^{10}	Al 3	22	24
5	Patel *et al* (2003)	10	100	5×10^{18}		Al 20	0	12
6	Spencer *et al* (2003)	0.2	60	7×10^{18}	1×10^{6}	Mylar 23	0	1.5
7	Spencer *et al* (2003)	0.2	60	7×10^{18}	1×10^{6}	Al 12	0	0.9
8	McKenna *et al* (2004)	233	700	2×10^{20}	1×10^{7}	Fe 100	45	40
9	Kaluza *et al* (2004)	0.85	150	1.3×10^{19}	2×10^{7}	Al 20	30	4
10	Oishi *et al* (2005)	0.12	55	6×10^{18}	1×10^{5}	Cu 5	45	1.3
11	Fuchs *et al* (2006)	10	320	6×10^{19}	1×10^{7}	Al 20	0 and 40	20
12	Neely *et al* (2006)	0.3	33	1×10^{19}	1×10^{10}	Al 0.1	30	4
13	Willingale *et al* (2006)	340	1000	6×10^{20}	1×10^{5}	He jet 2000		10
14	Ceccotti *et al* (2007)	0.65	65	5×10^{18}	1×10^{10}	Mylar 0.1	45	5.25
15	Robson *et al* (2007)	310	1000	6×10^{20}	1×10^{7}	Al 10	45	55
16	Robson *et al* (2007)	160	1000	3.2×10^{20}	1×10^{7}	Al 10	45	38
17	Robson *et al* (2007)	30	1000	6×10^{19}	1×10^{7}	Al 10	45	16
18	Antici *et al* (2007)	1	320	1×10^{18}	1×10^{11}	Si_3N_4 0.03	0	7.3
19	Yogo *et al* (2007)	0.71	55	8×10^{18}	1×10^{6}	Cu 5	45	1.4
20	Yogo *et al* (2008)	0.8	45	1.5×10^{19}	2.5×10^{5}	Polyimide 7.5	45	3.8
21	Nishiuchi *et al* (2008)	1.7	34	3×10^{19}	2.5×10^{7}	Polyimide 7.5	45	4
22	Flippo *et al* (2008)	20	600	1.1×10^{19}	1×10^{6}	Flat-top cone Al 10	0	30
23	Safronov *et al* (2008)	6.5	900	1×10^{19}		Al 2	0	8
24	Henig *et al* (2009b)	0.7	45	5×10^{19}	1×10^{11}	DLC 0.0054	0	13
25	Fukuda *et al* (2009)	0.15	40	7×10^{17}	1×10^{6}	CO_2+He cluster jet 2000		10
26	Zeil *et al* (2010)	3	30	1×10^{21}	2×10^{8}	Ti 2 μm	45	17
27	Gaillard *et al* (2011)	82	670	1.5×10^{20}	1×10^{9}	Flat-top cone Cu 12.5	0	67.5

[a] Different authors do or do not include the incidence angle in the irradiance definition.

Table 1.4 *Experimental data of laser-driven ion acceleration [Daido et al., 2012].*

1.4.1 Target Normal Sheath Acceleration (TNSA)

Known with the acronym TNSA, *Target Normal Sheath Acceleration* has been proposed for the first time in [Wilks *et al.*, 2001] as an explanation for the energetic protons observed on the backside of a solid thick target irradiated by the Nova PW laser [Snavely *et al.*, 2000]. In [Wilks *et al.*, 2001], for the first time, the authors hypothesized the model that has been afterwards generally accepted and it is described in detail in [Mora 2003; Mora 2009].

In this model the hot electrons generated on the front surface of the target cross the target bulk and reach the rear surface where a cloud of relativistic electrons is formed: the ***sheath***. The hot electrons attempt to escape in vacuum from the rear surface [Link *et al.*, 2011] and lead to a plasma expansion over several Debye lengths. A charge unbalance is created and consequently an intense (TV/m) E field is generated, mostly directed along the target normal surface. This field is able to accelerate protons and ions mostly coming from a thin layer of impurities on the rear surface (contaminated with water or hydrocarbons [Allen *et al.*, 2004]).

The presence of hot electrons also on the front surface leads to a similar behavior also on this side: the creation of a charge unbalance and an electric accelerating field and, as a consequence, a plasma expansion induced by the hot electron sheath. Therefore, protons and ions are accelerated also backward from the contaminated layer on the front surface. The more remarkable difference in this case is that when the main pulse arrives on the front surface it finds an already pre-formed plasma due to the laser pre-pulse[4]. So in this case the plasma gradient density is not sharp like in the backside surface. This affects the quality and the characteristics of the beam produced [McKenna *et al.*, 2004; Fuchs *et al.*, 2007].

Therefore the TNSA is the acceleration model that describes the production of the forward beam generated on the rear surface and a backward beam generated on the front surface, but in this thesis we are interested to investigate just the characteristics of the first beam for which the TNSA is more efficient [McKenna *et al.*, 2004; Fuchs *et al.*, 2007].

The sheath electric field E_s can be related to the hot electrons temperature T_h and the typical spatial extension of the sheath L_s by [Mora 2003]:

$$eE_s \sim k_B T_h / L_s \,. \tag{1.11}$$

The plasma expansion in vacuum can be divided in two phases:

1. A first phase with duration of the order of the laser pulse duration where the laser transfers its energy to the electrons that feed the

[4] Note that for strong laser pre-pulse and very thin target also the rear surface can be affected and all the acceleration mechanism is compromised [Kaluza *et al.*, 2004; Fuchs *et al.*, 2006].

sheath on the rear surface. For short pulse duration the ions can be considered fixed and the ***expansion isothermal***.

2. A second phase where the expansion of the plasma in vacuum passes from an isothermal regime to an ***adiabatic regime***. The electrons transfer progressively their energy to ions or protons, and during this phase the electrostatic accelerating decreases progressively until the velocity of protons and electrons become equal and the acceleration process ends.

The result of TNSA is a bunch of accelerated electrons that co-moves with a bunch of accelerated protons and ion species, the charges being neutralized.

For most of the possible applications of TNSA ion beams, it is important to know the maximum energy achievable at a given laser intensity. Using a model that incorporates theoretical results of the isothermal expansion[5] of a hot plasma [Mora 2003] coupled with a model of the characteristic ion acceleration time, it is possible predict the maximum ion energy:

$$E_{max} = 2ZT_h \left(ln \left(t + \sqrt{t^2 + 1} \right) \right)^2 . \qquad (1.12)$$

Where $t = \omega_{pi} t_{acc} / \sqrt{2\exp(1)}$ with t_{acc} the acceleration time and $\omega_{pi} = (n_{e0} Ze^2 / M_i \varepsilon_0)^{1/2}$ the ion plasma frequency (n_{e0} is the initial electron sheath density and M_i the ion mass).

The initial electron density n_{e0} can be determined by the evaluation of the quantity of hot electrons accelerated inside the target by the laser $N_e = fE/T_h$, where f is the laser energy fraction absorbed in the plasma and converted in hot electrons[6]. The electrons are distributed inside the thickness d of the target and a part of them is spread on the electron sheath area A_{sheat} at the back of the target [Antici *et al.*, 2008]. This would give $n_{e0} = N_e / (d \times A_{sheat})$ where $A_{sheat} = \pi(r_0 + d \times tan\theta)$, r_0 is the radius of the zone from which the electrons are accelerated at the critical interface, that can be assumed equal to the focal spot radius ($r_0 = FWHM$), and θ is the hot electron divergence half-angle[7].

[5] An isothermal model can be used analytically contrary to an adiabatic one that can be solved only numerically [Mora 2005].
[6] A typical value of f is 10-15% [Ping *et al.*, 2008].
[7] Several experimental and theoretical studies show that θ is between 15° and 40° [Fuchs et al., 2003; Stephens et al., 2004; Adam et al., 2006], increasing with laser energy.

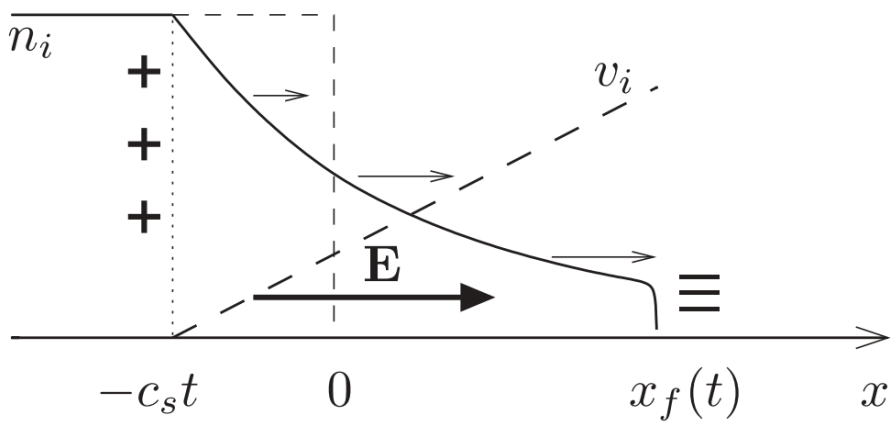

Figure 1.14 *Taken from [Gauthier thesis 2013]. Density and velocity profiles from the self-similar solution for the isothermal expansion [Mora 2003].*

The acceleration time t_{acc} represents the time during which the electron temperature T_h is considered constant in the model, therefore it must be of the order of the pulse duration [Fuchs *et al.*, 2006] except for very short pulses. Indeed, if we consider pulses of very short duration, a minimum time t_{min} to transfer the energy from the electrons to the ions will be needed. The laser intensity will also affect the acceleration time, since low intensities induce lower plasma expansion and therefore an increase of the time duration over which acceleration occurs. A function that defines the value of the acceleration time can be defined like: $t_{acc} = \alpha(\tau_{Laser} + t_{min})$ where τ_{Laser} is the laser pulse duration, $t_{min} = 60\ fs$ and α is a parameter that varies linearity from 3 (for a laser intensity $I = 2{\times}10^{18}\ W/cm^2$) to 1.3 (for $I = 10^{19}\ W/cm^2$) and remains constant at this value for higher intensities [Fuchs *et al.*, 2007].

Observing Figure 1.14, that represents the sketch of the density and velocity profiles from the self-similar solution in the case of isothermal plasma expansion, it is possible to identify the front of the charge separation at $x = x_f(t)$ and the rarefaction front at $x = -c_s t$. The electric field is uniform in the $-c_s t < x < x_f(t)$ region.

1.4.2 Radiation Pressure Acceleration (RPA)

In the *radiation pressure acceleration* (RPA) regime, the ions are accelerated from the front surface by the radiation pressure of the irradiating light. Electrons are pushed by the laser ponderomotive force at the front of the target and lead to a strong charge separation setting up a high amplitude electrostatic field. This field will accelerate **front surface ions** to high energies during the duration of the laser pulse. Laser ion acceleration through the laser radiation pressure has first been studied theoretically and using Particle-In-Cell simulations by [Wilks et al. 1992] and [Denavit et al. 1992]. It was first referred as the *hole*

boring regime and can lead to the development of strong electrostatic shocks inside the target [Silva et al., 2004].

Electromagnetic (EM) waves carry momentum, which may be delivered to a nontransparent (either absorbing or reflecting) medium. The radiation pressure, for a monochromatic EM wave of intensity I and frequency ω normally incident on the plane surface of a medium, is given by:

$$P_{rad} = (1 + R - T)\, I/c \; = (2R + A)\, I/c \,. \tag{1.13}$$

Where R, T and A are the *reflection*, t*ransmission* and *absorption coefficients* (with $R + T + A = 1$).

The ponderomotive force is proportional to the inverse of the particle mass, therefore it acts effectively on the electrons that are pushed inward at the critical surface of the overdense plasma region.

This regime starts to show its effects in the proton acceleration process for laser intensity higher than 10^{20} W/cm² [Kar *et al.*, 2012] and, depending on the target thickness, it is possible to observe some differences, which are detailed in the following.

Thick target – Hole boring

The intense radiation pressure of the laser pulse pushes the surface of an overdense plasma inward and steepens the density profile (parabolic deformation of the plasma surface). This process usually named **hole boring** allows the laser to penetrate deeply into the target. In the literature the authors sometimes refer to this same process using also the name *sweeping acceleration* [Sentoku et al., 2003] or *laser piston* [Schlegel et al., 2009].

It is possible to estimate the recession velocity of the plasma surface v_{HB} by balancing the EM and the mass momentum flows in a planar geometry.

$$\frac{v_{HB}}{c} = \sqrt{\frac{1}{2}\frac{n_c}{n_e}\frac{Zm_e}{M_i}a_0^2}\,. \tag{1.14}$$

Using the preceding plasma surface velocity it is possible to estimate analytically the maximum proton energy of forward accelerated protons from the front surface.

$$E_{max} = 2M_i v_{HB}^2\,. \tag{1.15}$$

Thin target – Light sail regime

The hole boring RPA is the description of the radiation pressure for thick[8] target, but when the target is thin enough and with a low mass so that all the ions are accelerated before the end of the laser pulse, the RPA regime is named *light sail*. In this case the laser pulse is able to accelerate ions to higher energies since the ions are not screened by a background plasma [Macchi *et al.*, 2012].

1.4.3 Collision-less Shock Acceleration (CSA)

Collision-less shock acceleration (CSA) mechanism has been proposed as an ion acceleration mechanism in superintense laser interaction with an overdense plasma on the basis of PIC simulations by [Denavit 1992] and [Silva et al. 2004].

More recently, it has been also highlighted in simulations by [d'Humières *et al.*, 2010; d'Humières *et al.*, 2013]. In this acceleration scheme, protons are accelerated inside the target by collision with the electrostatic potential barrier at a discontinuity surface named ***shock front***. Therefore, it combines shock front acceleration with the volumetric inductive acceleration variant of TNSA.

In CSA, the ions are first accelerated in the same manner by the inductive electric field. Due to the smooth density gradient at the rear side, the inductive electric field monotonously decreases with the distance from the high-density zone. Ions in the low-density region therefore experience an electric field lower than ions from the higher density region. As a result, ions from the low-density region can be caught by the ions coming from the higher density region, leading to the formation of an electrostatic shock front, a peak of ion density propagating inside the decreasing (low) density ramp.

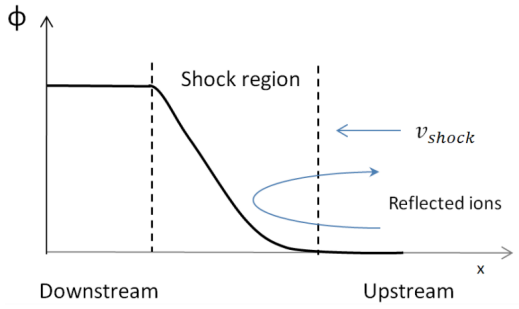

Figure 1.15 *Scheme of the CSA regime.*

[8] Much thicker than the skin layer in which ion acceleration by space-charge field occurs.

The ions located upstream are then reflected by the shock structure and accelerated at velocities up to twice the shock velocity. This however requires an adequately tuned rear-density gradient, in the range of tens of μm up to few hundreds of μm, depending on the laser intensity, so that these events can take place favorably. This mechanism has never been demonstrated experimentally.

1.4.4 Transparency Regime: Break-Out Afterburner

The transparency regime is achievable when ultrathin foils are used as targets and the high-intensity laser pulse presents an ultrahigh-contrast (prepulse-free conditions) in order to avoid the early destruction of this ultrathin target (same as in RPA). Under these conditions, it is possible to induce a relativistic transparency of the target so that the laser can propagate above the critical density n_c into the target [Fuchs *et al.*, 1998]. While this effect limits the energy attainable via RPA, it can lead to enhanced ion acceleration via different mechanisms.

Simulation studies of this regime show that the increase of the cutoff energy is related to enhanced and volumetric heating of electrons as the target becomes transparent, leading to a stronger accelerating field for ions. Contrary to TNSA, where only a small fraction of the available electrons became "hot", in this regime all the bulk of the electron volume is heated, and the acceleration process of the ions take place inside the target and not on the surface.

The name *break-out afterburner* BOA was proposed for such regime by the Los Alamos group [Yin et al., 2007]. The modeling of this process is very complex since it involves different stages.

A scaling of the maximum ion energy has been proposed as:

$$E_{max} \simeq (1 + 2\alpha) Z T_e \,. \tag{1.16}$$

Where T_e is the electron temperature and α a phenomenological parameter (estimated to be ~3 from simulations) [Macchi *et al.*, 2013].

Chapter 2

Experimental Design and Diagnostics Description

Abstract The second chapter of this thesis is devoted to present to the reader the concept that has motivated us to perform the two experimental campaigns presented in the next chapter (ELFIE and TITAN). That is the possibility to exploit new experimental schemes to shorten the duration and to select in energy a laser driven neutron source. In the first section I present the roadmap we have set to follow and all the preliminary considerations we have made, while in the second section there is a short description of all the diagnostics used during the experiments. The reader will so be able to easily interpret the two experimental campaigns and their results that are presented in the third chapter.

2.1 Concept: Improving a Laser Driven Neutron Source

In the previous chapter, I introduced all the principal and most interesting characteristics of the existing neutron sources. I highlighted that to make available for the future more affordable neutron sources is a challenging objective, especially when desiring to match the demand for new sources to respond to the increasing number of neutron applications. The laser driven neutron sources presented in § 1.3 are not only a good alternative to the existing traditional neutron sources, but they also exhibit interesting and new characteristics as a very short pulse duration. Indeed, in theory a laser driven neutron source could be of about the laser pulse duration. However, we have to consider that, over a long distance, the short duration of a beam of moving particles is preserved only if the range of particle energies (and therefore the range of their velocities) is narrow. We established the

objective to experimentally study the possibility of narrowing the energy spectrum of a laser driven neutron source. Achieving this result would be a good starting point for future applications of this kind of neutron sources in fast neutron radiography.

We decided to generate neutrons using the dual target configuration, the so-called pitcher-catcher set-up, described in the § 1.3. In this scheme, the energy spectrum of the produced neutrons depends on:

- The characteristics of the ion beam accelerated from the primary target.
- The catcher material and so the nuclear reaction that will generate the neutrons.
- The thickness of the catcher.

Once the characteristics of the catcher are fixed, the neutron generation process is driven by the laser-accelerated ions. Therefore, acting on the characteristics of the ion beam, it is possible to modify the energy spectrum of the neutrons. We decided to achieve the collimation of the ion beam and a narrowing of its energy spectrum using a ***laser-triggered micro-lens*** (see § 2.1.2). The idea was to take advantage of these new characteristics of the ion beam to perform a narrowing of the neutron spectrum.

In our experiments we expected to accelerate protons via the TNSA mechanism and then to generate neutron with a (p,n) reaction inside the catcher. The full neutron spectrum achieved in that way should be compared with the neutrons produced using a modified proton spectrum. Three steps are needed, as schematized in Figure 2.1:

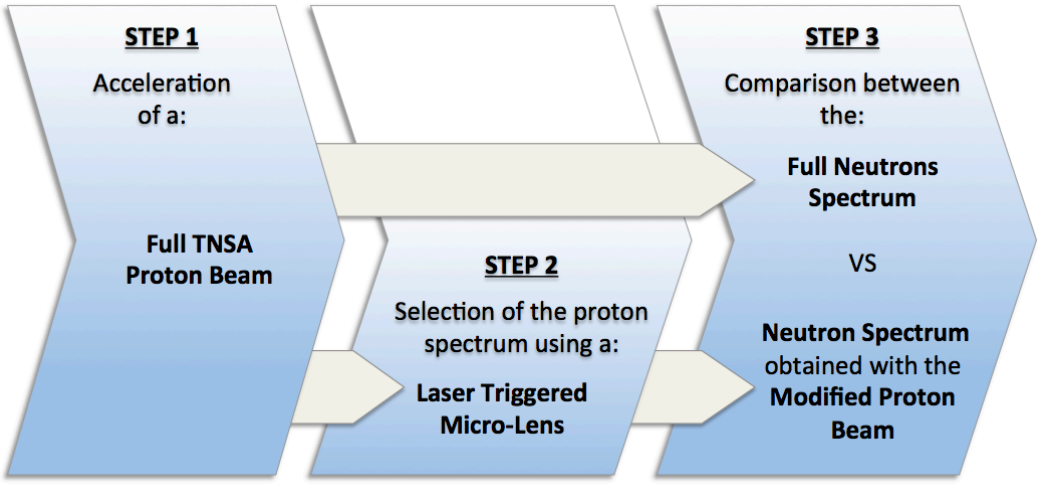

Figure 2.1 *Scheme of the experimental concept to study the spectrum modification of a laser driven neutron source that is possible to obtain with a laser triggered micro lens set-up.*

1. Step 1: Acceleration of a TNSA proton beam (with a full energy spectrum).
2. Step 2: Modification of the TNSA proton beam accelerated in the step 1 using a laser-triggered micro lens device.
3. Step 3: Comparison between the full neutron spectrum obtained using the full proton spectrum from step 1 and the modified neutron spectrum obtained by the modified proton spectrum from step 2.

Each of these steps is discussed in the next sections together with preliminarily considerations.

2.1.1 Step 1: Acceleration of Protons via the TNSA Mechanism

As will be presented in the next chapter, we carried out two experiments at two different laser facilities: the ELFIE laser system (LULI) and the TITAN platform at the Jupiter Laser Facility (LLNL). The laser pulse intensity was $\sim 10^{19}\ W/cm^2$ at ELFIE and $\sim 10^{20}\ W/cm^2$ at TITAN (see chapter 3 for more detailed information about the facilities). Therefore, as discussed in § 1.4.1, the proton beam we could produce during our experiments was a TNSA proton beam.

In section 1.4.1 the theoretical frame of the TNSA mechanism has been introduced. In this section I would like to detail the ion beam characteristics it is possible to obtain using this mechanism.

As discussed in the previous chapter, thanks to target normal sheath acceleration, two proton beams can be produced, a *forward*-directed beam (mostly from the rear surface of the target) and a *backward*-directed beam (from the front surface of the target).

During our experimental campaigns, we were interested to exploit the forward proton beam because, as already said, it is the one that presents the best characteristics (higher maximum energy, emittance, laminarity). Anyway, it is important as well to take into account the fact that the backward proton beam impinging on material inside the chamber can produce background neutrons or gamma signal.

Since the TNSA is one of the regimes that has been most intensively studied for the acceleration of protons in ultra-intense laser plasma physics, it is also one of the better known. So the characteristics of a TNSA proton beam can be easily predicted, as I detail below.

Proton Energy Spectrum

The energy spectrum represents the number of particles accelerated at certain energy, and it is one of the most important characteristics for applications in general, and for our study in particular.

Depending of the intensity of the laser pulse and the material of the target, it is possible to characterize the spectrum of the protons produced. The energy spectrum of the beam is typically broadband with a quasi-exponential decay up to a cut-off E_{max} maximum energy. It is possible to approximate the proton number per MeV with a quasi-thermal Boltzmann distribution:

$$\begin{aligned} &for\ E < E_{max} && \frac{dN}{dE}(E) = \frac{N_0}{T}\exp\left(-\frac{E}{T}\right), \\ &for\ E > E_{max} && \frac{dN}{dE}(E) = 0\,. \end{aligned} \tag{2.1}$$

The maximum energy scales with the laser parameters as seen in section 1.4.1. In Figure 2.2 some typical spectra of a TNSA proton beam are shown, for four different laser facilities (taken from [Schollmeier thesis 2008]).

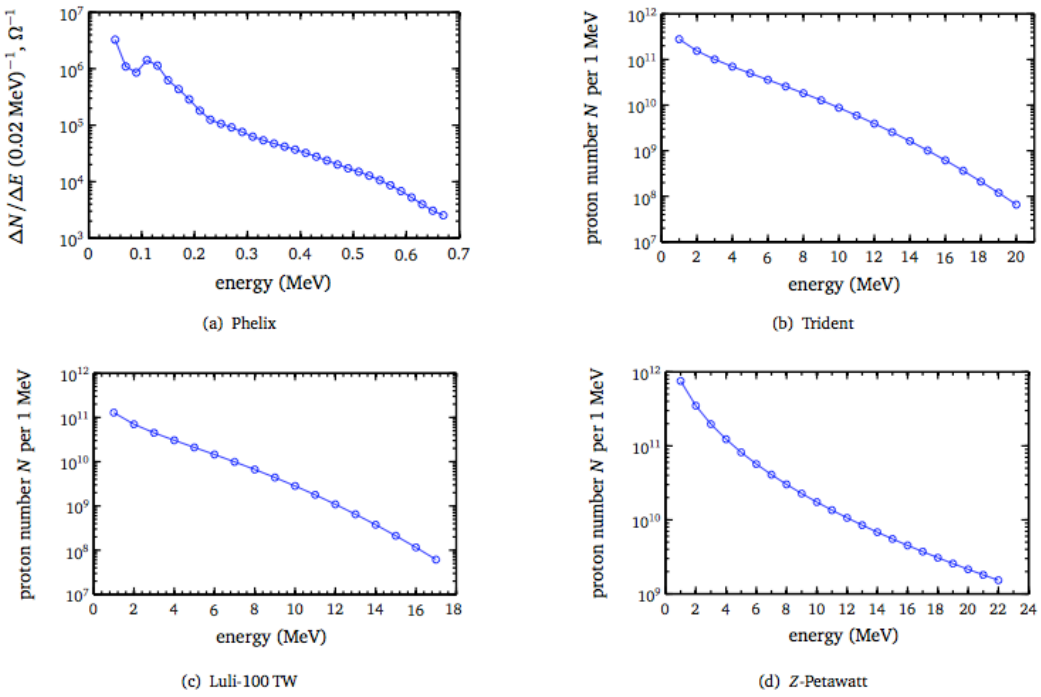

Figure 2.2 *Energy spectra obtained at a) PHELIX (Darmstadt), b) TRIDENT (Los Alamos, NM, USA) c) LULI- 100TW (Palaiseau, France) and Z-Petawatt (Albuquerque, NM, USA) [Schollmeier PhD thesis 2008].*

Source Size

Past studies have investigated the size of the proton source on the rear side of the target, where the forward TNSA protons are accelerated. An energy dependence of the source size has been observed. Indeed, the size decreases with increasing the proton energy, as shown in Figure 2.3.

In [Schollmeier thesis 2008], the energy-resolved source sizes for different laser facilities are presented, as shown in Figure 2.4.

The energy-dependence of the source size is directly related to the electric field strength distribution of the accelerating hot electron sheath at the source. In [Cowan *et al.*, 2004] the decrease of the emission zone is explained as a consequence of the transversally bell-shaped electron density distribution. In the central zone of the sheath there is the high-density portion of this distribution. This is where the highest energy protons are accelerated, whereas lower energies protons come from the wings of the sheath distribution.

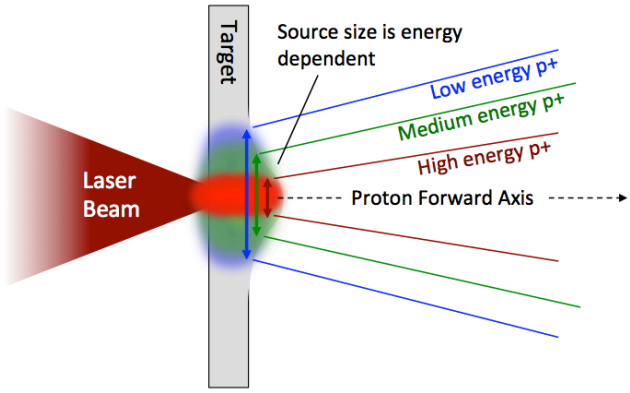

Figure 2.3 *Scheme of the source size energy dependence.*

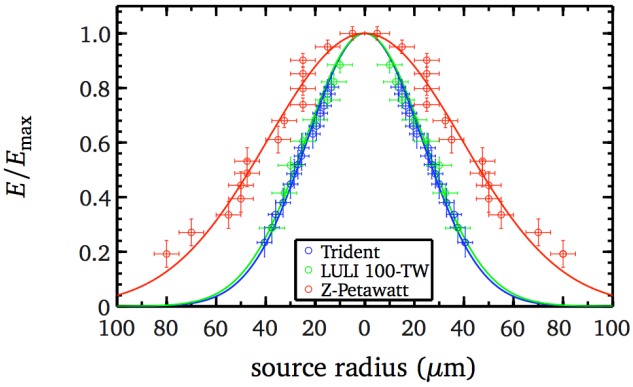

Figure 2.4 *Energy-resolved source sizes for data from TRIDENT (blue), LULI-100TW (green) and Z-Petawatt (red), respectively [Schollmeier thesis 2008].*

Beam Emittance

The beam emittance is a very important parameter in the physics of particle acceleration since it provides a description of the quality of the beam. The value of the emittance is a measure of the average spread of particle coordinates in the position-and-momentum phase space. It can be measured in all three spatial dimensions. It is called ***longitudinal emittance*** for the dimension parallel to the motion of the particle and ***transverse emittance*** for the other two dimensions.

Assuming that the beam propagates along the z axis, it is possible to define the transverse emittance for x and y direction. The trajectories of the particles of the beam are confined inside small, near-axis regions, and the transverse momentums are much smaller than the longitudinal momentum ($p_{x,y} \ll p_z \approx p$), which allows us to consider the angle x' , y' instead than the transverse momentum with the following approximation:

$$x' = \frac{p_x}{p_z} \approx \frac{p_x}{p}, \qquad y' = \frac{p_y}{p_z} \approx \frac{p_y}{p}. \tag{2.2}$$

If in the phase space (x, x') the whole particle distribution can be contained inside an ellipse of surface A, the transverse emittance ε_x can then be defined as:

$$\varepsilon_x = A/\pi \qquad [mm\ mrad]\ . \tag{2.3}$$

And the ellipse equation can be written as:

$$\gamma_x x^2 + 2\alpha_x x x' + \beta_x x'^2 = \varepsilon_x\ . \tag{2.4}$$

Where (x, x') are the particle coordinates in the phase space and the coefficients $\gamma_x(z)$, $\alpha_x(z)$, $\beta_x(z)$ are the Twiss parameters.

As shown in Figure 2.5, it is possible to use the Twiss parameters to define the maximum value of x (boundary of the beam envelope) $x_{max} = \sqrt{\beta_x \varepsilon_x}$ and the maximum beam divergence $x'_{max} = \sqrt{\gamma_x \varepsilon_x}$.

An important property of the beam is obtained according to the *Liouville theorem*: the volume occupied by the beam in the 6D (x, p_x, y, p_y, z, p_z) phase space is constant, provided that there are no dissipative forces acting on the beam, no particles lost or created and no binary Coulomb collisions between particles.

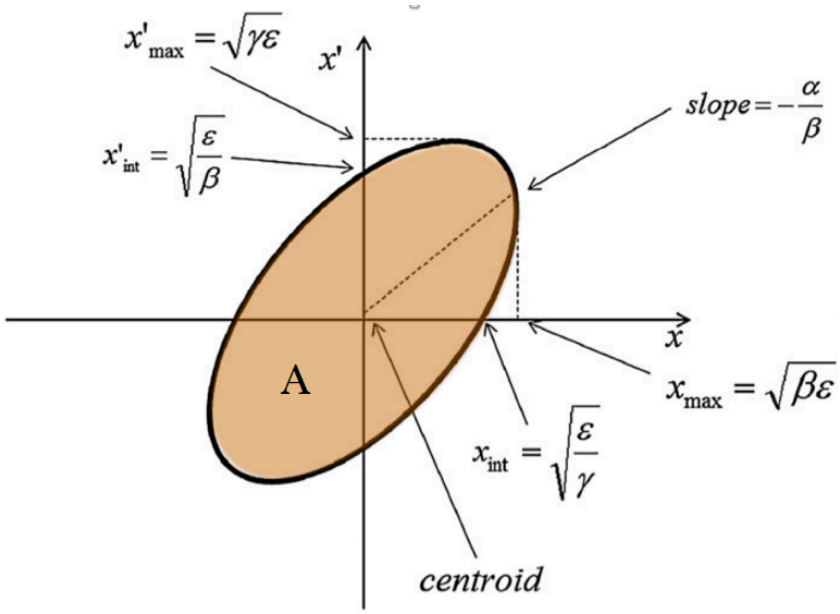

Figure 2.5 *Phase space distribution in a skewed elliptical boundary showing the relationship between the Twiss parameters and the ellipse geometry.*

Moreover, if the forces in the three orthogonal directions are uncoupled, the Liouville theorem holds also for the surfaces of each reduced phase space $(x, p_x), (y, p_y), (z, p_z)$ and hence also the emittance remains constant in each plane [Reiser 1994].

The transverse emittance gives information about the *laminarity* of the beam. It is a very important parameter also for our experimental study. An ideal highly charged particle beam has orbits that flow in layers that never intersect, as occurs in a laminar fluid. Such a beam is often called a laminar beam. More precisely a laminar beam satisfies the following two conditions:

- # 1: All particles at a given position have identical transverse velocities.
- # 2: The angle x' has a linear dependence to the displacement x from the axis z of beam propagation.

The particle distribution of an ideal laminar beam in the transverse phase space is a straight line, as shown in Figure 2.6 (a), and therefore the emittance is zero. In this case, it is always possible to identify a unique Virtual Source Point (VSP) for the beam.

On the contrary, if the beam does not satisfy the first condition, as in the case shown in Figure 2.6 (b), for each position x a different VSP is defined. In this case, the representation of the particle distribution on the phase space deviates from a straight line showing that the beam is not perfectly laminar. The relation between each position x and the angle x' is still biunique and the particle distribution does not occupy an area on the phase space, therefore also in this case the emittance (like previously) defined is still zero.

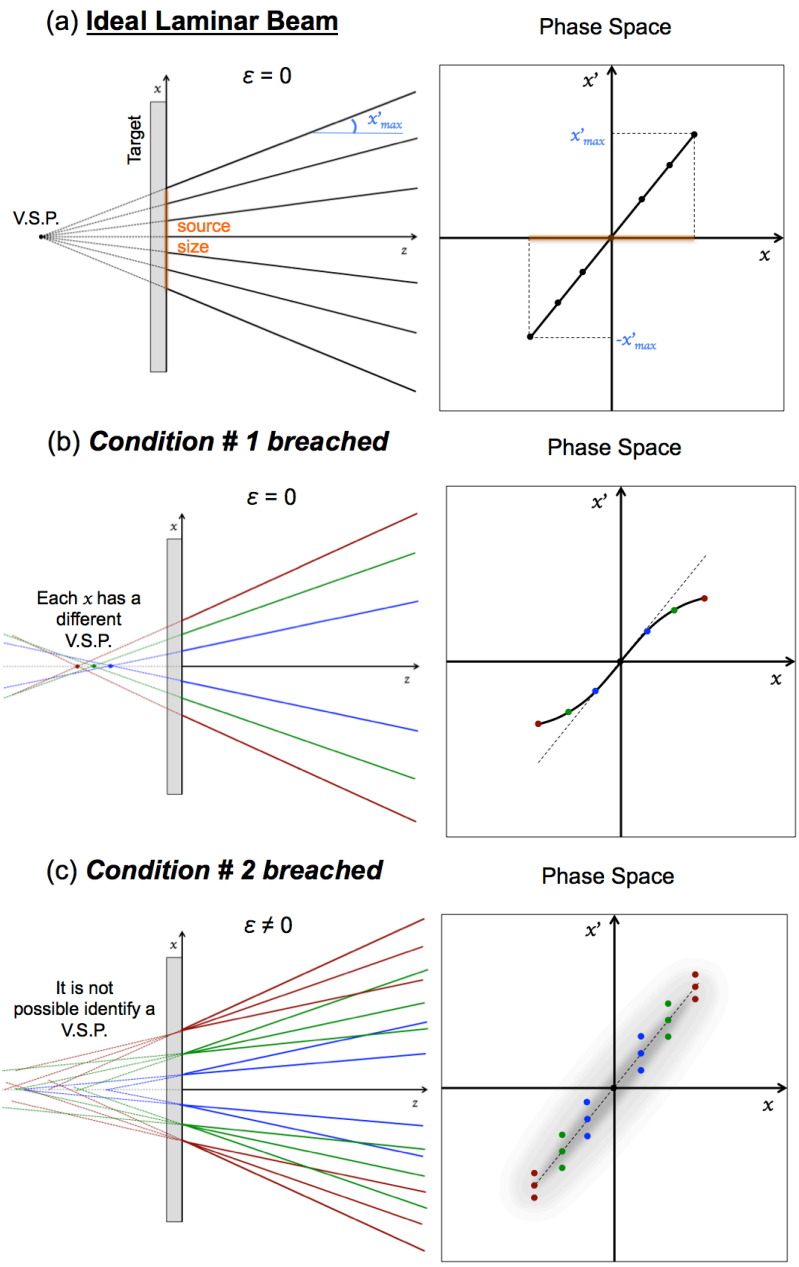

Figure 2.6 *Graphic representation of a particle beam and its phase space. (a) Represents the case of an ideal laminar beam. (b) represents the case of a beam that breaches the condition #1 although it respects the condition # 2. (c) Represents the case of a beam that respects condition #1 and breaches condition #2.*

When the beam does not respect the second condition its representation in the transverse phase space occupies a surface contained in the previously defined ellipse (see Figure 2.6 (c)). In this case the transverse emittance is different from zero, and no VSPs can be identified but a minimum envelope of the beam waist can be defined.

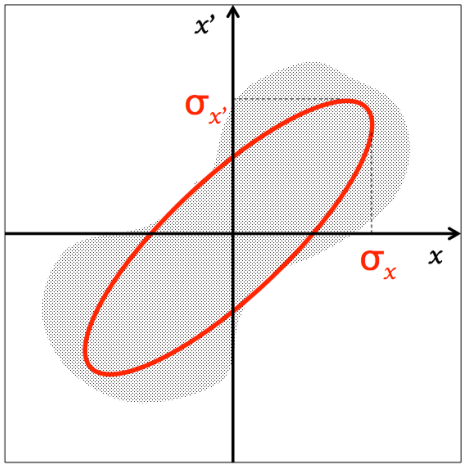

Figure 2.7 *Phase space distribution of a real beam (black dots) with superimposed the equivalent ellipse (red line).*

Considering that a realistic phase space distribution can be quite different from a regular ellipse it is often useful to consider a statistical definition of the emittance. In this case, one can define a so-called *rms (root mean square) emittance* ε_{rms} that can be used to write the ellipse equation:

$$\gamma_x x^2 + 2\alpha_x x x' + \beta_x x'^2 = \varepsilon_{x,rms} \,. \tag{2.5}$$

Where the ellipse projections on the x and x' axes are equal to the rms values of the beam width σ_x and the divergence angle $\sigma_{x'}$ of the distribution:

$$\begin{cases} \sigma_x = \sqrt{\beta_x \varepsilon_{x,rms}} \\ \sigma_{x'} = \sqrt{\gamma_x \varepsilon_{x,rms}} \end{cases}. \tag{2.6}$$

Therefore the rms emittance can be defined in terms of second moments of the distribution [Ferrario 2012], like:

$$\varepsilon_{rms} = \sqrt{\sigma_x^2 \sigma_{x'}^2 - \sigma_{xx'}^2} \,. \tag{2.7}$$

Contrary to the first definition of the emittance, the rms emittance is different from zero for each non perfectly laminar beam, so even in the case of Figure 2.6 (b) where the relationship between the angle and the position in the phase space is not linear, the distribution is a line with a null phase space area. This because the rms emittance depends not only on the area occupied by the beam in phase space but also on the distortions produced by non-linear forces.

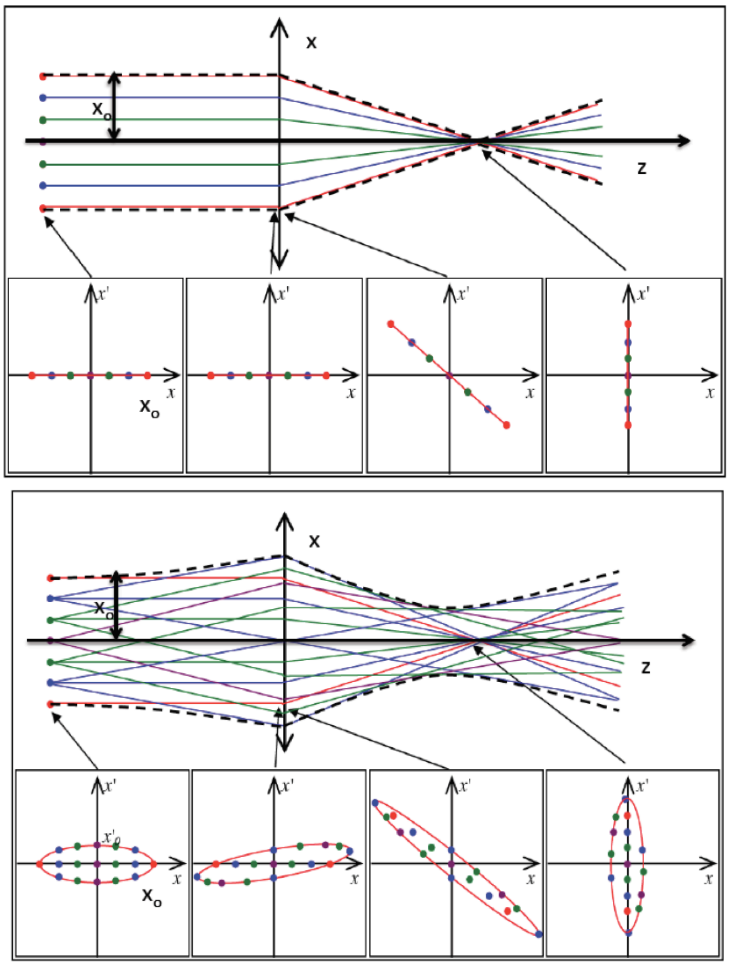

Figure 2.8 *Particle trajectories and phase space evolution of a laminar beam (top) and non-laminar beam (below).*

For an accelerated beam it is better to consider the normalized rms emittance, for which the transverse momentum p_x is used instead of the angle divergence x'. Indeed the transverse momentum is independent from the longitudinal acceleration, while the angle divergence is reduced during acceleration because $x' = p_x/p$. Therefore, the acceleration reduces the un-normalized emittance but this does not affect the normalized emittance, which for small energy spread can be approximated to: $\varepsilon_{n,rms} = \beta\gamma\varepsilon_{rms}$ with β, γ the relativistic factors.

The possibility to have information about the laminarity of a particle beam through the emittance is an important asset while the beam is being accelerated, transported or focused. Indeed, only an ideal laminar beam can be focused in one point using an ideal focusing element that keeps the beam laminar as shown in Figure 2.8 (top). If the beam propagates completely parallel to the propagation axis z, it means that all particles of the beam have zero transverse velocity. Without taking into account collisions and inner forces (like Coulomb forces) a parallel beam could propagate with no change in its transverse width. If this beam passes

through an ideal lens it is transformed in a converging laminar beam where the transverse velocities after the linear lens are proportional to the transverse position x and all the orbits converge to a single point. After passing through the focal point, the particles follow diverging laminar orbits.

In theory a non-laminar beam can be made to converge in a single point only if it is of the type of Figure 2.6 (a), while if the particles have a random distribution of transverse velocities at the same location and a spread in direction as in Figure 2.6 (b), it is impossible to focus all particles from a location in the beam toward a common point. A lens can influence only the average motion of the particles. This case is illustrated in Figure 2.8 (below) where the focal spot limitations are evidenced [Ferrario 2012].

Several authors carried out studies about the emittance of a TNSA proton beam [Cowan *et al.*, 2004], [Kemp *et al.*, 2007], [Cowan *et al.*, 2011].

For proton energies higher than 10 MeV in [Cowan *et al.*, 2004] a transverse normalized rms emittance $< 0.004\ mm\ mra$ has been measured and a longitudinal normalized rms emittance of $10^4\ eV\ s$. These values are at least 100-fold and maybe as much as 10^4-fold better than conventional accelerator beams.

In [Schollmeier thesis 2008] some experimental results for the emittance at different laser facilities were presented. The transverse phase space plots recorded at three laser systems TRIDENT, LULI-100 TW and Z-Petawatt are shown in Figure 2.9. The plots exhibit a different slope for each proton energy.

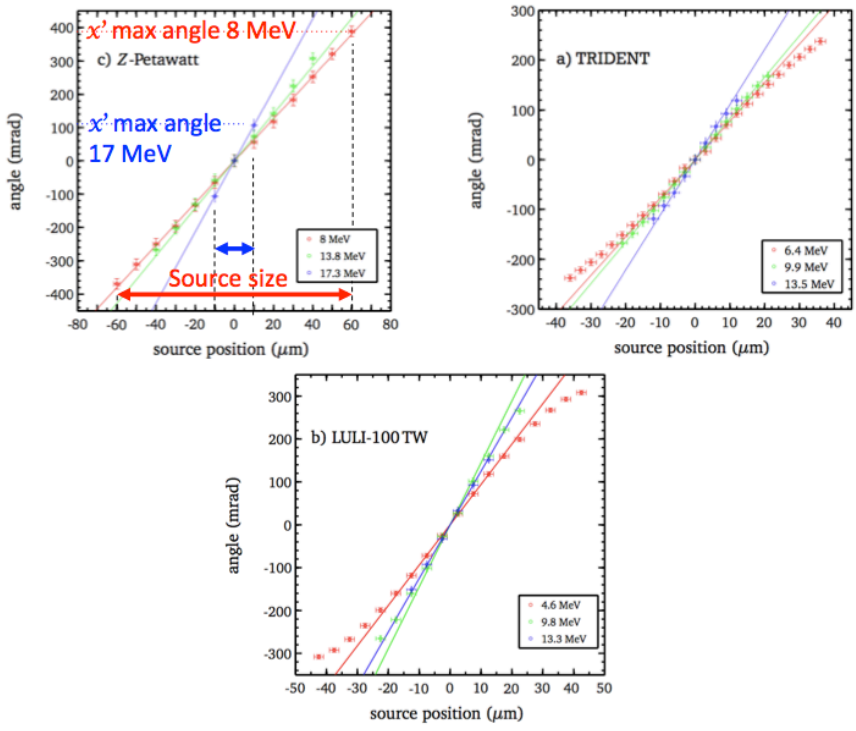

Figure 2.9 *Energy-resolved transverse phase space, for three TNSA proton beams at three different laser facilities.*

Maximum Proton Divergence

As said, each energy of the forward proton beam corresponds to a different dimension of the emission zone on the target (source size). From this emission zone the protons are ejected as a diverging beam. The divergence of the beam, for each proton energy, can be represented by the maximum *half-angle* divergence, that is a function of the proton energy E_p. Indeed, the high-energy protons are emitted from the smallest zone with the lowest divergence angle. As the energy decreases, the maximum divergence angle increases, up to the low energy protons that are emitted from the largest zone (that is the wings of the sheath) and again present a low divergence angle (see Figure 2.10).

A detailed study of the divergence half angle as a function of the proton energy E_p has been realized by [Mancic et al., 2010], [Mancic Thesis 2010]. There the trend of the divergence half angle for several TNSA proton beams is shown and a general fit for the experimental data is proposed:

$$Half\ Angle\ (E) = p_0 + p_1 E + p_2 E^2 + p_3 E^3 + p_4 E^4. \qquad (2.8)$$

With the coefficient values: $p_0 = 5.0778$, $p_1 = 121.61$, $p_2 = -321.33$, $p_3 = 344.33$ and $p_4 = -150.46$ and $E = E_p/E_{pMAX}$ (see Figure 2.11 (right)).

In Figure 2.11 (left) from [Nurnberg *et al.*, 2009], the behaviour of the divergence is shown for three different laser facilities and experimental conditions. For each of these experimental data the same decreasing trend can be identified.

This angular distribution can be modified by bending the target surface [Bartal et al., 2011], by choosing a particular structure of the target rear surface [Roth et al., 2002] or the structure of the laser focal spot [Fuchs et al., 2003].

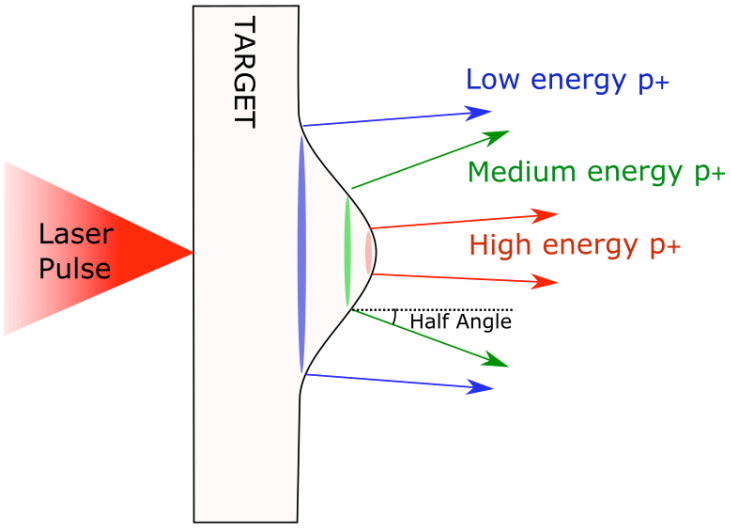

Figure 2.10 *Scheme of the emission of different proton energies.*

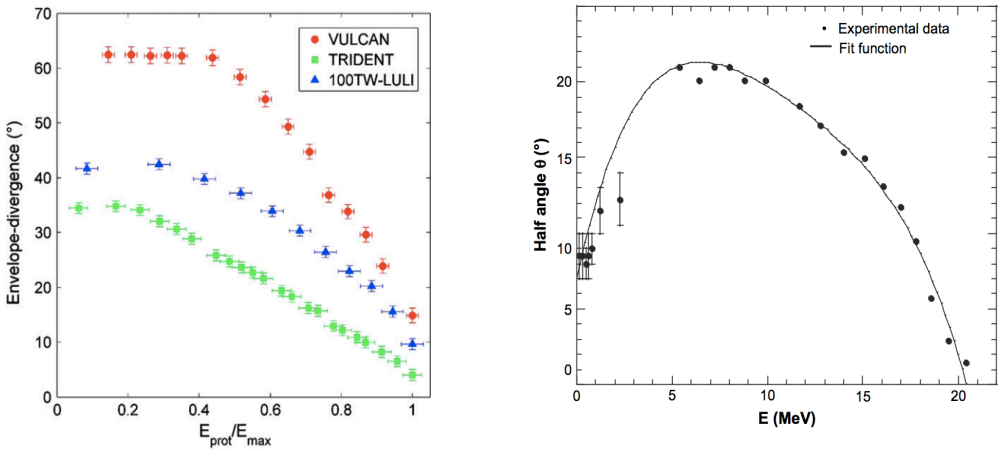

Figure 2.11 *Energy-dependence of the half-angle. (left): experimental data obtained at TRIDENT (green), at LULI- 100TW (blue) and at VULCAN (red) [Nurnberg et al., 2009]. (right): experimental data and fit (equation (2.8)) from [Mancic Thesis 2010].*

2.1.2 Step 2: Selection of a Part of the Produced Proton Spectrum via Laser-triggered Micro-lens

We were interested to obtain a modification of the TNSA proton beam accelerated in step 1 using a laser-triggered micro lens device. In this section the operating principle of this lens will be discussed.

The name ***laser-triggered micro lens*** describes a very easy and cheap device, that has been tested for the first time by [Toncian *et al.* 2006] at LULI and better characterized in [Toncian *et al.* 2011].

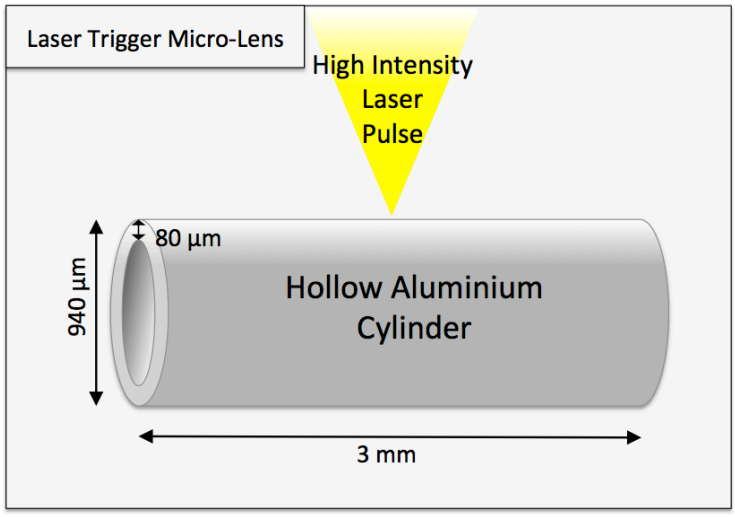

Figure 2.12 *Scheme of the laser-triggered micro lens with the typical dimensions used in the past as well as in our experimental campaigns described in chapter 3.*

The “lens” is nothing more than a hollow aluminium cylinder; it can be for example a section of what is used for medical syringes. Its dimensions in the past experiments were of few millimetres in length for a diameter of about 1 mm (see Figure 2.12). On the external wall of this cylinder a high intensity laser pulse is focused that generates a transient electric field inside the cylinder. This field is able to focus positive charges passing through.

Since the electric field inside the cylinder is transient, the focalization is effective only for a particular range of energies for the protons that pass through the cylinder while the electric field is operating. Due to the energy spread of the different protons accelerated (related to the beam longitudinal emittance), the beam undergoes a debunching while propagating from the source. Each energy pass through the cylinder at a different moment and is therefore subject to a different electric field. For these reasons, the characteristics of the focalization are different for each range of energy.

Using this device it is possible to focus a TNSA proton beam. Three principal parameters can be modified to control the characteristics of the focusing process:

- **The distance between the proton source and the beginning of the cylinder.** If the proton source passing though the lens is a TNSA proton source, it is not monochromatic (see the broadband energy spectra of Figure 2.2) and it has a characteristic beam divergence (see Figure 2.11). Since the beam is composed of various proton energies, each energy has a different times of flight and, therefore, reaches the cylinder at different moments. The bigger is the distance between the cylinder entrance and the proton generation zone, the bigger will be the energy spread and, therefore, the range of involved energies will be narrower. On the other hand, depending on the diameter of the cylinder and the proton divergence, starting from a certain distance it will not be possible to collect all the protons of the beam but only a part of them (see Figure 2.13).
- **The timing between the principal laser beam and the trigger laser beam.** The evolution of the electric field inside the cylinder is triggered by a second laser beam, so it is possible to control the moment when the effect of the focusing E field starts by controlling the delay between the two laser beams (the main beam and the trigger beam). If the high-energy protons cross the cylinder before it is irradiated by the trigger laser beam that generates the focalizing fields, they do not undergo any focalizing effect. Protons with a slightly lower energy, synchronized with the focalizing E fields will undergo the maximum effect.

- **<u>The intensity of the laser beam acting on the cylinder</u>**
  The electric field generated inside the cylinder depends on the intensity of the laser focused on his external wall, so varying its intensity it is possible in principle to control the amplitude of the electric field inside the cylinder.

Choosing the delay between the laser beam accelerating the protons and the one triggering the lens, or choosing the distance between the protons source and the lens beginning, it is possible to tune which range of proton energies will be focused. For these reasons the lens can be considered *tunable*.

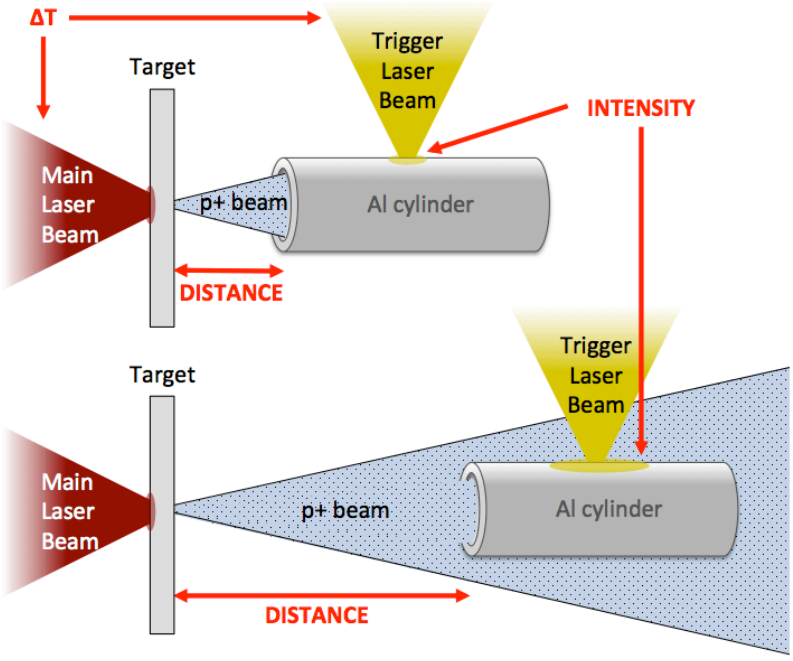

Figure 2.13 *In the figure, the three principal parameters that allow to control the micro lens are evidenced in red.*

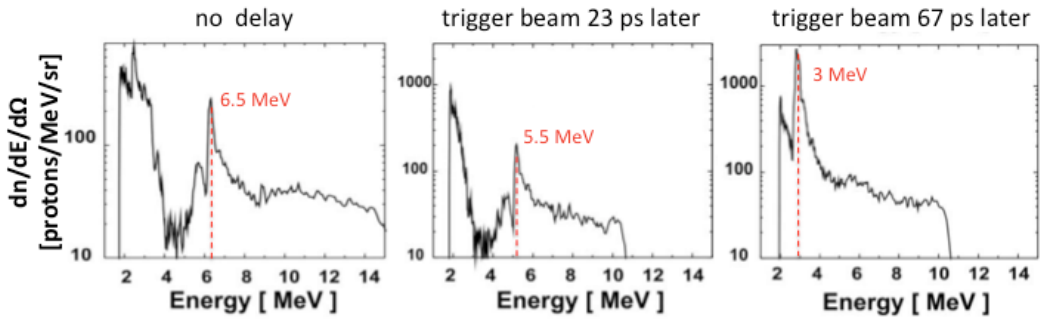

Figure 2.14 *Three experimental spectra of a proton beam passed through the micro lens, with three different timings between the two laser beams (no delay, 23 ps, 67 ps).*

The proton energy spectrum measured after a slit by a magnetic spectrometer is shown in [Toncian *et al.* 2011]. The spectrum does not present the typical quasi-exponential decay, but it evidences a peak in correspondence to the range of proton energies that have been focused close to the entrance slit of the spectrometer. On the other hand, the dip seen at lower energy, just before the peak, may correspond to protons with a large divergence following a strong focusing far from the slit.

The three spectra shown in Figure 2.14 give experimental evidence that the desired location of the peak of a proton energy can be tuned selectively, allowing to tailor the energy distribution of the transmitted beam.

A theoretical model to describe the evolution of the electric field inside the cylinder has been proposed by [Goerdienko *et al.*, 2006]. According to this model, the laser pulse, that hits the external wall of the cylinder generates a population of hot electrons with enough energy to penetrate through the solid metal wall and to spread over the inner surface of the cylinder. In an initial stage, at the rear side of the interaction region (the internal wall), the electrons build up, as in the TNSA process, a strong electric sheath field E_s, leading to ion acceleration.

A fraction of the electrons will be electrostatically trapped thus returning towards the surface. A fountain like motion of electrons can be imagined that drives a strong transverse magnetic field $B_\perp$. This field is excited perpendicular to the plane of motion. This field propagates at the speed of light following the hot electrons. At the same time the electrons are pushed sideways by the Lorentz force in the direction of $E_s \times B_\perp$, increasing the extension of these fields. While these fields extend, the surface is ionized and a plasma layer with high electron temperature T_e and low ion temperature T_i is created. This plasma begins to expand into the vacuum toward the cylinder axis according to the TNSA mechanism.

In the expanding plasma two zones can be distinguished:

- The front of this expanding plasma is the so-called *non-quasineutral edge* or ***ion front***. It is estimated [Mora 2003] to be on the order of the Debye length $\lambda_D = \sqrt{\varepsilon_0 k_B T_e / n_{e0} e^2}$.
- The ***quasi-neutral zone*** that follows the front.

The hypothesis that $\lambda_D \ll R$, with R the radius of the cylinder, coincides with the quasineutrality condition, for which the Debye sheath layer is narrow.

Because of the narrowness of this non-quasineutral edge field, only a small amount of ions of the beam transiting through the lens (on the order of $\lambda_D / R \ll 1$) would be influenced by it. This influence can be neglected.

Therefore, to describe the focusing, it is relevant to study the properties of the quasi-neutral zone of the expanding plasma. For the quasineutrality to be ensured, the electron and ion density must be balanced $n_e \approx Z_i n_i$ (where Z_i is the ion charge state).

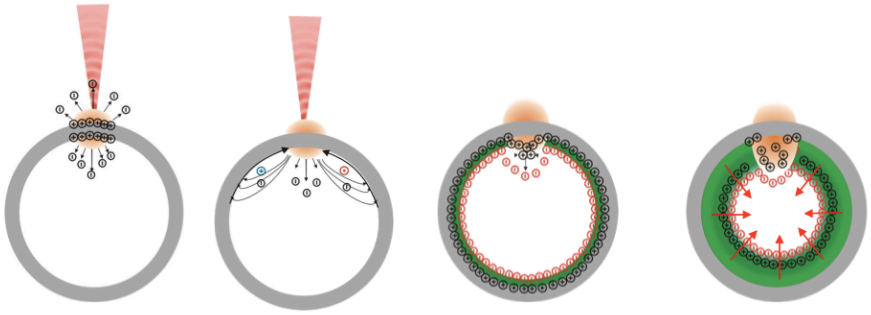

Figure 2.15 *Phases of the plasma expansion inside the cylinder: (1) The laser pulse hits the external wall of the cylinder and a hot electron population is generated. (2) The hot electrons spread on the inner surface of the cylinder. (3) Start of the plasma expansion.(4) The ion front leads the plasma expansion followed by the quasi-neutral zone (green) [Toncian et al., 2011].*

The plasma density and therefore the electron pressure $P_e = n_e k_B T_e$ vary along the cylinder radius.

Due to the space charge separation inside the quasi-neutral zone, a radial electric field is generated that counterbalances the pressure gradient:

$$E = -\frac{1}{en_e}\nabla P_e \,. \tag{2.9}$$

As the electron pressure gradient is directed outwards, the generated electric field is directed towards the cylinder axis. According to the model, it is this field that focuses the ions passing through the cylinder. This field is transient and its duration is depending on the plasma expansion duration.

For a correct operating principle of the lens, the focusing electric field inside the cylinder must be symmetric. In order to develop a symmetric field, that is a symmetric expansion of the plasma, two conditions must be verified.

First the hot electrons must spread on the inner wall on a time shorter than the plasma expansion time inside the cylinder. Indeed the laser pulse is focused on one side of the hollow cylinder, where the electrons are generated. As said the electrons spread on the inner surface at nearly the light velocity c, while the plasma expansion directed towards the cylinder axis begins with the ion sound velocity $c_s = \sqrt{Z_i k_B T_e / m_i}$. Therefore the characteristic time of radial plasma expansion is on the order of $\tau = R/c_s$, while the hot electrons spreading time is $\tau_s = \sqrt{(\pi R)^2 + (L/2)^2}/c$, with R and L being the radius and the length of the cylinder respectively. The cylindrical symmetry is satisfied since we always have $\tau \gg \tau_s$.

The second condition for the formation of symmetric fields is that the collisional cooling of the electrons does not hamper their spreading, and this can be assumed to be true if the radius of the cylinder: $R < \frac{c}{\nu_e \pi}$, where ν_e is the

Coulomb collision frequency for moderately relativistic electrons and the R radius of the cylinder. For an electron temperature $T_e = 1\ MeV$ and a hot electron density of $n_e = 10^{24}\ cm^{-3}$ this corresponds to a condition of $R \lesssim 3\ mm$.

The 2D simulations realized with the PIC code PSC and presented in [Toncian *et al.*, 2011] confirm the validity of the model described above (see Figure 2.16). In the simulations the presence of a small exponential pre-plasma around the cylinder is considered. For a laser intensity of $I = 5{\times}10^{18}\ W/cm^2$, the electron temperature has been estimated to be $T_e \approx 580\ keV$.

The electric fields seen in the simulations are correctly described with the analytical model of a plasma expanding into the vacuum that can be used for scaling. For the simulations, if the laser intensity is increased up to $10^{21}\ W/cm^2$, the electric field generated inside the cylinder would be able to focus up to 240 MeV energy protons.

The results of particle tracing simulations are shown in [d'Humieres 2012] and [d'Humieres *et al.*, 2006]. The simulations describe the trajectories of 100 protons while passing through the cylinder at different temporal stages. The electric field for each stage is obtained from PIC simulations similar as the ones shown in Figure 2.16. The distance between the proton source and the cylinder entrance was 4 mm and the cylinder length was 3 mm. The hot electron density was considered equal to $6{\times}10^{-5}n_c$, where n_c is the critical density at $\lambda = 1\ \mu m$.

In Figure 2.17, the trajectories of protons with three energies are presented. The 7.6 MeV energy protons on the right are not focalized since they pass inside the cylinder too early. The 6.25 MeV protons are close to the exit of the cylinder when it is irradiated, sustain small fields and are therefore well collimated over a long distance. The 4.9 MeV protons are at the middle of the cylinder when it is irradiated, they therefore sustain fields much stronger than the 6.25 MeV and are focalized at a short distance (5 mm) from the cylinder and then strongly diverge.

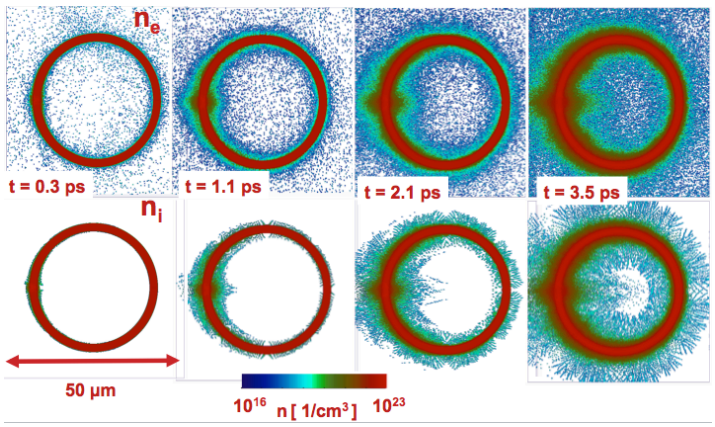

Figure 2.16 *2D simulations realized with the PIC code PSC, from [Toncian et al., 2011]. Simulation parameters:* $I = 5{\times}10^{18}\ W/cm^2$, *pulse duration* $350\ fs$.

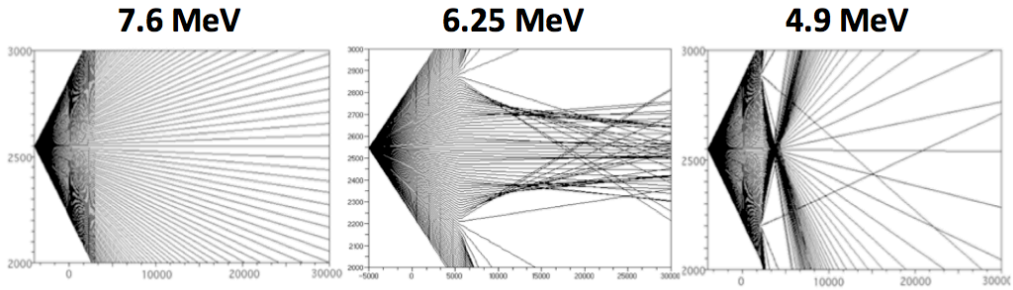

Figure 2.17 *Simulations from [d'Humieres 2012]. Protons of different energies transiting through the cylinder. The cylinder, which had a thickness of 50 μm, was irradiated by a laser pulse at an intensity* $3\times10^{18}\ W\,cm^{-2}$*, and with a pulse duration of 350 fs.*

The micro-lens is not the only device studied during the past years to focus and/or select the broadband TNSA proton beam.

Another possibility to focus and select a TNSA proton beam has been proposed by [Schollmeier *et al.*, 2008] where the use of a permanent magnet miniature quadruplole lens has been tested. This technology has the advantage, compared to the micro lens, that it does not need to be replaced and aligned at every shot. Indeed the cylinder is destroyed on each shot. On the other hand, the disadvantages are that this technology is not tunable shot by shot to adjust the focus of a particular energy proton and that the transmission through the magnets is low (0.1%). The device is composed in this case of two permanent magnet quadrupoles (PMQ); the first focuses the beam in one plane and defocuses the protons in the perpendicular one, the second PMQ focuses on the other plane but the second aperture cuts a part of the beam (see Figure 2.18).

[Nishiuchi *et al.* 2009] have obtained an increase of the measured transmitted proton beam increasing the aperture of the PMQ (from 5 mm to 50 mm). The first PMQ had an acceptance half-angle of 10°, which was similar to the whole proton beam divergence; however, the beam was still partly clipped by the second PMQ, giving an overall transmission of 30%. They obtained a quasi-monoenergetic proton spectra after the PMQs with an energy of 2.4 ± 0.1 MeV (see Figure 2.19).

[Roth *et al.* 2009] and [Harres *et al.* 2010] alternatively demonstrated the collimation of a 2.5 MeV laser-proton beam with a solenoid magnet (7 cm long, 4 cm diameter, 8 T) that has the advantage to have a collection effiency of almost 100%. However [Harres *et al.* 2010] pointed out that the electrons co-moving with the protons are focused inside the solenoid and this causes a space charge effect.

A compact broadband ion beam focusing device based on laser-driven MG thermoelectric magnetic fields is been designed by [Albertazzi *et al.*, 2015]. they have shown that ~10 MG, long-lived, surface toroidal magnetic field can be produced by high intensity, high contrast laser irradiating a solid target.

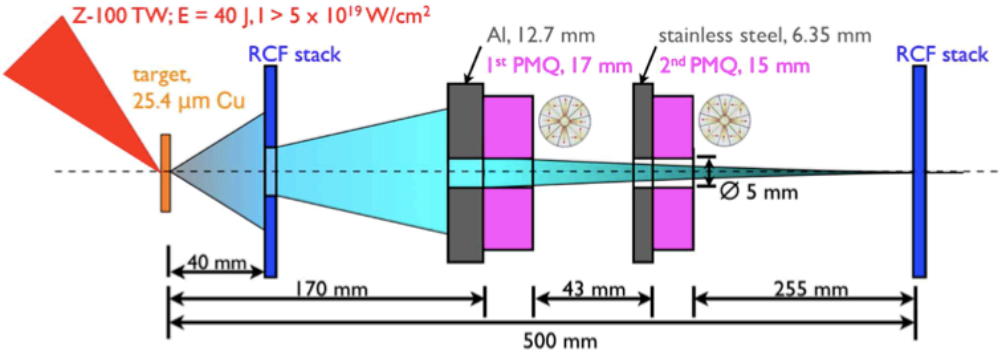

Figure 2.18 *Set-up of [Schollmeier* et al.*, 2008] device, composed by two permanent magnet quadrupoles (PMQ).*

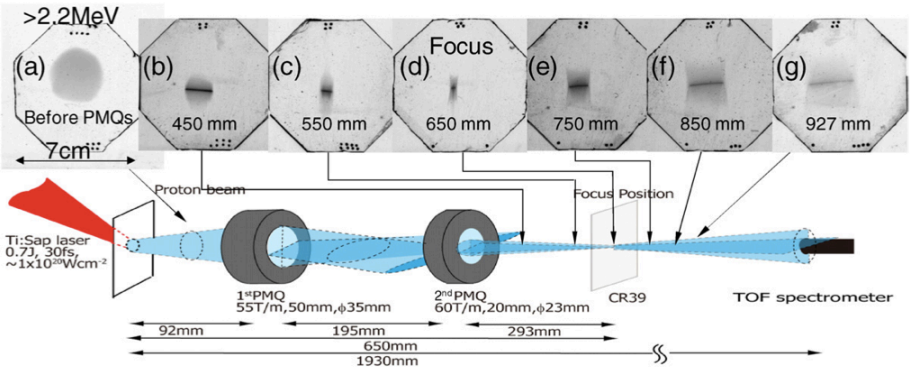

Figure 2.19 *[Nishiuchi* et al. *2009] set-up. The octagonal frames show the proton beam profiles recorded with the CR-39 nuclear track detectors, the darker regions correspond to higher proton density. (a) The original beam profile before the PMQs (Al 40 μm filter, 1.9–2.8 MeV protons). (b)–(g) Proton beam profiles (2.2–3.1 MeV) at indicated distances from the target. At the best focus (d), the visible beam size is 3 mm × 8 mm; however, these dimensions are overestimated due to CR-39 saturation at the image centre.*

This toroidal magnetic field can be used to capture and refocus a large energy range of diverging, laser-produced protons. Effective control of proton focusing can be directly achieved by varying (i) the delay between the laser pulse that produces the protons beams and the laser pulse which is used to generate the self-generated magnetic field, (ii) the material of the target onto which the B fields are generated, and (iii) the target thickness. However, using a TNSA proton beams, the device does not allow the capture of the entire divergent proton beam from the source.

A simplification of the micro lens device has been proposed by [Kar *et al.*, 2008] by incorporating the lens on the principal target and avoiding in this way the necessity to use the second laser beam. The micro lens is charged by the main laser pulse and the electric field is generated by the hot electrons that escape from the Debye sheath accelerating the protons and then spread along the

cylinder surface. This simplification makes it also more easy to align and set-up the device, which is an interesting benefit for future high repetion rate laser facilities. The drawback is that the tunability of the lens is lost like in the PMQ and solenoid magnet case.

In conclusion, as summarized in the Table 2.1 below, the micro lens is the only device that allows the tunability of the focused energy of the proton together with the possibility to collect the entire proton beam. For these reasons it has been the one chosen for our experiments. In the table the principal advantages and disadvantages of the use of this device are summarized.

During the experimental campaign we carried out, two set-ups have been tested to achieve a modification of the energy spectrum of the proton produced by TNSA using the laser triggered micro lens.

Since the lens focuses only a range of energies, only this range of energies is collimated over a long distance, therefore the spatial distribution of the energy spectrum over a long distance will be modified. This approach has been used in the ELFIE experiment described in § 3.1 of this thesis.

In the second set-up, the use of a pinhole has been tested. In theory, it is possible to put a pinhole at the focus point of the desired proton energy in order to cut the unwanted part of the spectrum. This approach is discussed in the § 3.2 of this thesis, where the results of the second experimental campaign in TITAN are presented.

Laser triggered micro lens features

Advantages	Disadvantages
Compactness (mm instead of dm)	Each alignment is for a single use
Tunable	Two laser beams are needed to preserve the tunability
Capability of focusing beams of several A instead of several mA	
Focusing and selecting in energy with the same device	
Low-cost device	

Table 2.1 *Advantages and disadvantages of the micro lens.*

2.1.3 Step 3: Comparison between the Neutrons Produced using the Full Proton Spectrum or the Selected One

As already mentioned, the first two objectives of our investigation were to generate a TNSA proton beam with a typical broadband energy spectrum (step 1) and to collimate and select part of this spectrum using a laser-triggered micro lens (step 2).

The purpose of step 3 was to use the pitcher catcher set-up described in § 1.3.1 to generate a neutron source. The initial idea was to send the two proton beams, generated in step 1 and step 2 respectively, on a catcher of appropriate material in order to obtain neutrons, and then to achieve a comparison between the neutron signals produced with the full proton spectrum (step 1) and the selected one (step 2).

The material chosen for the catcher was ***lithium fluoride*** (**LiF**). Each sample of LiF is composed of 50% of atoms of lithium (Li) and 50% of atoms of fluorine (F).

Natural lithium is composed of two stable isotopes: ***lithium-6*** (**^{6}Li**) with a natural abundance of 7.5% and ***lithium-7*** (**^{7}Li**) that has the higher natural abundance of 92.5%. Both isotopes have anomalously low nuclear binding energy per nucleon[1] compared to the next lighter and heavier elements, *helium-4* (^{4}He) and *beryllium-7* (^{7}Be), which means that among stable light elements, lithium is the only one that can produce net energy through nuclear fission. Therefore, the nuclei of lithium are really reactive and verge on instability. For this reason lithium is a very good catcher material. However, because of its high reactivity, lithium never occurs freely in nature but it only appears in compounds such as LiF. On the other hand, fluorine has 18 known isotopes from ^{14}F to ^{31}F and one isomer (^{18m}F), but only one of these isotopes is stable, that is, ***fluorine-19*** (**^{19}F**). As such, it is a monoisotopic element. Therefore, in order to predict the possible reactions on a LiF catcher when a proton beam impinges on it, one must take into account the (p,n) reaction cross sections of the three isotopes ^{6}Li, ^{7}Li and ^{19}F.

The principal reactions that could be interesting for our investigation are presented in the table of figure 2.21. The Q value for a reaction is the amount of energy released by that reaction (if Q<0 is the energy required for the reaction occur, in the centre of mass system) and the E_p threshold is the minimum proton energy needed to start the reaction.

As will be presented in chapter 3, the maximum cut-off energy of protons for the two experimental campaigns was around 9 MeV for ELFIE and 30 MeV for TITAN.

[1] Only the *deuterium* (^{2}H), the *tritium* (^{3}H) and *helium-3* (^{3}He) have lower binding energies per nucleon than the two stable isotopes of lithium.

Initial	Abundance [%]	Reaction	Final	Q-value [MeV]	E_p Threshold [MeV]
^{7}Li	92.5	(p, n_0)	^{7}Be	-1.644	1.880
		(p, n_1)	$^{7}Be^{*}$	-2.074	2.371
		$(p, 2n_0)$	^{6}Be	-1.232	4.091
^{6}Li	7.5	(p, n_0)	^{6}Be	-5.070	5.919
^{19}F	100	(p, n_0)	^{19}Ne	-4.021	4.235
		$(p, 2n_0)$	^{18}Ne	-15.658	16.489

Table 2.2 *Principal reactions considered in our experimental investigation. Values taken from [NNDC].*

The available cross sections for the reactions presented in the table (Table 2.2) are shown in Figure 2.22. It is possible to note that the highest cross section is that for the reaction $^{7}Li(p,n)^{7}Be$ with a maximum peak of 0.6 $barns$ around 2.2 MeV of incoming proton energy.

The second highest cross section ($0.2\ barns$) is that of $^{19}F(p,2n)^{18}Ne$ reaction for an incoming proton energy of around $30\ MeV$. It is therefore reasonable to assume that the principal nuclear reaction producing neutrons under our experimental conditions was $^{7}Li(p,n)^{7}Be$.

It is important to note that when a neutron source is generated in a laser-plasma environment, not only the foreground neutrons are generated (due to the pitcher-catcher configuration), but also "background" neutrons due to the interactions that take place inside the chamber or from interactions of the primary neutrons with the experimental room. This background signal depends on the experimental set-up and on the hardware present in each experimental room.

As described in § 1.3.1, one interesting feature of the laser-driven neutron source is its potential short duration. It is clear that in order to take advantage of this short duration (e.g. for fast radiography), the produced neutron beam must present some level of monochromacity. Clearly, the monochromaticity that one needs depends on the application (scientific, technical or medical ones). The width of the neutron spectrum and, therefore, the level of the monochromaticity of the neutron source are determined by the thickness of the catcher, the proton spectrum and the cross section.

The $^{7}Li(p,n)^{7}Be$ reaction is one of the most common sources for neutrons because it presents:

- Small kinematic energy spread
- Reasonable neutron intensity
- Simple target production

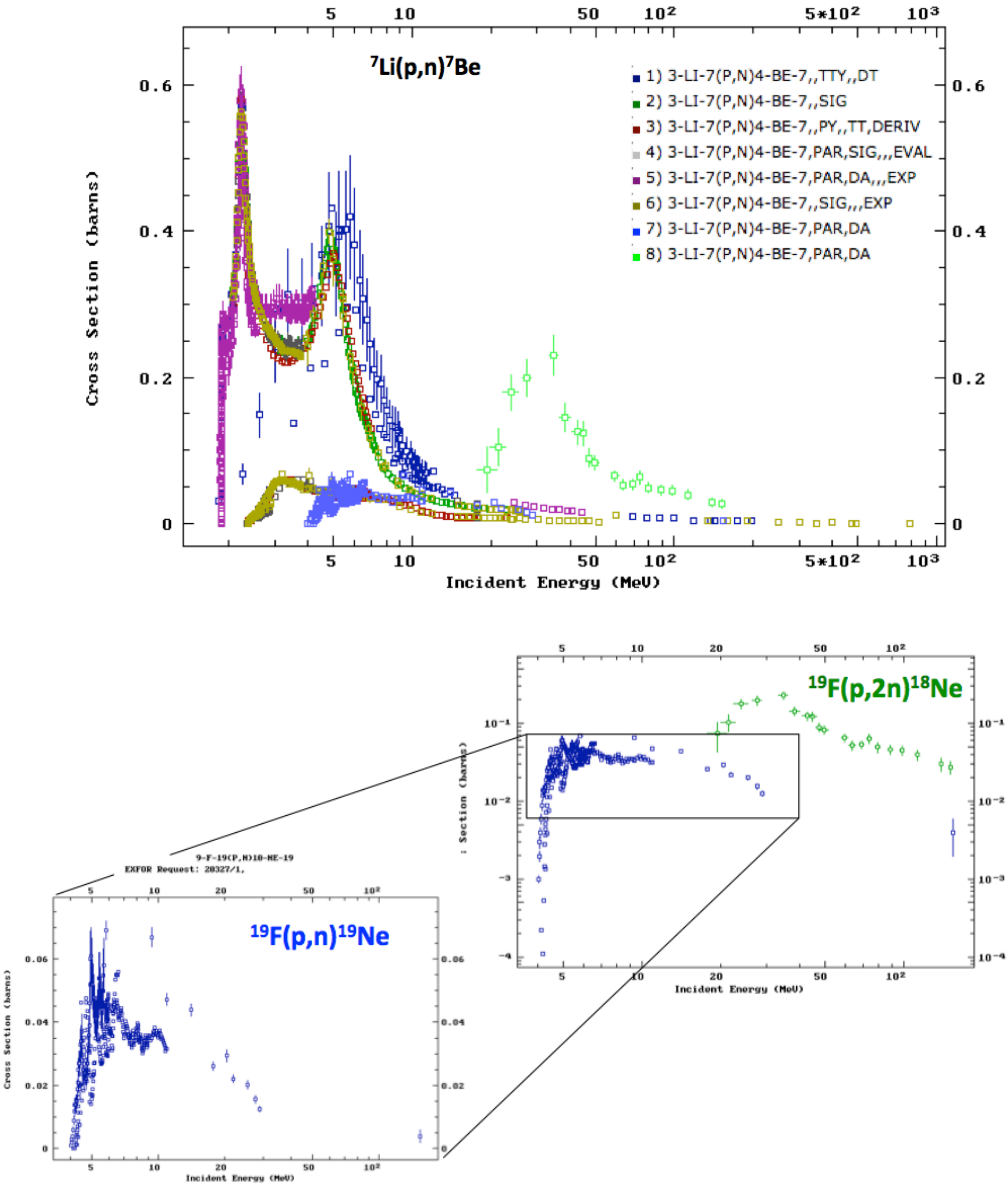

Figure 2.20 *Experimental Nuclear Reaction Data (measured and evaluated) taken from [EXFOR]. (Top) Cross section of the reaction ^{7}Li(p,n). (Below) Cross sections for the reactions ^{19}F(p,n) and ^{19}F(p,2n).*

.

2.2 Description of the Diagnostics

This section describes the diagnostics we used in the two experimental campaigns we carried out, which are both described in the next chapter. The first purpose of our investigation was to modify the spatial energy spectrum of the proton beam using the micro-lens. Therefore we were interested in using diagnostics able to characterize the proton beam formed during the interaction of the high-intensity laser pulse with the proton source target. The other purpose of the experiment was to generate a neutron source through the interaction of the proton beam with the LiF catcher; therefore we devoted some diagnostics to neutron detection.

2.2.1 Proton Diagnostics

To obtain information about the proton beam, two diagnostics were employed: radiochromic films (RCF) and the activation technique.

2.2.1.1 RCF

A radiochromic film is a radiation-dose sensitive film consisting of a single (HD, EBT2) or double layer (MD see below) of radiation-sensitive organic microcrystal monomers, on a thin polyester base with a transparent coating. When the RCFs are exposed to ionizing radiation their colour turns from transparent to different shades of blue (or green/yellow for the EBT2, EBT3 and HD-V2). The darkness of the film increases with the absorbed dose. The absorbed dose is a measure of the energy deposited in the medium by the ionizing radiation per unit mass. It is also known as Total Ionizing Dose TID (equal to the energy deposited per unit mass of medium), which may be measured in joules per kilogram and represented by the equivalent SI unit, Gray (1 Gy=1 J/kg). No processing is required to develop or fix the image, but the films must be handled with care, avoiding dust, fingerprints or bending. It is important to store the films in dry, dark environment with temperature <25°. Any prolonged exposure to UV light should be avoided. The films are insensitive to light at λ>300 nm, but sensitive to UV at lower λ. If a film is exposed to temperatures higher than 60° C or to a saturating dose, it changes its color from blue to red making quantitative data analysis impossible.

The RCFs are used as detectors for protons to measure their energy and angular distributions [Bolton, 2015]. RCFs are sensitive to penetrating protons, which have a large specific energy-loss and produce a high contrast image. Electrons and x-rays generally appear as a diffuse low-intensity low-contrast background that extends over the whole film surface.

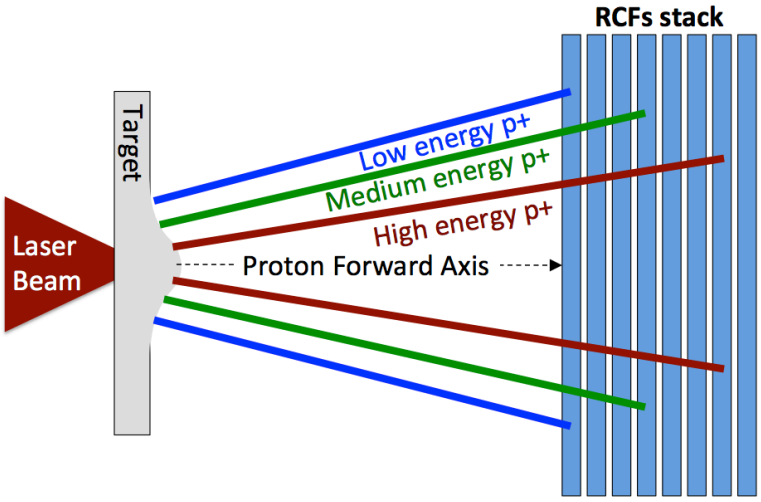

Figure 2.21 *Schematic representation of a TNSA proton beam stopping in a RCF stack.*

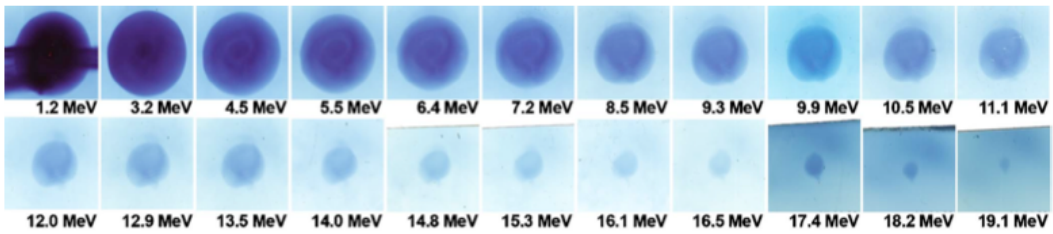

Figure 2.22 *RCF stack of an experiment performed at TRIDENT [Nürnberg et al., 2009]: 19 films of type HD-810 and three films of type MD-55. There was no signal in the following six MD-55 films of the stack. Below each film, the proton Bragg peak energy is given.*

Usually RCFs are used in a multi-layer arrangement that leads to a spectral capability of the detector (*Radiochromic film Imaging Spectroscopy* RIS [Nürnberg *et al.*, 2009]). While the less energetic protons are stopped in the first layers of the stack, high-energy protons can penetrate deeper, reaching the last films. As the energy is released mainly in correspondence to the **Bragg peak** at the end of the proton stopping curves, each layer acts as a filter for the following one and selects the protons whose Bragg peaks are localized within the active layer. Due to the presence of this peak, each RCF layer can be attributed to a small energy interval with a width varying from 0.5 MeV up to 1 MeV depending on the thickness of the active layer. It is important to note that in a multi-layer arrangement the signal observed in the first layers is principally due to the contribution of the low energy protons, but also partially to the high energy protons passing through (see Figure 2.23). To obtain a correct reconstruction of the proton energy spectrum, this has to be taken into account.

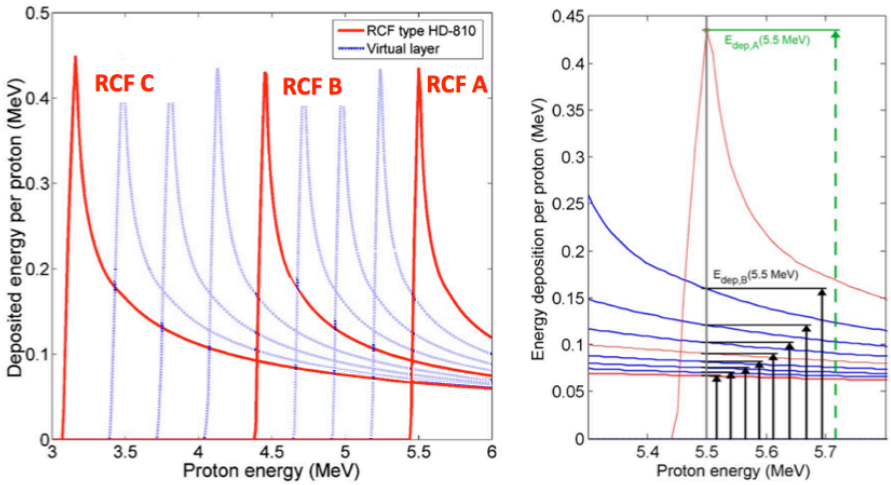

Figure 2.23 *(Right) Energy deposition curves for three consequential HD-810 films (red solid lines): RCF C first layer, RCF B second layer, RCF A third layer. (Left) The 5.5 MeV proton deposits its energy not only in the RCF A but also in the first two layers [Nürnberg et al., 2009].*

More precisely, when exposed to ionizing radiation, the RCF active layer, composed of crystalline di-acetylene, undergoes a solid-state polymerization reaction producing a dye polymer.

The active crystals, which are transparent to visible light, change color to cyan blue when the dye is produced. The amount of polymer produced, i.e. the depth of color change, and hence the optical density, is proportional to the absorbed radiation dose or, equally, to the energy locally deposited by the incoming beam. Due to the sub-micron size of the crystals and to the fact that polymerization does not spread between adjacent microcrystals, the RCF has an extremely high (sub μm^2) spatial resolution.

The films must be digitized for quantitative data analysis. Using a scanner, it is possible to convert the RCFs to a pixel sequence, where each pixel value corresponds to an optical density (OD) that is proportional to the absorbed dose of ionizing radiation. This means that the films must be calibrated for their response to protons and the scanner as well.

Due to their good spatial and spectral resolution and because they are easily handled (no etching is required), RCFs are widely employed for the detection of laser-produced protons. During our experiments four types of RCFs have been used:

- The less sensitive HD-810 and HD-V2 are suitable for high doses, as the abbreviation suggest, therefore, they are usually used at the beginning of the stack to detect the low energy protons, which are usually of higher dose.
- The more sensitive MD-55 and EBT2 are used for moderate doses at the end of the stack to detect the high-energy protons.

MD-55

The MD-55 films have a double active layer between polyester film substrates. The thickness of the active layer can vary slightly from batch-to-batch in order to match the sensitivity specification and to obtain a reproducible response (<10% sensitometric response difference from batch-to-batch). As shown in Figure 2.24, the film structure is symmetric; the film can therefore be used as a detector equally on both sides.

The dose range suggested by the supplier for the current film type is 2-100 Gy.

The inner structure of the film is shown below.

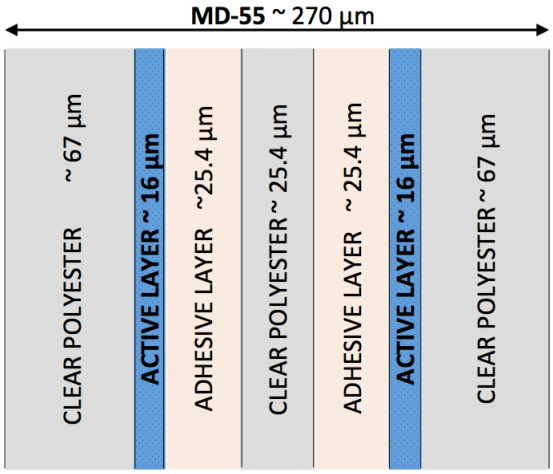

Figure 2.24 *Structure of the inner layers of a MD-55.*

EBT2

The EBT2 films have a wide dose range from 1 cGy to 40 Gy, and, like the MD-55, are more appropriate to detect high-energy protons.

The approximate thicknesses of the different layers are shown in Figure 2.25.

When the active component in the film is exposed to radiation, it reacts to form a blue coloured polymer with absorption maxima at about 636 nm and 585 nm. However, to the human eye, the exposed film will appear green owing to the presence of the yellow marker dye in the active layer.

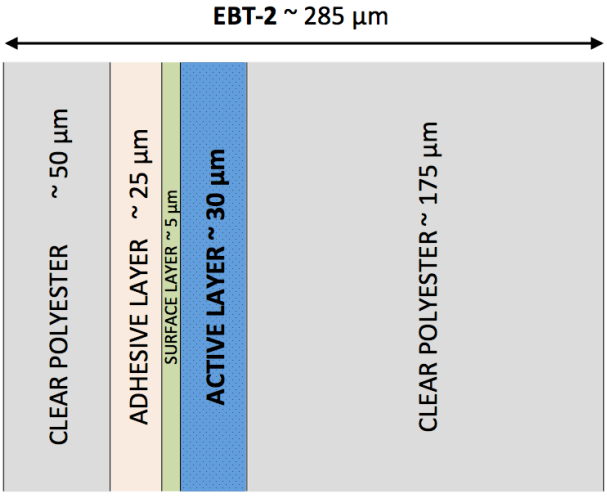

Figure 2.25 *Structure of inner layers of a EBT-2.*

HD-810

As shown in Figure 2.26, the HD-810 films are single layer detectors. This type of RCF is less sensitive to the incident protons than the MD-55 or EBT2 type, and they are suitable for a dose going from 10 to 400 Gy.

Contrary to the MD-55, this type of film has an un-symmetric structure. Therefore there is a difference in the stopping power when using one face compared to the other. For this reason it is necessary to pay a particular attention when the stack is assembled. The films must be put in a consistent way with the same orientation.

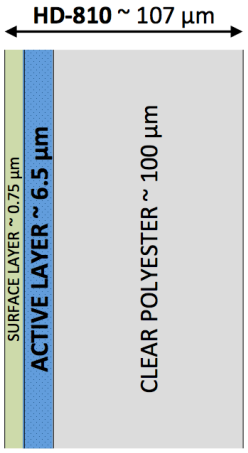

Figure 2.26 *Structure of the inner layers of a HD-810.*

HD-V2

As shown in Figure 2.27, HD-V2 has similar characteristics to HD-810. However, it has a larger dynamic range, namely 10 Gy to 1000 Gy. This film also incorporates a yellow marker dye.

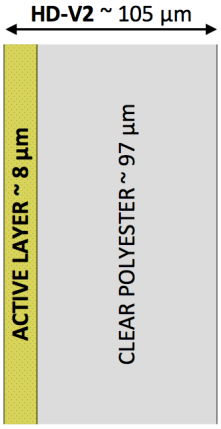

Figure 2.27 *Structure of the inner layers of the HD-V2.*

	Density (g/cm³)	C (%)	H (%)	O (%)	N (%)
Clear Polyester	1.35	45.44	36.36	18.20	0.00
Active Layer	1.08	29.14	56.80	7.12	6.94
Adhesive	1.20	33.33	57.14	9.53	0.00
Surface Layer	1.20	26.61	53.52	11.12	12.75

Table 2.3 *Chemical composition and density of the layers of HD-810 and MD-55 [Schollmeier thesis 2008].*

2.2.1.2 Activation Technique

If the proton energy is larger than several MeV, it is possible to use as well nuclear activation. This technique provides the advantage to overcome the saturation limits of the RCF. Indeed, the optical density of RCF saturates for proton fluxes around 10^{12} particles/cm^2, making a quantitative analysis very difficult under this condition. Moreover the RCF detector system can be destroyed by very high fluxes.

The activation technique is based on the study of the nuclear reactions induced by protons in a sample of a known material. The proton beam impinges on a stack of several layers of this known material. The protons induce nuclear reactions in the different layers of the stack. These reactions have well-known

cross sections and can produce radioactive nuclei. Looking at the decay of these nuclei, it is possible to determine the number of reactions induced in each layer (see § 2.2.2.4 for details). Exactly like for the optical density in the RCF stack, each layer acts as a low energy proton filter for the following ones, therefore, knowing the number of reactions in each layer, it is possible to deduce the initial kinetic energy distribution of the incident protons.

In [Tarisien *et al.*, 2007] the technique is presented for a stack of copper foils in which ^{63}Cu(p,n)^{63}Zn reactions are induced. The ^{63}Zn nuclei are β^+ emitters of short periods which can be detected with a very good signal to noise ratio. Depending on the material chosen for the stack, a reaction threshold is identified. In the case of copper, this threshold is 4.1 MeV; all the protons with lower energies cannot be detected by this technique. The range of energy can be extended using foils of other materials, for instance in foils containing carbon, the nuclear reaction ^{12}C(p,γ)^{13}N for which the energy threshold is much lower can be induced.

In order to unfold the measured data (i.e. the number of decays detected) the ***response function of the stack*** and the ***β^+-decay detection efficiency*** must be known. The *response function of the stack* is the probability that one incident proton of a given energy induces a reaction in one given foil, which can be calculated using the Monte Carlo code SRIM. The β^+ decay occurs inside the nucleus when a proton is converted into a neutron, and a positron (e^+) and an electron neutrino (ν_e) are emitted. It converts an atomic nucleus into a nucleus with atomic number decreased by one:

$$ {}^{A}_{Z}X \longrightarrow {}^{A}_{Z-1}Y + e^+ + \nu_e \,. \qquad (2.10) $$

The positron slows down in the surrounding matter and finally it collides with an electron (e^-). The result of the collision is the annihilation of the electron and the positron, and the creation of two gamma ray photons with energy equal to the electron rest energy ~511 keV, as shown in Figure 2.28.

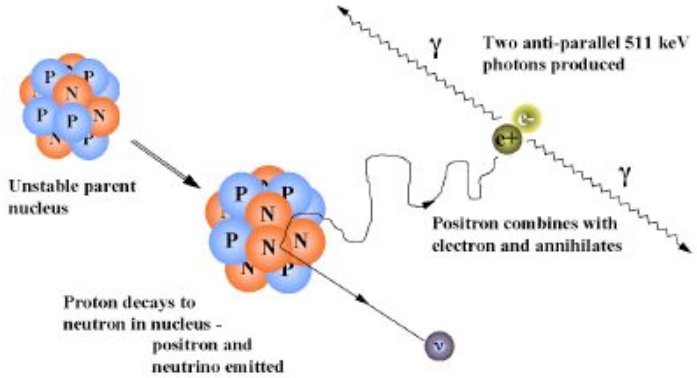

Figure 2.28 *β+ emission and positron annihilation [Badawi 1999].*

These photons can be measured in coincidence using an acquisition system that must allow a good signal to noise ratio. If the signal is due to the annihilation of positrons coming from the decay, the noise is mainly due to the positrons produced by interaction between cosmic ray and the detectors. The *dead time*[1] of the acquisition system must be measured and taken into account to calculate the true counting rates. The efficiency of the counting system can be measured using a calibrated source or can be calculated using a simulation code (e.g. the Monte Carlo code GEANT 4).

We used the activation technique in the second experiment carried out in the TITAN Laser Facility. During our experiments, we also used stacks of RCFs and cupper foils.

A diagnostic system called NATALIE [Tarisien *et al.*, 2011] has been used to measure the β^+ decay.

2.2.2 Neutron Diagnostics

Neutrons do not ionize directly being electrically neutral; hence they are harder to detect directly than charged particles. Furthermore, their motion is only weakly affected by electric and magnetic fields. Therefore, diagnostics used to detect neutrons, through their interaction with matter, are based on indirect methods. Neutrons do not interact directly with the electrons in matter, but they react with the nuclei of materials through **elastic scattering** (producing a recoiling nucleus), **inelastic scattering** (producing an excited nucleus), or **absorption** (with transmutation of the resulting nucleus). As discussed in section 1.1 (c), each of these possible neutron-nucleus interaction has a specific cross section. The cross section is function of the atomic number of the material and of the energy of the incoming neutron. Most detection approaches rely on detecting the various reaction products of these interactions.

Three principal categories can be identified:

- **Absorptive reactions**: mainly for detection of low energy neutrons using materials with high cross sections for neutron absorption. Typical absorber materials include *helium*-3, *lithium*-6, *boron*-10, and *uranium*-235. Each of these materials reacts by emission of high energy ionized particles, the ionization track of which can be detected by a number of means.
- **Activation processes**: the detection can be made by studying the products of the interaction (e.g. neutron capture, spallation) between neutrons and a specific material that must have extremely large cross

[1] The dead time of a detection system that records discrete events is the time after each event during which the system is not able to record another event.

[2] Most of the useful scintillator light comes from recoiling hydrogen nuclei (protons). This

sections for the capture of neutrons within a very narrow band of energy. The reaction products decay later in time, releasing beta particles or gamma rays. Using multiple absorber samples, it is possible to characterize the neutron energy spectrum.

- **Elastic scattering reactions** or **proton-recoil**: high-energy neutrons are typically detected indirectly through elastic scattering reactions. Neutron collide with the nucleus of atoms in the detector, transferring energy to that nucleus and creating an ion, usually a proton. The electrical signal produced by the charged particles can be processed by the detection system. The maximum transfer of energy occurs when the neutron collides with a nucleus of comparable mass, therefore hydrogenous materials are those that maximize the efficiency and are often the preferred medium for such detectors.

The following sections briefly describe the neutron detection techniques used in our experiments.

2.2.2.1 Neutron Time-of-Flight (nTOF) Detection

The Time-of-flight (TOF) technique is a general method for determining the kinetic energy of traveling particles, in our case neutrons, by measuring the time it takes for the particle to fly between two points whose distance is known. This technique is one of the most commonly used to detect high-energy fast neutrons, because it does not entail the moderation of neutrons to thermal energies. The moderation process is usually necessary to achieve a reasonable detection efficiency, but it precludes any opportunity to recover much of the information carried by the neutron source. The time required to moderate neutrons can vary between 1 and 100 μs, depending on the moderating material and their arrangement (a typical moderation time is between 10 and 30 μs).

Therefore, detection approaches that need moderation preclude timing accuracies better than roughly 30 μs [Jordan *et al.*, 2005]. Moderation also destroys information about the energy of individual neutrons because all incident neutrons are moderated to thermal energies before detection. It is still possible to extract neutron spectral information from a moderator-based detection method (e.g., a Bonners sphere set) by exploiting statistical characterization of the dependence of neutron moderation and transport upon incident energy. Such "statistical spectroscopy" devices, however, require measuring relatively large populations of neutrons to reliably reconstruct the incident energy spectrum [Toyokawa *et al.*, 1996]. Contrary to the Bonner spheres, nTOF detectors can also characterize the neutron energy spectra with a limited population of neutrons.

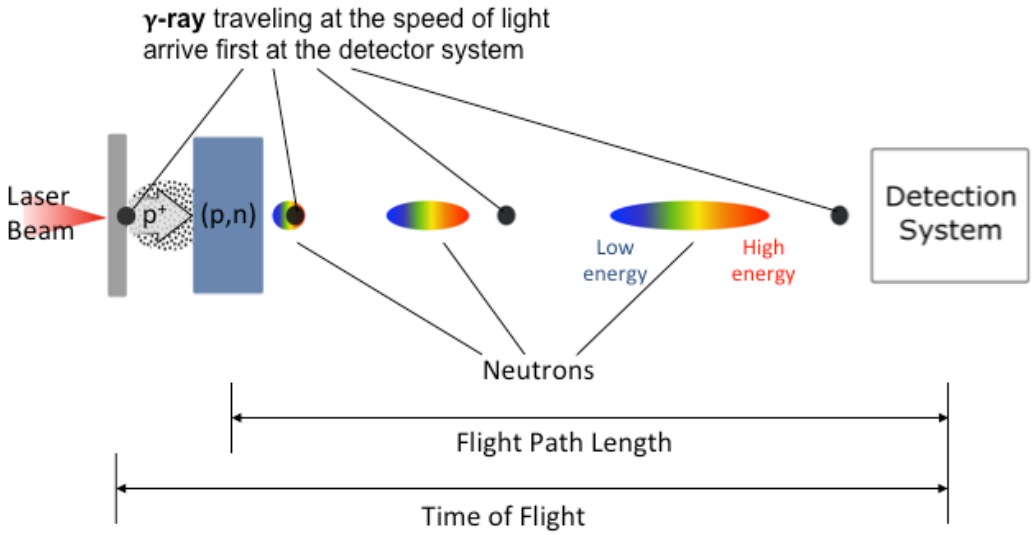

Figure 2.29 *Scheme of the nToF detection.*

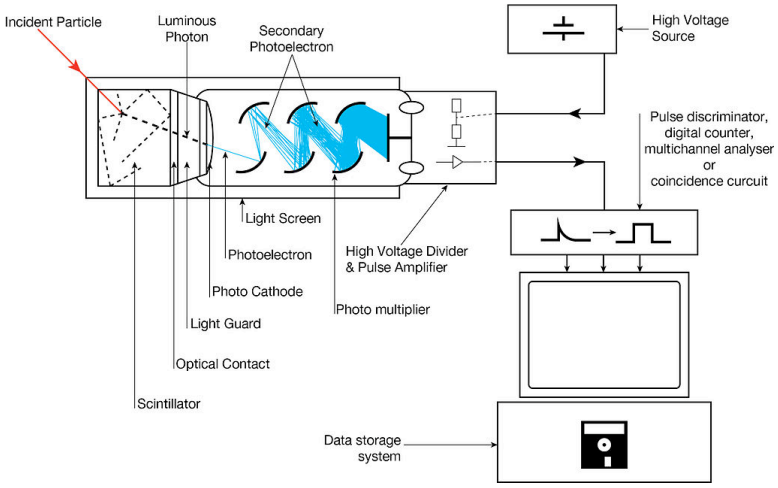

Figure 2.30 *Detection system scheme. Credit [Wikipedia].*

Depending on the distance between the source and the detector, a TOF spectrometer can in principle resolve neutron energies ranging from sub-MeV to hundreds of MeV [Mirfayzi *et al., 2015*]. The detection technique requires that the neutron production happens at a well-defined time, so that it is possible to correlate the detection time of a given neutron with his energy. During our experiment, the pulsed proton beam, which was accelerated from the primary target, produced quasi-simultaneously the neutrons in the catcher. At the same time during the laser plasma interaction in the primary target, a population of hot electron is generated (section 1.4). Only a small fraction (<1%, typically 1 pC charge for 5 J laser energy on the target) of this population escapes from the target [Link *et al.*, 2011]. The majority of the hot electrons goes around and into the target, thus producing an emission of hard X rays and gamma rays via

Bremsstrahlung as the electrons are decelerated. Neutrons and gamma rays travel a certain distance to arrive at the detection system. Because gamma rays travel at the speed of light, they arrive first. As neutrons propagate to the detector, the neutron pulse becomes broader in time with the highest energy neutrons arriving before the lower energy ones (see Figure 2.29). We note that there is no moderation used here.

This allows to define the neutron time of flight from the production target to the detection system as the time between the arrival of gamma rays and the arrival of neutron. Knowing the flight path length L, it is possible to determine the velocity and thus the energy of the neutrons and to reconstruct the neutron energy spectrum of the pulse. The *detection system* (see Figure 2.30) is generally composed of a **scintillator** that is optically coupled to a **photo-multiplier tube** (**PMT**) connected to an **electronic system**. The detection process works as follows: fast neutrons interact in scintillators through elastic scattering with the present nuclei, mostly carbon and hydrogen [2].The kinetic energy of the recoiling protons is absorbed by the scintillator and is ultimately converted to heat and visible light. The visible light is collected by the photomultiplier tube where it is converted to an electric signal using a photocathode[3]. Inside the photomultiplier, the signal is physically amplified by a number of electrodes called *dynodes* where electrons are multiplied by the process of secondary emission. Then the output signal is electronically amplified and processed by an electronic system. The electronic pulse magnitude is ultimately related to the kinetic energy of the recoiling proton.

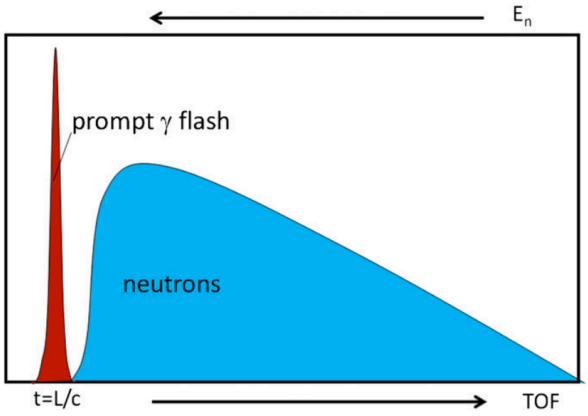

***Figure 2.31** nToF spectrum scheme.*

[2] Most of the useful scintillator light comes from recoiling hydrogen nuclei (protons). This happens because a neutron can transfer 100% of its energy in an elastic scattering interaction to a recoiling proton but only 28% can be transferred to a recoiling ^{12}C nucleus [Knoll 2010].

[3] When a photocathode is struck by a quantum of light, the absorbed energy causes electron emission due to the photoelectric effect.

Gamma photons interact in plastic scintillator via Compton scattering and generate a prompt γ flash before the arrival of the neutron pulse. In Figure 2.31, a schematic spectrum from a nTOF detector is represented.

2.2.2.2 CR-39

CR-39 is a solid-state passive nuclear track detector. It is a popular method to measure particle and neutron radiation due to its low cost, robustness, track permanence and relative insensitivity to electron, gamma rays, UV and X-rays.

CR-39[4] is made of a clear plastic polymer with chemical composition $C_{12}H_{18}O_7$. When a charged particle collides with the polymer structure, it leaves a trail of broken chemical bonds and free radicals along its track within the CR-39 [Séguin *et al.*, 2003]. The amount of local damage along the track is related to the local rate at which the particle loses its energy (dE/dx, where x is the distance along track). The length of the track is the range of the particle in the plastic.

As shown in Figure 2.32, if after the exposition to the ionizing radiation, the CR-39 is immersed in a concentrated alkaline solution (e.g., sodium hydroxide NaOH) hydroxide ions attack and break the polymer structure, etching away the bulk of the plastic at a nominally fixed rate V_B ("*bulk etch rate*").

Whereas along the paths of damage left by charged particle interaction, the concentration of radiation damage allows the chemical agent to attack the polymer more rapidly than it does in the bulk at a faster "*track etch rate*" V_T. So the paths of the charged particle tracks are made visible.

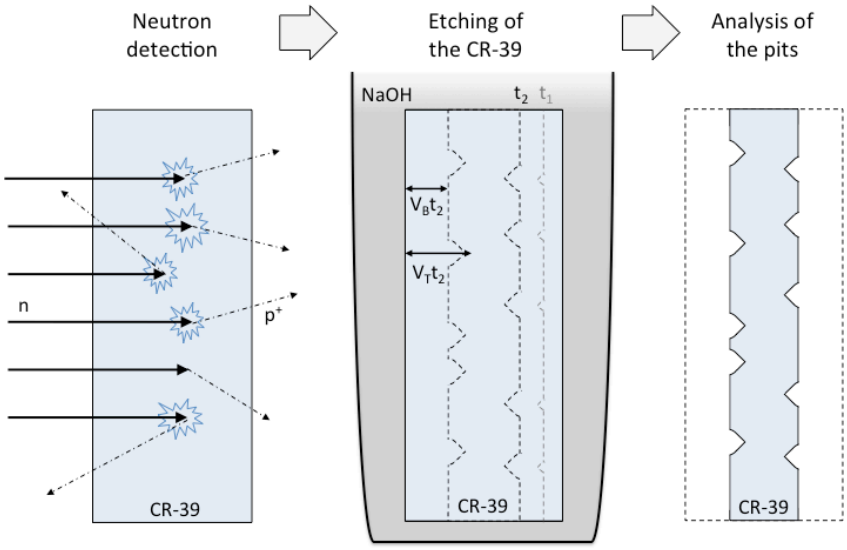

Figure 2.32 *Scheme of neutron detection using CR-39.*

[4] The abbreviation stands for "Columbia Resin #39," because it was the 39th formula of a thermosetting plastic developed by the Columbia Resins project in 1940.

The resulting etched plastic therefore contains a permanent record of the location of the radiation on the plastic, and it also gives spectroscopic information about the source. Track diameters after etching depend on the nature and energy of the ion which has created the track, the NaOH molarity, the NaOH temperature, and the etch time.

After being etched, rinsed and dried, the CR-39 must be analysed using a microscope. From the diameter, the eccentricity and the number of the tracks, it is possible to reconstruct information about the colliding charged particles.

In the case of neutrons one must take into account that they do not directly cause any ionization in the CR-39 detector. The tracks are not produced by neutrons but are a secondary effects due to recoiling nuclei of the detector under neutron impact, leading to the production of charged particles that cause ionization, and consequently, etchable tracks. The most probable way to produce tracks is through the recoil of hydrogen, carbon and oxygen nuclei as well as alpha particles from (n,α) reaction [Castillo *et al.*, 2011].

During our experiment CR-39 detectors were used to obtain information about the neutron flux and have been coupled with the nTOF detectors.

An example of a CR-39 plate after exposure to neutrons and etching is shown in Figure 2.33. The tracks are not round, contrary to what is observed when etching CR-39 exposed to an ion source that penetrates in the CR39 almost under normal incidence, such as when exposing it to a laser-driven ion source. This is due to the fact that the tracks are produced by the recoiled ions, which have trajectories that can be far from normal to the CR39 plate.

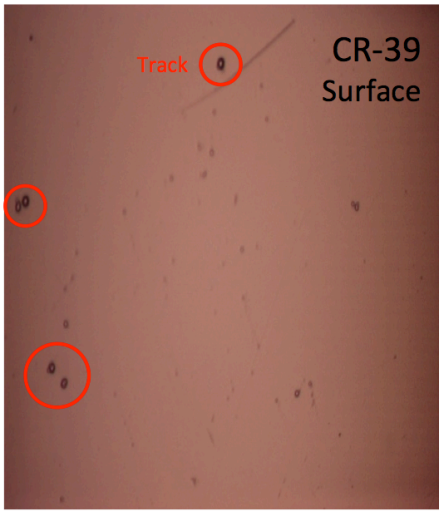

Figure 2.33 *Second CR-39 layer inside the stack used in the ELFIE experiment as observed after 6 hours of etching in 6.0 molarity NaOH at 80°C. The sparse, large, dark rings correspond to tracks induced by ions recoiled after a neutron collision in the CR-39. Visible tracks start to appear after 4 hours, and become obvious after 6 hours of etching. The area covered by the picture is 0.57 mm^2.*

As shown in [Frenje et al., 2002], when CR-39 is used for neutrons detection, the efficiency of track production depends not only on the etching parameters, but also on the side of the plastic that is observed, this is because neutron-scattered ions will generally have a forward-going trajectory, which decreases the number of tracks on the front (facing the neutron source) of the CR-39.

2.2.2.3 Bubble Detector Spectrometers

The neutron flux was also measured with Bubble Detector Spectrometers (BDS) from Bubble Technology Industries. As shown in Figure 2.34, the bubble detector is a tube that contains droplets of a super heated liquid, which is cooled and then suspended in a clear polymer inert gel. The exact chemical compositions of the polymer and of the dispersed liquid are protected by a patent, and the manufacturer (Bubble Technologies Industries Inc., Canada) does not release the information [BDS Manual 2012].

When a neutron passes through one of the droplets it can deposit energy, which serves as a nucleation trigger, causing the liquid to vaporize and create a visible bubble inside the tube. The bubbles can be easily counted by eye, see Figure 2.34. Detectors can be re-used through recompression in a pressure chamber supplied by the manufacturer, allowing to reconvert the gas bubbles to droplets of liquid again.

The detectors provide information on the neutron spectrum over 6 energy bins, detecting neutrons between 10 keV to 20 MeV. Indeed, the BDS consists of six sets of bubble detectors, with all of the detectors in a set being sensitive to a given range of neutron energies (see Table 2.4). The number of bubbles in a tube is a measure of the neutron dose in the energy range of the tube.

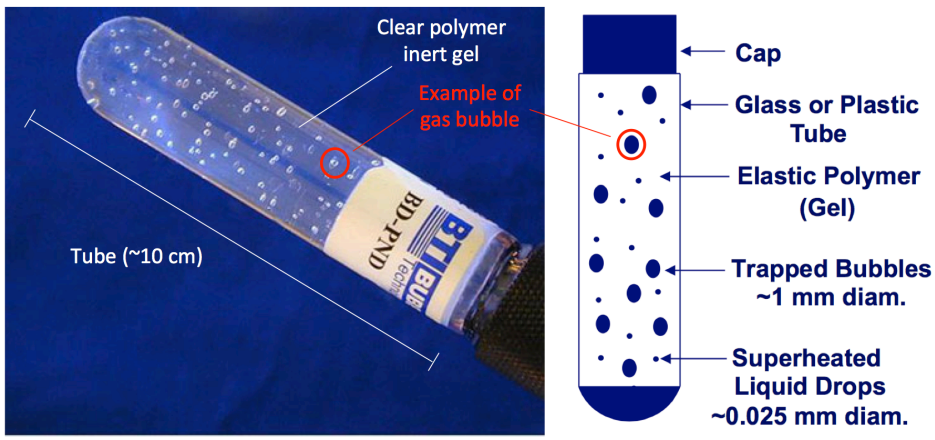

Figure 2.34 *Example of bubble detector tube.*

Each detector has its own normalized response; the curves are shown in Figure 2.35. Using the deconvolution procedure described below, it is possible to determine the neutron flux in the six different energy bins. The average number of bubbles n_i seen in the i-th detector can be related to the total flux of neutron N_j (in n/cm^2) seen by the i-th detector in the j-th region of the histogram via the equation:

$$n_i = \sigma_{ij} N_j \,. \tag{2.11}$$

Where σ_{ij} represents the average cross section of the reaction in a given detector induced by the incident neutrons, i is the index of the detector and j is the index of the region of the histogram seen by the detector.

The process starts with the higher energy range detector, the BDS-10000, which can detect only the highest energy bin of the histogram:

$$n_6 = \sigma_{66} \boldsymbol{N_6} \,. \tag{2.12}$$

Where σ_{66} is the average response of the BDS-10000 over the interval 10-20 MeV. Counting the n_6 bubbles present in the BDS-10000 tube after the interaction, it is possible to obtain the neutron flux $\boldsymbol{N_6}$ for this range of energy and to solve the equation for the next range of energy (2.5-10 MeV):

$$n_5 = \sigma_{55} \boldsymbol{N_5} + \sigma_{56} N_6 \,. \tag{2.13}$$

Where σ_{56} is the sensitivity of the BD-2500 detector over the 10-20 MeV range and σ_{55} is the sensitivity of the same detector over the 2.5-10 MeV range. The flux $\boldsymbol{N_5}$ can be obtained knowing the flux N_6 and the number of bubbles n_5 present in the BD-2500 tube.

Once the deconvolution process is carried out through each of the six areas of the histogram, the neutron flux in the six different energy bins can be obtained.

Tube Name	**BDS-10**	**BDS-100**	**BDS-600**	**BDS-1000**	**BDS-2500**	**BDS-10000**
Energy Range (MeV)	from 0.01 to 0.1	from 0.1 to 0.6	from 0.6 to 1.0	from 1.0 to 2.5	from 2.5 to 10	from 10 to 20

Table 2.4 *Energy bins of the bubble detectors.*

An error for the deconvolved neutron flux can be estimated using the uncertainties in the counts from each group of detectors. The counts in the detectors have an uncertainty equal to the square root of the number of counts observed in the detector. Each bin in the deconvolved neutron spectrum may produce a contribution to its uncertainty that arise from uncertainties from all of the individual bubble counts. After the above procedure is applied, the number of bubbles counted for a single detector are artificially incremented by one standard deviation, and then the deconvolution process is repeated to make an artificial spectrum. The difference between the two unfolded spectra is calculated. For each bin, this yields the uncertainty in the spectrum due to the count from one bubble detector. This can be repeated for all detector sensitivities. Because the counts are statistically independent, so are the calculated differences in each energy bin is the sum-in-quadrature of the difference.

The manufacturers provide the user a spread sheet where inserting the number of bubbles present in each detectors the neutron spectrum is automatically generated using the procedure described above.

The bubble detectors are insensitive to ions, electrons and gamma rays. Therefore, they do not need to be shielded from these radiations. This characteristic makes them really suitable to be used in laser-plasma interaction experiments where the presence of all this background radiation can be very high. However, to have a good statistics, a significant number of bubbles is required. The precision of this detector can be limited in low neutron flux condition ($<10^6$). This is because of the very low value of the normalized response (see Figure 2.35)

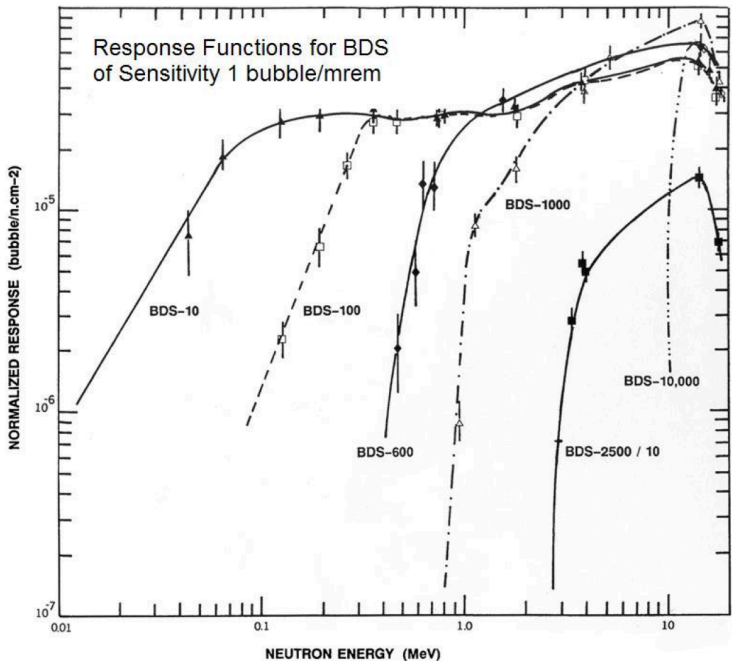

Figure 2.35 *Response function for bubbles detectors as a function of neutron energy [BDS Manual 2012].*

2.2.2.4 Activation

As described for proton detection in section 2.2.1, the study of a neutron source can also be characterized through the radioactivity that is induced by neutron interaction in some materials. A sample of an appropriate material is exposed to a neutron flux for a certain time, it is *activated*, and then the induced radioactivity is counted using an activation counting detector, e.g. a gamma detectors (such as High-Purity Germanium detector HPGe that is able to detect gamma activity from low activity foils in a high and low background).

The HpGe detector is a semiconductor detector in which ionizing radiation is measured through the number of charge carriers set free in the detector semiconductor material. Ionizing radiation produces free electrons and holes. The number of electron-hole pairs is proportional to the energy of the radiation that is transferred to the semiconductor. As a result, a number of electrons are transferred from the valence band to the conduction band, and an equal number of holes are created in the valence band. The detector material is positioned between two electrodes where under the influence of the electric field, electrons and holes travel to the electrodes. They result in a pulse that can be measured in an outer circuit. The holes travel in the opposite direction and can also be measured. As the amount of energy required to create an electron-hole pair is known and independent of the energy of the incident radiation, measuring the number of electron-hole pairs allows the whole energy carried by the incident radiation to be determined [Knoll 2010]. This requires that the detection is performed in a single-counting regime. There, the particles land one by one on the detector and their incident energy can be measured. Otherwise, if several particles concur to produce the $e^-/hole$ pairs, the spectrum of the source cannot be retrieved.

The rate R of activation due to the neutron interaction is given by:

$$R = \varphi \Sigma_{act} V \, . \tag{2.14}$$

Where φ is the neutron flux averaged over the foil surface, Σ_{act} is the activation cross section averaged over the neutron spectrum and V is the volume [Knoll 2010].

The total number of radioactive nuclei $N(t)$ at a certain time t changes with a rate given by the difference between the formation rate of the radioactive nuclei and the decay rate:

$$\frac{dN(t)}{dt} = R - \lambda N(t) \, . \tag{2.15}$$

Where λ is the decay constant and $A(t) = \lambda N(t)$ represents the *total activity* and is the decay rate (decays per unit time of a radioactive sample). The

number of radioactive nuclei as function of time can be written as:

$$N(t) = \frac{R}{\lambda}\left(1 - e^{-\lambda t}\right). \tag{2.16}$$

The *total activity* of the foil is therefore given by:

$$A(t) = R\left(1 - e^{-\lambda t}\right). \tag{2.17}$$

The induced activity builds up during the time of exposition of the sample to the neutron pulse. For an ideal infinitely long time of irradiation, the induced activity tends to the asymptotic or saturated activity.

$$A_\infty = R = \varphi \Sigma_{act} V. \tag{2.18}$$

Assuming that t_o is the time when the irradiation is stopped, the activation at t_o is:

$$A_o = A_\infty\left(1 - e^{-\lambda t_0}\right). \tag{2.19}$$

After the exposure, the sample activity is counted in a radiation counter (e.g., HPGe). The decay process is continuous therefore the various times corresponding to the different stages of the measurement (end of the irradiation t_0, start of counting process t_1, end of counting process t_2) must be carefully noted. The number of counts C (see Figure 2.36) can be defined as:

$$\begin{aligned} C &= \epsilon \int_{t_1}^{t_2} A_0\, e^{-\lambda(t-t_0)} dt + B, \\ C &= \epsilon \frac{A_0}{\lambda} e^{\lambda t_0}\left(e^{-\lambda t_1} - e^{-\lambda t_2}\right) + B. \end{aligned} \tag{2.20}$$

Where ϵ is the overall counting efficiency (including any self-absorption effect) and B is the number of background counts expected in the interval (t_2 - t_1).

Therefore the neutron flux magnitude can be calculated from:

$$\begin{aligned} A_\infty = \varphi \Sigma_{act} V &= \frac{\lambda(C-B)}{\epsilon(1 - e^{-\lambda t_0}) e^{\lambda t_0}(e^{-\lambda t_1} - e^{-\lambda t_2})}, \\ \varphi &= \frac{1}{\Sigma_{act} V} \frac{\lambda(C-B)}{\epsilon(1 - e^{-\lambda t_0}) e^{\lambda t_0}(e^{-\lambda t_1} - e^{-\lambda t_2})}. \end{aligned} \tag{2.21}$$

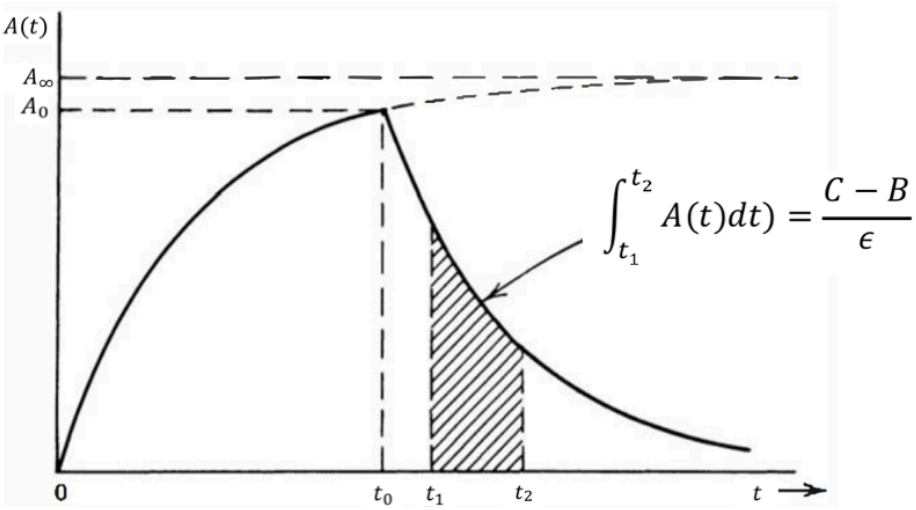

Figure 2.36 *Curve of the activity of an irradiated sample*

In order to determine the neutron flux that has activated the sample, one must know the time of irradiation, the start and the end time of counting, the cross section and the volume of the sample.

As shown in section 1.1 (c), there are several possible absorption reactions, such as (n,p), (n,α), (n,γ), (n,f), etc., that can generate radioactive nuclei, many of which are gamma emitters. The cross-section of each of these reactions is energy dependent. Hence, the total activity of a particular type of decay can only give a measurement of the neutron fluence in a particular energy range (where the cross-section is significant). If the neutron energies spread over a wide range, no single detector can cover that entire domain. The spectrum needs then to be measured with a set of activation foils, resulting in a multi-detector system.

Radiative capture or (n,γ) reactions typically have largest cross sections at or near neutron thermal energies, and therefore materials in which these reactions predominate are preferentially chosen for slow neutron detectors. Other reactions such as (n,p), (n,α) and (n,2n) often require a threshold energy. Materials in which these reactions predominate can therefore be candidates as fast neutron detectors, which will be inherently insensitive to slow neutrons

In a laser-plasma interaction environment, the choice of material for the activation detectors must take into account the high gamma and X-ray background radiation, the achievable activity level, and that the half-life time is not too short to allow for the counting.

For this reason, some activation materials that are normally used in other types of experiment (e.g. traditional accelerators), were excluded from our experiment. Both reactions in ^{58}Ni were excluded due to the very low activity, which stems not from the number of activations, but from the very long half-life of

the products. The ^{63}Cu isotope was excluded, not due to the low activity, but to the fact that the copious X-rays produced in the laser interaction may create activity in the sample via the ^{63}Cu(γ,n)^{62}Cu reaction, which is indistinguishable from the neutron-generated activity.

The materials that were chosen for the experiment were ^{27}Al, ^{56}Fe and ^{115}In, which were used in their natural abundances.

Also the activation of the LiF catcher can also be exploited to obtain information about the neutrons produced. Indeed, a direct measurement of the total neutron production can be performed through the measurement of the residual isotopes from the irradiation. As shown in section 2.1.3, neutrons can be generated in a LiF catcher principally through three nuclear reactions:

$$^{7}Li + p \longrightarrow {}^{7}Be + n\,, \tag{2.22}$$

$$^{6}Li + p \longrightarrow {}^{6}Be + n\,, \tag{2.23}$$

$$^{19}F + p \longrightarrow {}^{19}Ne + n\,. \tag{2.24}$$

Only the ^{7}Be residual has a sufficiently long half-life, i.e. 53.22 day, to be detected without rush, while the half-lives of both ^{6}Be and ^{19}Ne are below 20 seconds, preventing a useful measurement in most of the cases.

$$^{7}_{4}Be + e^{-} \xrightarrow{53.22\ d} {}^{7}_{3}Li + \nu_e\,, \tag{2.25}$$

$$^{6}_{4}Be \xrightarrow{5\ zs} {}^{4}_{2}He + 2p\,, \tag{2.24}$$

$$^{19}_{10}Ne \xrightarrow{17.296\ s} {}^{19}_{9}F + e^{+} + \overline{\nu_e}\,. \tag{2.25}$$

The instable isotope ^{7}Be decays through electron capture ϵ either directly to the ground state of ^{7}Li (89.56%) or via the 477 keV of ^{7}Li (10.44%). In the second case the de-excitation process of the ^{7}Li emits a gamma ray of 477 keV that can be detected using an HpGe detector.

Chapter 3

Experimental results and conclusions

Abstract In this third chapter I describe the two experimental campaigns we carried out at two different laser facilities. Both experiments were designed to test the production of neutrons and the possible modifications of the energy spectrum of the latter. The difference between the two laser environments, and the two set-ups used give us the possibility to test under different conditions the feasibility of the experimental concept presented in the previous chapter. I show the principal results we obtained as well as some limitations that can be overcome in future experiments.

3.1 First Experimental Campaign (ELFIE)

The first experimental campaign has been carried out in May 2013 at the ELFIE Laser Facility (LULI, *Ecole Polytechnique, France*). The first aim of the campaign was to test the possibility of generate a neutron source that we were able to characterize with the diagnostics used. Using the laser trigger micro-lens (see § 2.1.2) protons with a range of energies have been collimated, allowing to test the capability to modify the neutron spectrum with an easy modification of the set-up.

The facility has a Ti:Sapphire laser source which is then injected in a glass amplifiers system. The laser system is based on the CPA (*Chirped Pulse Amplification*) technique that makes available to the users two ultra-intense laser beams (10 J – 350 fs) with a repetition rate of around 20 minutes. The pulse is generated in the oscillator at λ=1057 nm and amplified in an amplifier chain composed by several steps. In each step the diameter of the beam is increased.

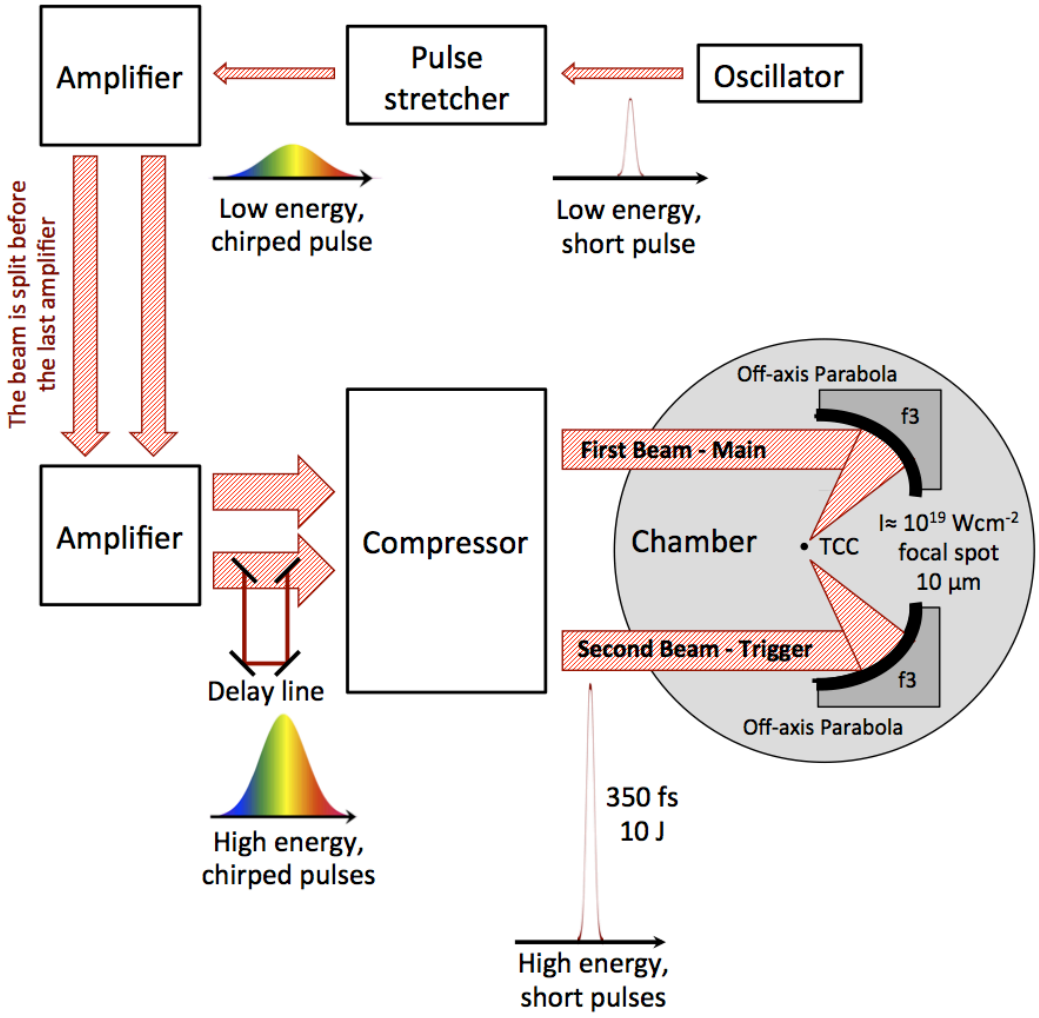

Figure 3.1 *Schematic diagram of the CPA system at the ELFIE Laser Facility. The short, low-energy pulse is generated in the oscillator. It is stretched to a longer duration before entering in the amplifier chain and it is recompressed to a short duration before the chamber.*

Before the last amplifier the beam is separated in two beams with a beam splitter. A user-adjustable optical path creates a delay line that allows the experimenters to choose the delay between the two beams. Therefore the arrival in the chamber of the second beam can be retarded with respect to the first beam up to several tens of picoseconds with a precision of a fraction of the pulse duration.

During our experiment we use the first beam, named below **main beam**, to accelerate the proton from the primary target and the second beam to activate the micro lens hence it is named in the following **trigger beam**. The ELFIE laser system described above is illustrated in Figure 3.1.

The two beams have a diameter of 105 mm at the entrance of the experimental chamber and were focused by two f-3 off-axis parabolic mirrors to a FWHM (*Full Width Half Maximum*) focal spot size of 10 µm achieving a laser

intensity on the target of $I \approx 3.6\times10^{19}\ W cm^{-2}$.

We focused the main beam on the primary target (located at TCC, Target Chamber Center) from which we accelerated protons via TNSA, while we focused the trigger beam on the external wall of the cylinder slightly moved with respect to TCC. The delay between the two beams has been verified using a streak camera with a precision of 10 ps and then using an interference technique. That is the two beams are brought simultaneously on a CCD in order to synchronize them, with a precision of a fraction of the pulse duration. This allows us to set the t=0, from which the trigger beam can be precisely delayed compared to the main beam. The beams arrived inside the chamber with a horizontal polarization. The main beam hits the primary target surface perpendicular to it while the trigger beam arrives on the cylinder wall with a slight angle (around 10°).

The pre-pulse in the facility was measured using a third order autocorrelation system (Amplitude Sequoia). The third order autocorrelation measure was taken a 10 Hz just after the regenerative amplifier, that is the first amplifier of the ELFIE amplification chain and the one where the signal is more strongly amplified from pJ up to mJ. Therefore it is the amplifier where the maximum non-linear effects take place and the pre-pulse is generated. As shown in Figure 3.2 at the time of our experiment, 60 ps before the main pulse there was a pre-pulse with an intensity three orders of magnitude lower than the main pulse. This pre-pulse was produced from a spurious reflection on an optic inside the amplifiers, the origin of which took several years to be identified.

As I described in the previous chapter (§ 2.1) the aim of our experimental campaigns was to test a new possibility to generate a neutron source using a high intensity laser pulse. First we generated a proton beam using the TNSA mechanism and we used them to generate neutrons in a *pitcher-catcher* configuration.

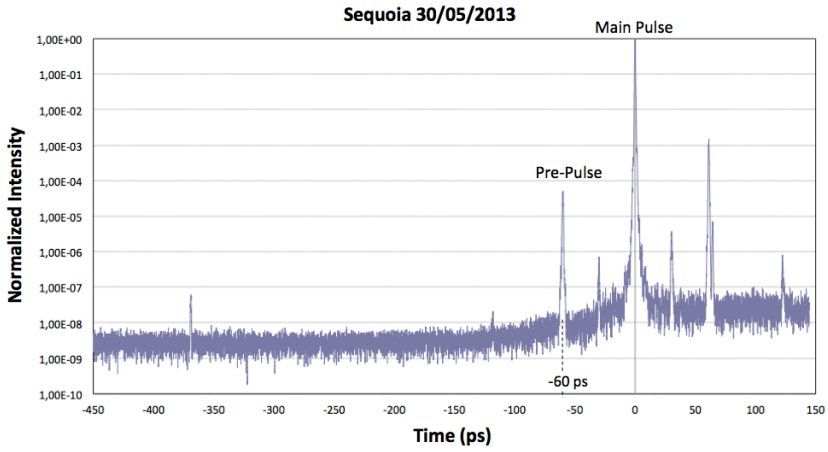

Figure 3.2 *Example of pulse duration measure taken during the experiment with the Amplitude Sequoia third order correlation.*

Second we used a laser-trigger micro-lens to collimate over a long distance a part of the proton spectrum. Third we used this collimated proton beam to generate a neutron source and we compared this second source to the one obtained during the first step. For each step of the experiment we varied the set-up. In the following sections, each set-up is presented in detail together with the results we obtained.

3.1.1 SET-UP A: Proton acceleration via TNSA and full spectrum neutron generation

Primary Target:	PET (50 μm thickness coated with 14 nm Al)
Cylinder:	-
Secondary Target:	LiF (25 mm diameter and 200 μm thickness)
Beams:	Only Main Beam
Diagnostics:	RCF stack for proton detection CR-39, nToF, Bubbles Detector Spectrometers for neutron detection

During this phase of the experiment we were interested in studying the characteristic of the accelerated protons and to use them to produce a full spectrum neutron beam. In the implemented set-up the main laser beam was focused by the f/3 off-axis parabola (OAP) on the primary target generating a forward proton beam. First of all we studied this beam putting an RCF stack on the forward direction and once the characteristics of the beam were determined we put the secondary target, the catcher, (i.e. the LiF) on the forward direction. Impinging on the catcher the proton beam generated the neutrons that were detected using a Bubble Detector Spectrometers (§ 2.2.2.3), a CR-39 stack (§ 2.2.2.2) and a neutron Time-of-Flight detector (§2.2.2.1).

Proton Beam

The proton beam has been studied using an RCF stack (see § 2.2.1.1) composed by 6 Gafchromic HD-810 RCF (with the sensitive layer in front of the beam trajectory) and 5 Gafchromic MD-55 RCF. Each layer of RCF was about 18 mm x 25 mm. The entire RCF stack was wrapped in a 12 μm thick aluminum foil to protect the RCFs from the gammas and the x-rays coming from the laser-target interaction zone. The stack was positioned 30 mm after the primary target on the forward direction in order to collect all the protons accelerated on this side (see Figure 3.3).

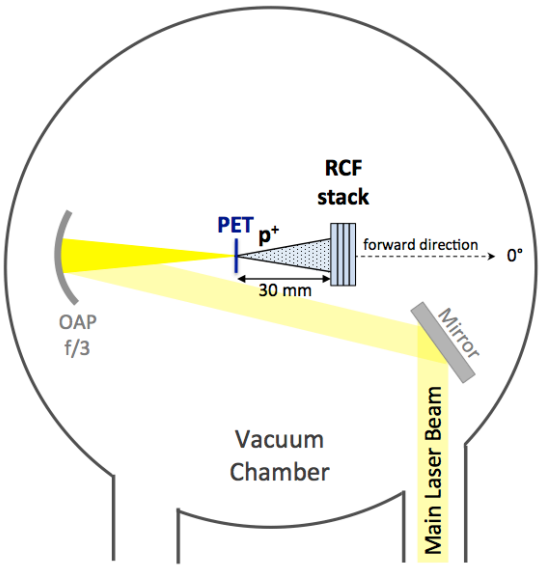

Figure 3.3 *Set-up of the first phase of the ELFIE experiment with the objective of studying the TNSA proton beam produced by the main beam using a RCF stack after the primary target.*

As said, the pre-pulse was only three order of magnitude lower than the main pulse, that is $10^{16}\ W cm^{-2}$. Therefore, it was high enough to ionize and ablate material from the target creating pre-plasma. Under these conditions we were forced to use thick target to prevent the pre-plasma formation on the rear side. [Fuchs *et al.*, 2007] and [Kaluza *et al.*, 2004] have shown how this can compromise the acceleration process.

In the beginning, a 25 μm thick Al target has been used to generate the proton beam. Under the same laser conditions, a metal target generates a higher flux and higher maximum cut-off energy of protons [Fuchs *et al.*, 2003], but at the same time it generated a very high x-ray signal due to the Bremsstrahlung. A high x-ray signal is a problem for neutron detection using nToF detectors as it generates an intense prompt signal (i.e. at t=0) that risks, if too high, to prevent detecting the later arriving neutrons.

The best compromise in order to have a good proton signal but a not too high X-ray and gamma ray signal was to use a plastic target. The material chosen was *polyethylene terephthalate*, commonly abbreviated PET, with a thickness of 50 μm.

The PET was aluminized on one side, that is covered with a 12 nm Al coating. The aluminum coting side has been put in front of the laser to maximize the laser absorption.

The proton spectrum for the 50 μm PET aluminized is shown in Figure 3.4. It was possible to observe signal up to the 7th layer of the RCF pack (6 HD + 1 MD) corresponding of a maximum energy of around 9 MeV.

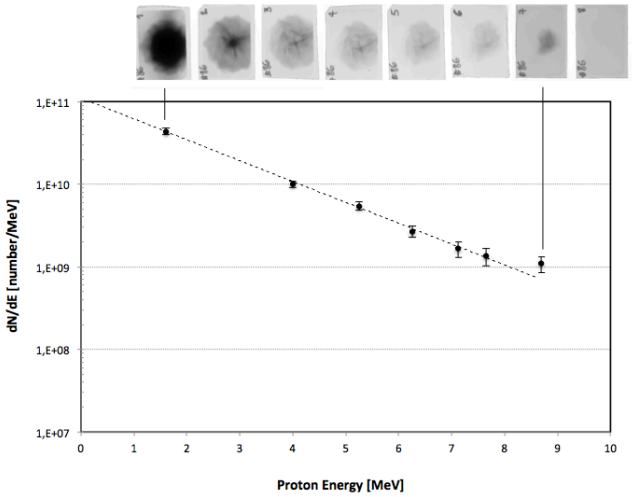

Figure 3.4 *Example of proton spectrum obtained during the ELFIE experiment.*

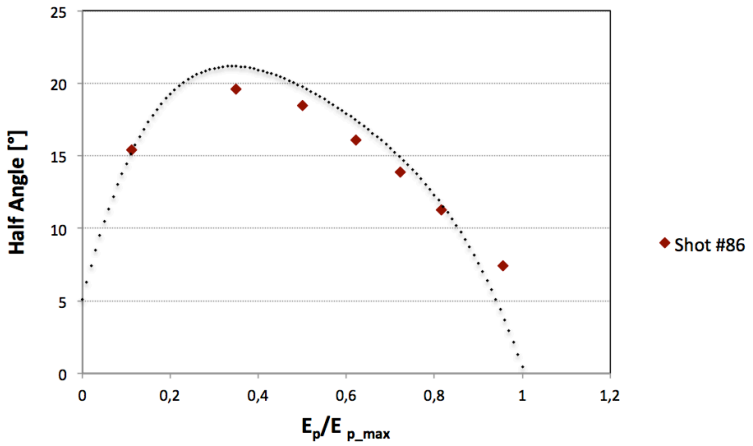

Figure 3.5 *Example of the divergence of the proton beam accelerated in a shot. The experimental measurement of the divergence half angle as function of the proton energy E_p normalized by the maximum proton energy E_{p_max} shows a good agreement with the fit proposed in [Mancic et al., 2010] and [Mancic Thesis 2010]. The fit is shown in figure with the dot line as the function:* $Half\ Angle\ (E) = p_0 + p_1 E + p_2 E^2 + p_3 E^3 + p_4 E^4$, *where coefficients are* $p_0 = 5.0778$, $p_1 = 121.61$, $p_2 = -321.33$, $p_3 = 344.33$ *and* $p_4 = -150.46$.

Such low energy is due to the fact that we had to resort to thick target due, as already said, to the strong laser pre-pulse ([Fuchs *et al.*, 2007], [Kaluza *et al.*, 2004]).

As shown in § 2.2.1.1, the RCFs are radiation-dose sensitive films that must be digitized before being analyzed. In our case the scan has been done using an Epson photo scanner (*perfection 2450 photo - model G860A*) used in transparency mode. The calibration curve must be known for the specific scanner used. The calibration curve allows to convert the optical density (OD) of each layer in the equivalent absorbed dose. Once the dose absorbed by each film has been determined, a program has been used to find the best fit of the proton spectrum.

The program has been developed during the past years by our group [Antici thesis 2007] and it allows, through an iterative routine, to infer the proton spectrum that best fits the experimental data.

The calibration of the RCF has been done in our group using RCF that we exposed to a known dose in a traditional accelerator facility and it has been successfully compared to nuclear activation measurements performed by our colleagues of CENBG on other collaborative experiments.

The proton spectrum produced via TNSA can be considered reproducible from shot to shot with a variation of ~20% due to fluctuations in the laser energy, the pulse duration or the pre-pulse presence [Antici thesis 2007].

An average between the spectra obtained in six different shots is shown in Figure 3.4. In the top part of the figure a typical RCF stack is presented. As discussed, in § 2.1.1, where the principal characteristics of a TNSA proton beam were pointed out, a different proton divergence can be evidenced in each layer of the stack. In Figure 3.5 is represented the trend of the maximum half angle as a function of the normalized energy of the protons for an example shot of our campaign. The dotted line is the fit presented in [Mancic *et al.,* 2010] and [Mancic thesis 2010] based on previous experimental measurements. The half angle varies from a minimum of 6° (for the maximum cut-off proton energy) to a maximum of 20° for 4 MeV protons.

Neutron Beam

Once that the proton spectrum obtainable in the ELFIE experimental condition has been tested, we investigated the possibility to generate a neutron source. Therefore we put a second target, the catcher, of lithium fluoride (LiF) 2 mm after the primary target. The LiF target was a disk of 25 mm in diameter and 200 μm in thickness in which the entire TNSA proton beam was collected.

In order to detect the neutrons generated, we put a CR-39 stack 25 mm after the LiF target in the 0° (forward) direction. The CR-39 stack was composed of 5 CR-39 layers of 1 mm thickness (around 25 mm x 18 mm), wrapped in a 12 μm thick aluminum foil and put in a lead shield box of 1 mm thickness. This lead box shielded the CR-39 from direct protons with energy below 21 MeV, as explained in § 2.2.2.2. This ensured that the CR-39 detected only neutrons since it is sensitive to all ionizing particles. Since the neutron flux in our experimental conditions was too low to obtain good counting statistics of the neutrons in the CR-39, we integrated the neutron signal over three to four shots in the same CR-39 stack in order to increase statistics. As described in § 2.2.2.2 the CR-39 must be chemically etched for individual tracks to be visible under the microscope. Taking into account the response curve of CR-39, the number of incident neutrons can be determined from the number of tracks.

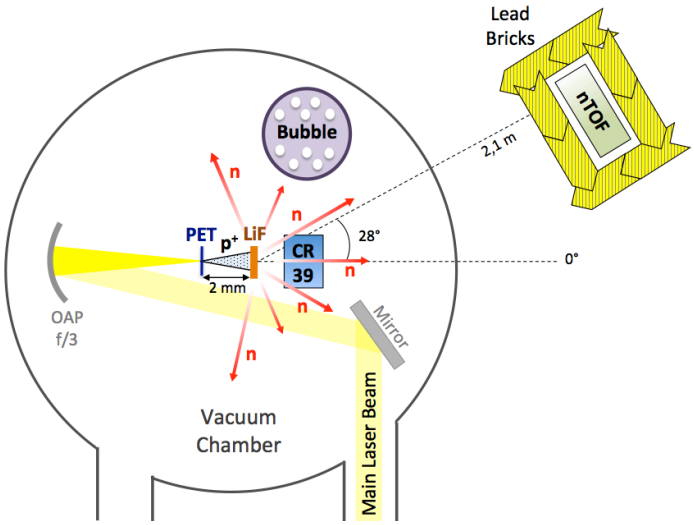

Figure 3.6 *Set-up inside and outside the chamber to determine the full neutron spectrum that we generated in the experiment. The catcher-target LiF was 2 mm away from the pitcher-target PET in the forward direction. So all the forward proton beam accelerated from the PET collided with the LiF.*

To count the tracks in the CR-39 after etching, the CR-39 were viewed in a microscope with a zoom that covered 0.57 mm^2 and 25 pictures were taken for a total area of 14.52 mm^2. An un-irradiated sample of CR-39 was also etched and counted as reference. In order to deduce the number of neutrons from the number of pits present on the etched CR-39 surface, we used an efficiency curve (see Figure 3.7) obtained by Frenje with the method described[1] in [Frenje *et al.*, 2002], where only the CR-39 efficiencies for detecting DD neutrons (2.45 MeV) and DT neutrons (14.1 MeV) are presented.

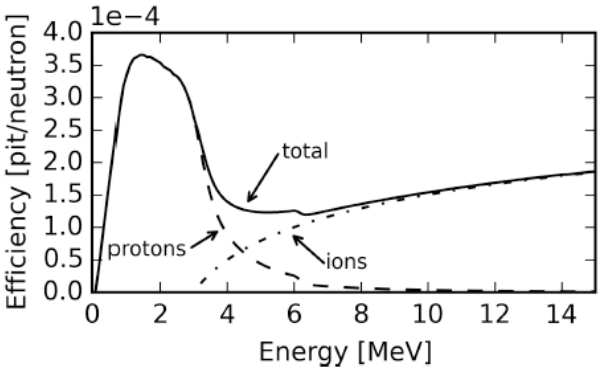

Figure 3.7 *The efficiency of the pit formation in CR-39 as function of the energy of an incident neutron inducing the recoil of a nucleon, either proton or heavier ion, as indicated. The curve has been calculated for an etching of the CR-39 in 6.0 molarity NaOH at 80°C from 6 hours. These numbers correspond to the rear-side of the plastic as defined by [Frenje* et al.*, 2002].*

[1] A Monte-Carlo code was developed to predict the CR-39 efficiency for standard etch

In practice, the way the neutron yield, which we quote later on, is inferred from the CR-39 is based on using the neutron spectra and angular distributions given by the simulations (based on the measured spectra and angular distributions of the protons impinging on the LiF). Then, using the curve shown in Figure 3.7, we can deduce the number of tracks that would be created, and compare that number to the observed density of tracks. This allows us to have an independent way, compared to the bubble detectors and the nTOF, of verifying the consistency of the simulations.

The bubble detectors were put inside the chamber in an independent airtight vessel. This allowed us to reduce the distance from the target to the detectors as much as possible, leaving the bubble detectors at atmospheric pressure. Also for this diagnostic the neutron flux achievable in one shot was too low to have a good bubble counting statistics; so several shots were integrated before getting the vessel out from the chamber and counting the bubbles present in each detector. The information about the neutron spectrum was obtained thanks to the procedure described in § 2.2.2.3.

Obviously the necessary integration over several shots makes these diagnostics (CR-39 and bubble detectors) more a qualitative indicator of the neutron generation. Nevertheless, it gives a good estimation of the order of magnitude of the number of neutrons produced. Under our experimental conditions the CR-39 recorded a yield of $7 \pm 4 \times 10^5\ n/MeV/sr/shot$ and the bubble detectors detected $8 \pm 4 \times 10^5\ n/MeV/sr/shot$.

Three nTOF detectors were also used to obtain information about the energy spectrum of the generated neutrons. The nToF detectors were set up at a variety of angles and distances outside the chamber and shielded with lead bricks making a box around the scintillator and the PM tube (as shown in Figure 3.6). We used a $40\times40\times120\ mm\ BC400$ scintillator coupled to a Photonis $XP2972$ photomultiplier and we recorded the signal with a $1\ GHz$ oscilloscope. The scintillator was placed so that neutrons passed through its $40\ mm$ length. The thickness of the lead shielding was $200\ mm$ and it was used to reduce the signal produced in the scintillator by x-rays and γ-rays originating from the target or the interaction chamber.

We analyzed the neutron energy spectrum obtained from the nTOF placed at $2.1\ m$ from the LiF position and at an angle of 28° from the 0° forward direction, as shown in Figure 3.6. I will discuss the results obtained later on in § 3.1.3 together with the comparison with the neutron signal generated using the proton beams modified by the laser-triggered micro lens that is presented below.

3.1.2 SET-UP B: Focusing study

Primary Target:	PET (50 μm thickness coated with 14 nm Al)
Cylinder:	Al (3 mm length; 940 μm external diameter; 780 μm internal diameter)
Secondary Target:	-
Beams:	Main and Trigger Beam
Diagnostics:	RCF stack for proton detection nToF for gamma and background detection

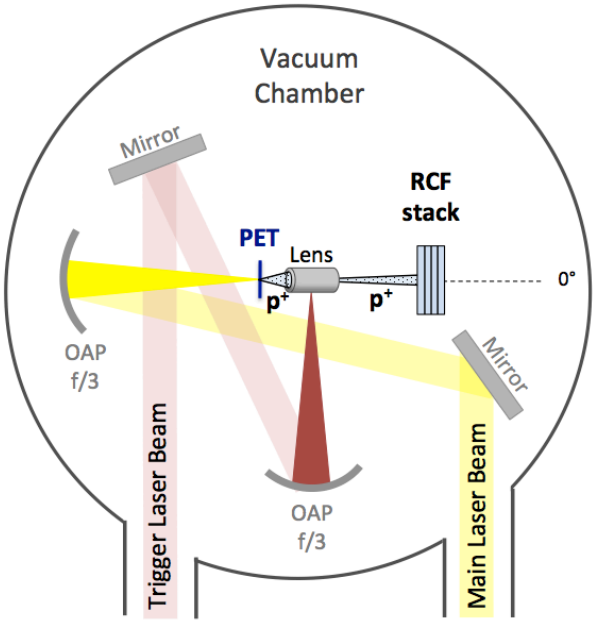

Figure 3.8 *Set-up of the second phase of the ELFIE experiment. A hollow aluminum cylinder was put 1 mm away from the PET primary target and an RCF stack was positioned about 30 mm away from the primary target.*

After characterizing the proton beam accelerated from the primary target and the neutron beam generated by the collision of the proton beam in the LiF, in the second phase of the experiment we studied the proton focusing achievable using the micro-lens described in § 2.1.2 and how to exploit this mechanism to modify the energy spectrum of the accelerated proton beam.

During this phase of the experiment, the set up inside the vacuum chamber was changed by removing the LiF catcher and placing the hollow aluminum cylinder after the primary target, as illustrated in Figure 3.8. We used both laser beams: the *main laser beam* was focused on the primary target, the PET, and the

trigger laser beam was focused on the external wall of the cylinder and we put a RCF stack on the forward direction to detect the proton beam after the cylinder.

The cylinder was 3 mm long with an internal diameter of 780 µm and an external diameter of 940 µm. Obviously the alignment of the cylinder must be precise. The axis of the cylinder must be parallel to the 0° forward direction and the internal aperture must be centered with the focal spot on the primary target.

We checked the aligment by shooting on the primary target without shooting on the cylinder, so that the micro lens is not activated. The entrance of the cylinder was put 3 mm away from the primary target while a HD RCF film was put 400 mm away from the target (see Figure 3.9).

Only the projection of the proton beam passed through the inactive cylinder is visible on the RCF after the cylinder. It is thus possible to deduce the precision of the cylinder's alignment. We obtained a precision better than 1°.

Once that the alignment was fine, the second laser beam, the trigger pulse, was focused on the external wall of the cylinder, at half of his length. The trigger beam was set to arrive 86 ps after the main beam, with a precision of the order of few ps.

As explained in § 2.1.2, the *timing* between the two beams (the main and the trigger) and the *distance* between the primary target and the cylinder are important parameters that set the lens activation and determine the energy of focused protons.

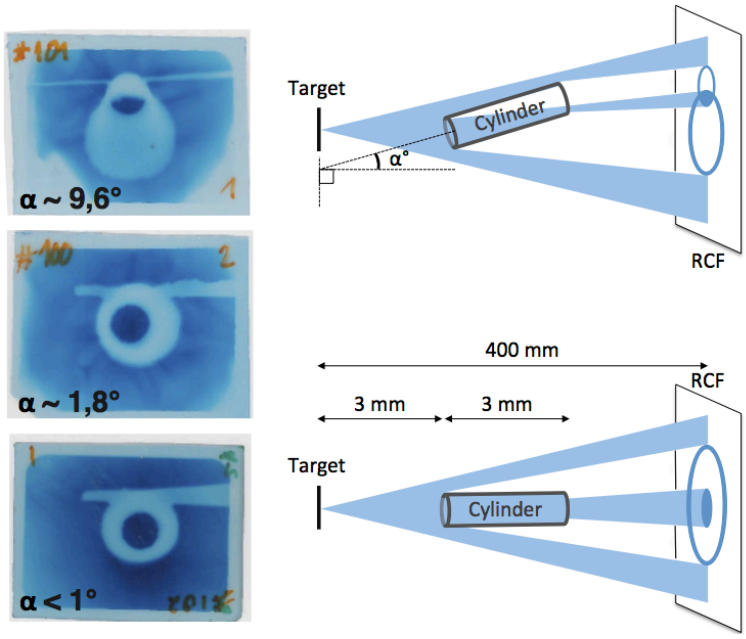

Figure 3.9 *On the left are shown protons beams recorded in three RCFs from three different alignment test shots. On the right diagrams of a misalignment situation and the alignment one. The small circle is the projection of the external circumference at the ending of the cylinder, while the big circle is the projection of the internal circumference at the beginning of the cylinder. Measuring the distance between the two centres, it is possible to obtain information about the angle orientation of the cylinder.*

In order to study the focusing effect of the lens, we chose to set the distance between the primary target and the entrance of the cylinder at 1 mm. This allowed us to obtain a spread in energy of the proton beam entering the cylinder and to collect at the same time the whole beam inside the cylinder. At a distance of 1 mm from the target, the internal aperture angle of the cylinder is 42°. As we already saw, the maximum divergence of the proton beam corresponds to a half angle of 20°. This means that 40° is the minimum aperture needed to collect the entire beam.

Positioning the lens at a larger distance from the target would help to focus a smaller range of energies. On the other hand, the aperture angle would become smaller, not allowing to collect the whole incident proton beam.

A compromise must be sought depending on the facilities and the application of the focused beam. In our case, we would like to study the effects of the focalization on the spread beam without losing too many particles. Indeed, for the application of our experiment, we were interested in collecting the whole proton beam to maximize the number of particles after the lens, in order not to decrease the achievable neutron flux too much.

Figure 3.10 shows the spread of the proton beam over time. Each proton energy is at a different position inside the cylinder at the arrival of the trigger pulse arriving 86 ps after the main laser beam accelerated the proton beam from the primary target. The minimum energy of 1 MeV represented on this plot is not the minimum energy of the accelerated protons, but the minimum energy we were able to detect with our RCF stack.

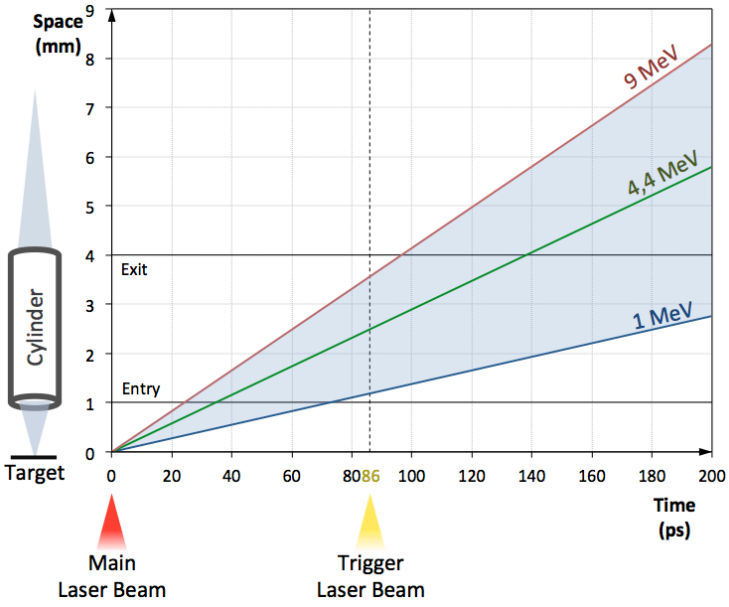

Figure 3.10 *Space vs. time graph of protons flying from the main source to and through the cylinder. The light blue cone represents the debunching over time and space of the proton beam.*

In § 2.1.2, I described the operating principle of the micro-lens and I pointed out the principle parameters that can control the focusing process. During the set-up of the ELFIE experimental campaign, we established these parameters to be:

- **Distance proton source to beginning of the cylinder:** 1 mm.
- **Timing between the two beams:** 86 ps delay for the trigger beam.
- **Intensity of the trigger beam**: $I \approx 3.6\times10^{19}\ Wcm^{-2}$ (same as the main beam).

While the distance and the timing determine the position of each proton energy when the transient electric field inside the cylinder is triggered, the intensity of the trigger beam determines the duration of this field and its intensity. Before presenting the results achieved during this phase of the experiment, is estimate the duration and the intensity of the transient electric field in our experimental conditions.

Estimate of the duration of the transient electric field

The transient electric field inside the cylinder depends on the evolution of the plasma inside it. The duration of the field is indeed a function of the plasma expansion velocity. There is not yet a recognized model of the cylindrical plasma expansion that has been validated via experimental results, but as discussed in § 2.1.2, in our experimental conditions, the plasma expansion can be described as a TNSA mechanism.

It is possible to identify three temporal stages:

1. The time duration of the heating process of the electrons at the laser focal spot position on the external wall of the cylinder that is of the order of the laser-plasma interaction: $\tau_{laser} \approx 0.35\ ps$.
2. The time it takes for the hot electrons to spread over the inner surface of the cylinder. If we consider hot electrons moving at the speed of light and the maximum dimension of the cylinder (≈3 mm): $\tau_{spread} \approx 10\ ps$.
3. The time τ_E over which the plasma expands inside the cylinder and the transient electric field is operating.

To estimate the order of magnitude of the duration of the electric field inside the cylinder, one can use the isothermal plasma expansion model [Mora 2003] and the adiabatic plasma expansion model [Mora 2005] that have been developed for a planar infinite foil and for a thin foil of initial width L respectively.

In order to estimate τ_E, it is useful to first estimate some parameters of the plasma expansion. As previously said, the hot electrons are generated via several absorption mechanisms and different formulas have been proposed for the hot electron temperature as a function of the laser intensity and wavelength. Taking

for example the Beg's formula [Beg *et al.*, 1997] the hot electron temperature at time zero (when the laser pulse interacts with the target) is given by:

$$k_B T_{e0} = 215 \left[\left(\frac{I_0}{10^{18} W cm^{-2}} \right) \left(\frac{\lambda_0}{\mu m} \right)^2 \right]^{1/3}. \quad (3.1)$$

In our experimental conditions, $\boldsymbol{I_0 \approx 3.6 \times 10^{19}\ W cm^{-2}}$ and $\lambda_0 = 1.057\ \mu m$ so that the hot electron temperature can be estimated as $\boldsymbol{k_B T_{e0} \approx 740\ keV}$.

The total number N_{e0} of hot electrons generated can be estimated taking into account the absorbed laser energy and the hot electron temperature obtained from equation (3.1) [Fuchs *et al.*, 2006]:

$$N_{e0} = \frac{f E_{laser}}{k_B T_{e0}} \quad (3.2)$$

where the laser energy is $\boldsymbol{E_{laser} = 10\ J}$ and f is the fraction of laser light that is absorbed into the pre-plasma as hot electrons. This fraction f has been found to depend on the laser incident intensity as follows:

$$f = 1.2 \times 10^{-15} I^{0.74} \quad (3.3)$$

where the intensity is given in $W cm^{-2}$ ([Fuchs *et al.*, 2006]). The scaling (3.4) for the conversion fraction fits very well with the measured data in [Key *et al.*, 1998] and [Feurer *et al.*, 1997] where the maximum conversion efficiency was found to be $f_{max} \approx 0.5$. In the ultra relativistic regime for a laser intensity above $10^{20}\ W cm^{-2}$ the data reached also 60% for near-normal laser incidence and 80%–90% for 45° incidence [Ping *et al.*, 2008]. Using the equation (3.3) the conversion efficiency during the ELFIE experiment was $\boldsymbol{f = 0.35}$. Therefore only 35% of the 10 J laser energy was converted in hot electrons for a total number $\boldsymbol{N_{e0} = 3 \times 10^{13}}$.

As discussed in the previous chapters, these hot electrons move inside the target and spread over the inner surface of the cylinder. To make an estimate of the hot electron density n_{e0}, I consider that the volume where these electrons spread corresponds to the product of the cylinder surface $2\pi RL$[2] and the Debye length.

$$n_{e0} = \frac{N_{e0}}{2\pi RL \cdot \lambda_D}. \quad (3.4)$$

The Debye length in the expanding plasma is defined as:

[2] With $R \approx 0.4\ mm$ the radius of the cylinder, and $L = 3\ mm$ the length of the cylinder.

$$\lambda_D = \sqrt{\frac{\varepsilon_0 k_B T_{e0}}{n_{e0} e^2}}. \tag{3.5}$$

Where ε_0 is the vacuum permittivity, k_B the Boltzmann constant and e the electron charge. Equations (3.4) and (3.5) can be combined to obtain the value of the two unknowns. Therefore the electron density is estimated to be $\boldsymbol{n_{e0} \approx 4\times10^{17}\ cm^{-3}}$ and the Debye length $\boldsymbol{\lambda_D \approx 10\ \mu m}$.

It is possible to define the ion-acoustic velocity c_s and the ion plasma frequency ω_{pi} as:

$$c_s = \sqrt{\frac{Z K_B T_e}{m_i}}, \tag{3.6}$$

$$\omega_{pi} = \sqrt{\frac{n_{e0} Z e^2}{m_i \varepsilon_0}}. \tag{3.7}$$

Where Z is the *ion charge number* and m_i the *ion mass*.

In the model of free isothermal expansion presented in [Mora 2003], the ion front velocity is obtained with the formula:

$$v_{front} \cong 2c_s \ln\left(\tau + \sqrt{\tau^2 + 1}\right). \tag{3.8}$$

The parameter τ is defined as:

$$\tau = \frac{\omega_{pi} t}{\sqrt{2e_N}}. \tag{3.9}$$

Where t is the *time* and e_N=exp(1), the *Napier's constant* . Therefore the ion front velocity defined in (3.8) diverges logarithmically with time for a free isothermal expansion. The isothermal model assumes a constant electron temperature, which is reasonable during the laser pulse τ_{laser}. However, it cannot be considered correct for late times, since the electrons progressively give their energy to the ions and cool down during the expansion. For this reason in [Mora 2005], an alternative model is presented that takes into account the electron cooling due to the energy transfer to the ions and the charge separation effects. According to this model there is a relevant characteristic expansion time of the foil, defined as:

$$\tau_{x_L} = \frac{x_L}{2c_s}. \tag{3.10}$$

With x_L being the thickness of the foil. For time $t \ll \tau_{x_L}$, the expansion is not significantly different from the isothermal semi-infinite case. For $t \approx \tau_x$, the cooling progressively occurs, and for $t \gg \tau_x$ the electron cooling is fully effective and the velocity becomes progressively frozen. The logarithmic trend of the ion front velocity of formula (3.8) will tend to a constant final velocity that is a function of the target thickness [Mora 2005]:

$$v_{final} \cong 2c_s \ln\left(0.32\frac{x_L}{\lambda_D} + 4.2\right). \tag{3.11}$$

In Figure 3.11, taken from [Mora 2005], the trend of v_{front} is shown in the case of isothermal and adiabatic expansions.

In our experimental conditions, we can assign the following values to the defined parameters: $\boldsymbol{c_s \approx 8.4\times10^{-3}\ mm/ps}$, $\boldsymbol{\omega_{pi} \approx 8.3\times10^{11}\ rad/s}$, $\boldsymbol{\tau_{x_L} \approx 5\ ps}$ and $\boldsymbol{v_{final} \approx 3.2\times10^{-2}\ mm/ps}$.

From the evolution of the ion front velocity with time (presented in Figure 3.11), we can estimate the time needed for the ion front to reach the center of the cylinder. The transient electric field must be of the same duration: $\boldsymbol{\tau_E \approx\ 14\ ps}$.

Considering the time needed for the hot electrons to spread along the cylinder and the time needed for the ion front to reach the center, we can suppose that the focusing effect of the lens switches off between 25 and 30 ps after the arrival of the trigger pulse on the cylinder, therefore around $110 - 120\ ps$.

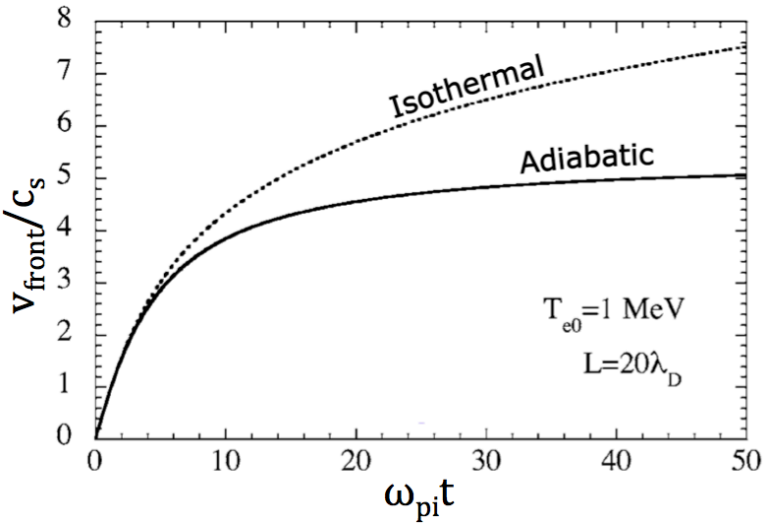

Figure 3.11 *Fastest ion velocity as function of time for the case presented in [Mora 2005] with $x_L = L = 20\lambda_D$ and $T_{e0} = 1\ MeV$. The dotted line is the prediction of the equation (3.8) for the free isothermal expansion.*

Estimate of the intensity of the transient electric field

In the two papers by Mora cited above, is also shown the variation of the electric field as a function of the expansion direction at a given time and for a fixed initial hot electron temperature. In both models, isothermal and adiabatic, the electric field presents a plateau region where the electric field is almost homogeneous, preceded by a peak at the ion front position. In both models, the electric field at the peak is given by:

$$E_{front} \cong \frac{\sqrt{2}k_B T_e}{e\lambda_D}. \tag{3.12}$$

For the isothermal model [Mora 2003], the electric field in the plateau $E_{plateau}$ is approximately half the peak electric field at the ion front. The evolution of the electric field at the ion front is described by:

$$E_{front} \cong \frac{2E_0}{\sqrt{2e_N + \omega_{pi}^2 t^2}}. \tag{3.13}$$

Where E_0 is related to the electron temperature (energy) divided by the Debye length and is given by:

$$E_0 = \sqrt{\frac{n_{e0}k_B T_{e0}}{\epsilon_0}}. \tag{3.14}$$

As said, in this isothermal case, the ratio $E_{front}/E_{plateau}$ is equal to 2 and it remains constant during the plasma expansion, therefore, according to (3.1.3), both the electric field values, E_{front} and $E_{plateau}$, evolve as t^{-1}.

On the other hand, in the adiabatic model presented in [Mora 2005], the ratio $E_{front}/E_{plateau}$ increases linearly with time. This means that the double layer (electrons and ions) staying at the ion front is the dominant feature of the electric field structure at late times.

In this case $E_{front} \propto t^{-2}$ and $E_{plateau} \propto t^{-3}$. Still, for late times, the proton deviation is mainly due to the electric field in the long plateau region and not to the field in the small ion front region.

An example of the electric field profile over the space in the isothermal and adiabatic case is shown in Figure 3.12, for $k_B T_{e0} = 1\,MeV$, $\omega_{pi}t = 50$ and the thickness of the target $x_L = 20\lambda_{D0}$.

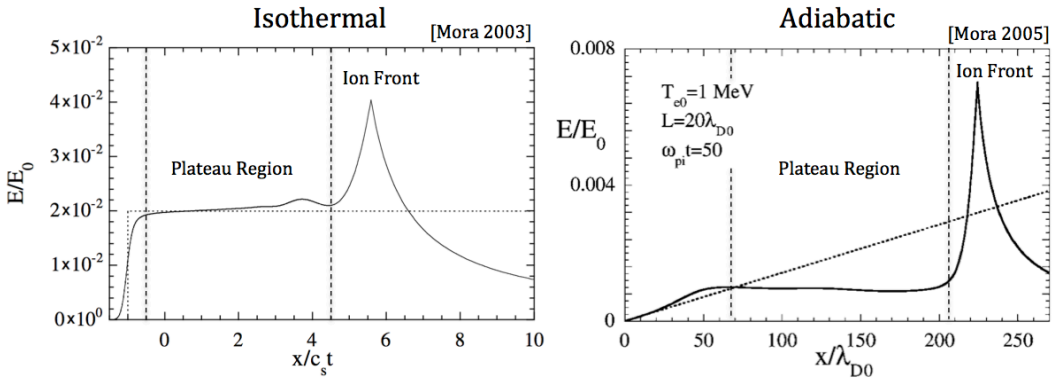

Figure 3.12 *On the left is presented the electric field at time* $\omega_{pi}t = 50$ *extracted from [Mora 2003] The dotted line corresponds to the self-similar solution. On the right the electric field in the adiabatic case extracted from [Mora 2005]. The dotted line is the electric field corresponding to the best-fitted Gaussian density calculated using the adiabatic model. In both graphs* E *is normalized to* $E_0 = \sqrt{n_{e0}k_B T_e/\epsilon_0}$.

Because the duration of the hot electron source is limited to the short laser pulse duration (≈0.35 ps), it is reasonable to assume that the temperature of the electrons varies during the long duration expansion according to an adiabatic regime where the total energy is given at the beginning of the expansion.

The calculation of the proton deviation inside the cylinder requires a full simulation of the electric field evolution in time and space and the precise geometry of the proton beam. A first attempt to simulate the electric field and the focusing process has been done by [d'Humières *et al.*, 2006].

Without going through the whole calculation process, we can still estimate the order of magnitude of the electric field inside the cylinder. For this we use the considerations about the field evolution detailed above and in [Mora 2005]. The proton deviation can then be deduced using:

$$\Delta v_\perp = \int \frac{q}{m_i} E_\perp\big(\vec{r}(t)\big)dt\,. \qquad (3.15)$$

Where $\vec{r}(t)$ is the proton position inside the cylinder.

As already mentioned, we will assume an adiabatic expansion starting with:

- An initial electron temperature $\boldsymbol{k_B T_{e0} \approx 740\ keV}$.
- An initial hot electron population $\boldsymbol{N_{e0} = 3{\times}10^{13}}$ distributed on the entire inner surface for a thickness of one Debye length ($\boldsymbol{10}$ μ$\boldsymbol{m}$).
- An initial density given by (3.4), $\boldsymbol{n_{e0} \approx 4{\times}10^{17}\ cm^{-3}}$.

With a cylinder thickness of $\boldsymbol{80}$ μ$\boldsymbol{m}$, the characteristic expansion time is equal to $\boldsymbol{\tau_{x_L} \approx 5\ ps}$ (equation 3.10).

For times larger than this typical time $t \gg \tau_{x_L}$, it is shown [Mora 2005] that

the electron temperature decreases as:

$$T_e(t) \propto T_{e0}\left(\frac{\tau_{x_L}}{t}\right)^2. \tag{3.16}$$

And the length of the plateau region can be defined as:

$$x_{plateau}(t) = v_{final}t\,. \tag{3.17}$$

Where v_{final} is the asymptotic ion front velocity $\boldsymbol{3.2{\times}10^{-2}\ mm/ps}$ (equation 3.11).

At the beginning for $t < \tau_{x_L}$, the plateau field is almost equal to the electric field in the plateau region of the isothermal case (that is $E_{front}/2$). For later times, the electric field in the plateau region can be approximated by:

$$E_{plateau}(t) \propto \frac{T_{e0}\left(\tau_{x_L}/t\right)^2}{x_{plateau}(t)} = \frac{T_{e0}\tau_{x_L}^2}{v_{final}}\ t^{-3}\,. \tag{3.18}$$

Which in our case leads to: $E_{plateau}(t)_{[V/m]} = 5.1{\times}10^{11}\ t_{[ps]}^{-3}$.

The evolution of the electric field in the plateau as function of time (in ps) is shown in Figure 3.13, from which it is possible to estimate the integral of the expression (3.15) as $\boldsymbol{\Delta v_\perp \approx 10^7\ m/s}$. The integral is calculated over approximately 15 ps, which is the duration of the electric field we estimated.

In Figure 3.14, the perpendicular components $v_\perp$ of three proton velocities (corresponding to three proton energies: 1 MeV, 4.4 MeV and 9 MeV) are shown as a function of their divergence angle from the source. Taking into account also the maximum half-angle divergence for each energies (see Figure 3.5) we can say that the maximum value of $v_\perp$ for each energies is:

$$v_{\perp max}(E = 1\ MeV) = 3.6{\times}10^6\ m/s,$$

$$v_{\perp max}(E = 4.4\ MeV) = 9.9{\times}10^6\ m/s,$$

$$v_{\perp max}(E = 9\ MeV) = 5.0{\times}10^6\ m/s.$$

Therefore, the value obtained above for $\boldsymbol{\Delta v_\perp}$ is compatible with a significant deviation of the trajectory for all the proton energies considered: the lens is very effective.

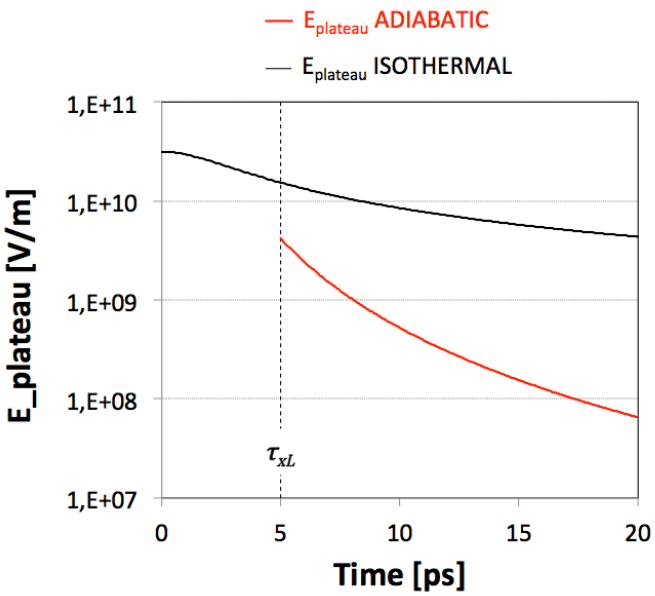

Figure 3.13 *Evolution of the plateau electric field in the case of isothermal expansion (black line) or adiabatic expansion (red line). The characteristic expansion time is represented by the dotted vertical line.*

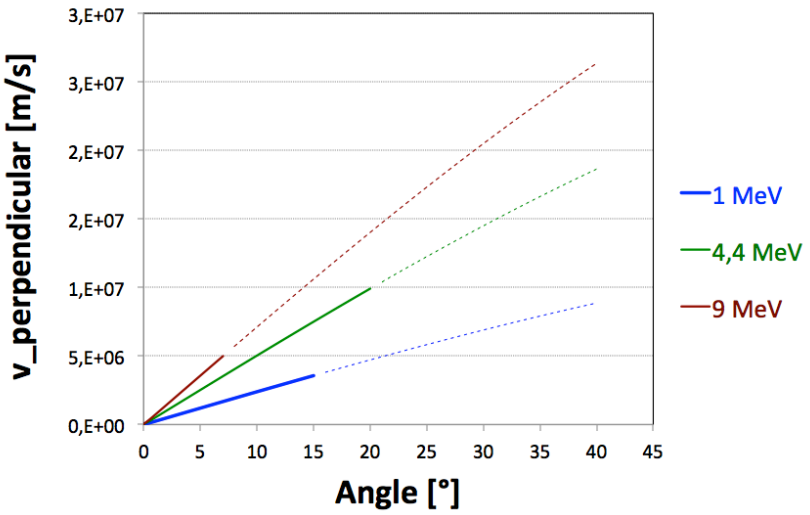

Figure 3.14 *Perpendicular component of the proton velocity as a function of the angle of emission, for 1 MeV, 4.4 MeV and 9 MeV. The line becomes dotted at the typical maximum half angle divergence for that energy (see Figure 3.5).*

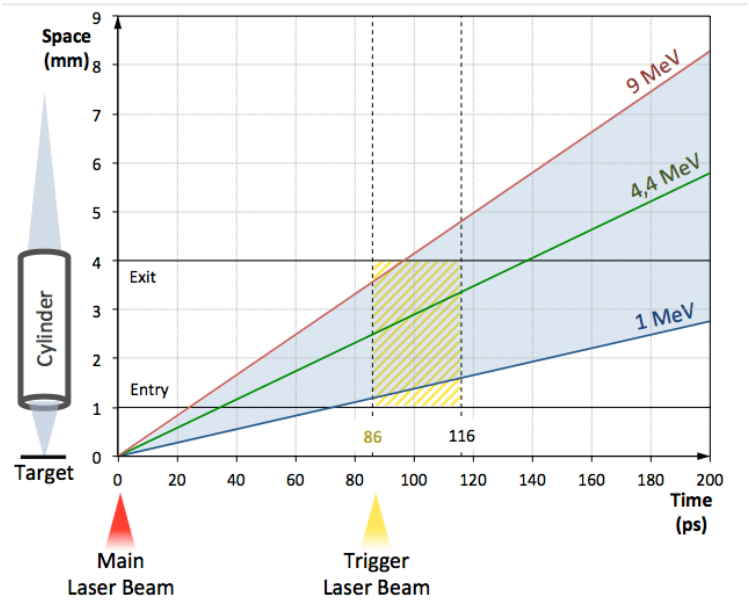

Figure 3.15 *Space vs. time graph for protons transiting through the cylinder. The period during which the transient electric field is acting inside the cylinder is shown in yellow.*

Consequently, from the above we can deduce that in our experimental conditions the entire beam underwent focalization, because the entire beam was inside the lens while the electric field was acting, as shown in Figure 3.15.

To detect the effects of the laser triggered micro lens on the proton beam we put an RCF stack with the same composition as in § 3.1.1 (6 HD + 5 MD) and at the same distance (30 mm) from the primary target.

Figure 3.16 shows the RCF stack obtained in this condition compared with the full proton spectrum of § 3.1.1 (Figure 3.5). The proton signal was visible in this case up to the 6th layer. The RCF stack clearly shows the focusing action of the lens and this is well shown in the plot of the divergence half angle versus the normalized energy. The divergence for the different energies is completely changed with respect to the case without the cylinder.

Playing with the brightness and the contrast, it is possible to identify signal also for the layer after the 6th RCF layer, as shown in Figure 3.17. This signal is not a proton signal but a shadow of the cylinder and its glass stick support. The shadow is generated by the X-rays created on the primary target that pass through the lens and its support. With different settings of brightness and contrast, the shadow is visible also in the first layer and it allows us to compare the simple projection made by the x-rays with the proton signal. We can see in this way that the proton beam was well-centered compared to the hollow inner part of the cylinder.

The RCF stack at a certain distance from the TCC gives information about the proton divergence in that position. To understand the evolution of the divergence in space, at least another position is needed.

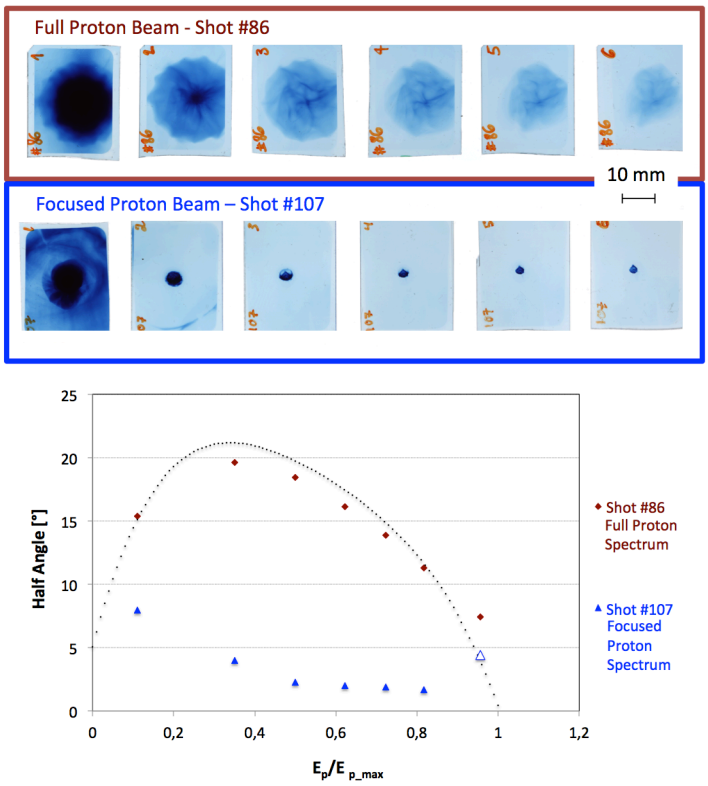

Figure 3.16 *(Top) two RCF stacks as measured in focused and unfocused conditions. (Below) the half angle divergence vs. the normalized proton energy for the full proton beam and for the focused one.*

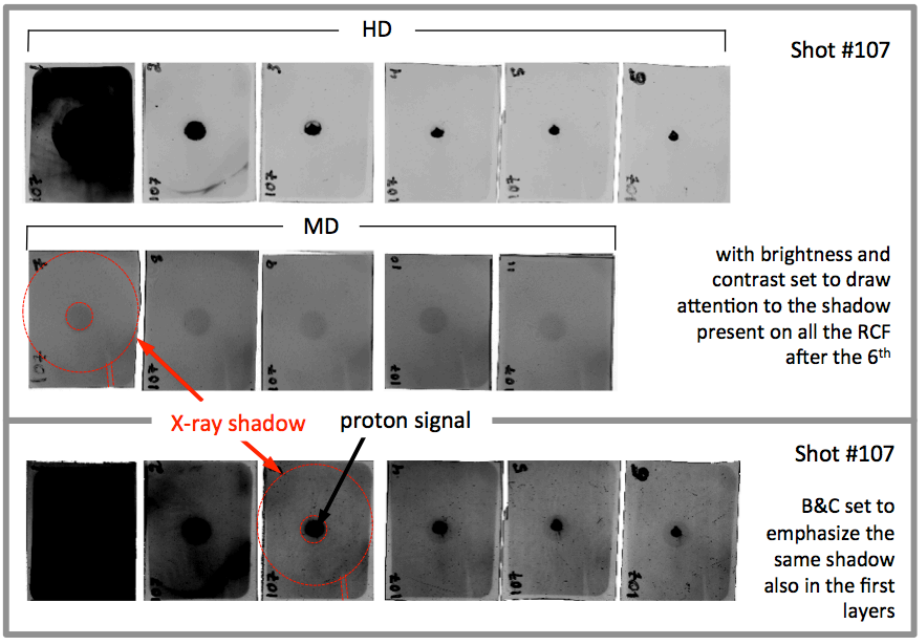

Figure 3.17 *Playing with brightness and contrast (B&C) on the RCF scan, it is possible to evidence the x-ray shadow of the cylinder in the focused proton shot.*

As said in § 2.1, as a TNSA proton beam has a good beam laminarity, this guarantees us that it is correct to infer information about the proton divergence knowing the divergence of the proton beam in two points.

For this reason we positioned a RCF stack at 555 mm from TCC to detect the divergence of the proton beam at this point. The lens parameters were the same. Due to the set-up inside the chamber, it was no possible to collect the entire proton beam on the RCF layers but only a quarter of it. Since the number of protons at this distance was low, we composed the stack only with MD films that are the more sensitive ones. Under this condition we recorded a proton signal up to the 3rd layer corresponding to a maximum proton energy of 9 MeV. The comparison of the proton signal on the RCF stack for the three different conditions is shown in Figure 3.18.

- **Shot #86**: The stack was 30 mm away from TCC and recorded the full proton spectrum accelerated from the PET primary target.
- **Shot #107:** The stack was 30 mm away from TCC and recorded the proton beam passed through the lens.
- **Shot #111:** The stack was 555 mm away from TCC and recorded the proton beam passed through the lens.

Without the information of the third shot it is not possible to infer if the proton beam has underwent real focalization or if it was only partially collimated.

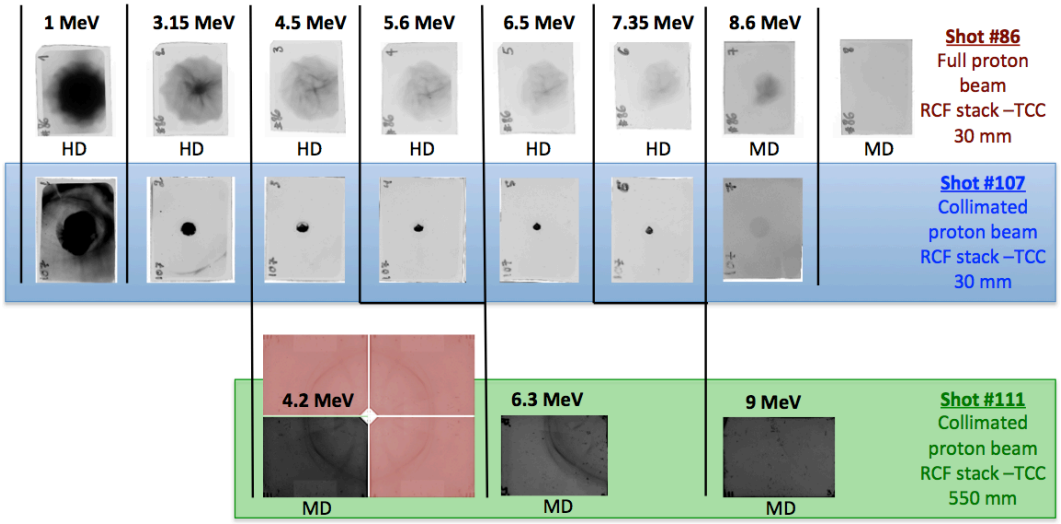

Figure 3.18 *The three RCF stacks compared. In the third row for the shot #111 is shown in red a reconstruction of how should appear the entire proton beam.*

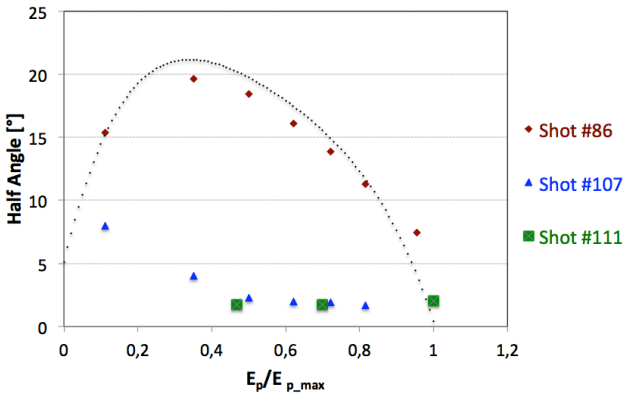

Figure 3.19 *Half angle vs. normalized proton energy for the three shots.*

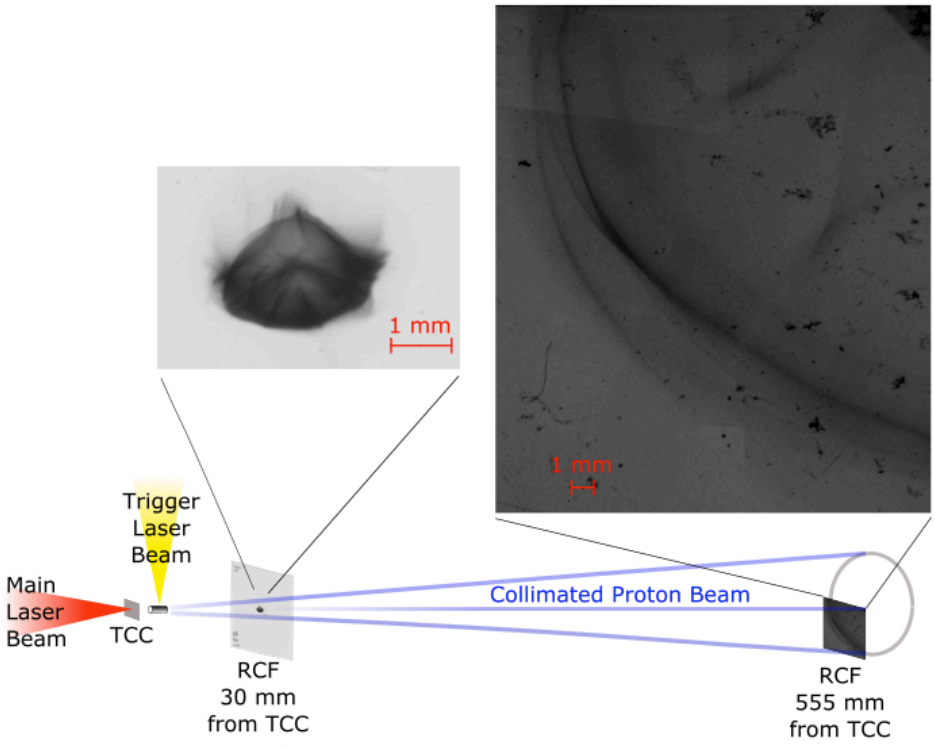

Figure 3.20 *Illustrative scheme of the proton beam collimation after the cylinder. The details on top show the structure of the proton beam at different locations.*

The divergence of this third shot has been analyzed and a comparison with the other two stacks is presented in Figure 3.19. For similar proton energy, the divergences for the shot #107 and shot #111 are almost the same. This means that the proton beam is not focused in one point but only collimated over a long distance, as shown in Figure 3.20.

In the same figure is also pointed out the detail of the proton beam spatial structure. The structures observed at the two locations are similar and evidence the non-uniformity of the proton beam. This can be due to a non-uniformity of the

full proton beam itself (a plastic target is known [Fuchs *et al.*, 2003] to generate a non-uniform TNSA proton beam). But this could be due as well to the transient electric field inside the cylinder that is probably not uniform (see the probing of such beam shown in [Chen *et al.*, 2012]).

A second confirmation that the proton beam was collimated can be obtained considering the formula presented by [Gordienko *et al.*, 2006]. According to the authors, for a fixed value of T_{e0}, the lens collimates ions with energy:

$$E_p \propto Z_p k_B T_{e0} \frac{LD}{R^2}. \tag{3.19}$$

Where Z_p is the charge of the ion, D the distance from TCC to the beginning of the cylinder, R the cylinder's radius and L the cylinder's length. Since protons having different energies are in different positions inside the cylinder when it is triggered, and each travel for a different distance during the time over which the transient electric field acts, each energy sees a different active length in the cylinder. During the 30 ps of the electric field duration, the slower protons travel less than the higher energy protons. On the other hand, the faster protons are already close to the exit of the cylinder when it is triggered, and they can make a part of their path outside the cylinder. The distance $L = f(E_p)$ travelled inside the cylinder by protons having different energies is represented with red points on Figure 3.21, where the dotted line is the curve predicted by (3.19). We can observe from the figure that up to around 6 MeV the dotted line and the red points overlap. This means that protons having these energies have travelled the exact distance to be collimated. For the higher energies the travelled distance seems to be lower than the one needed according to Gordienko's formula.

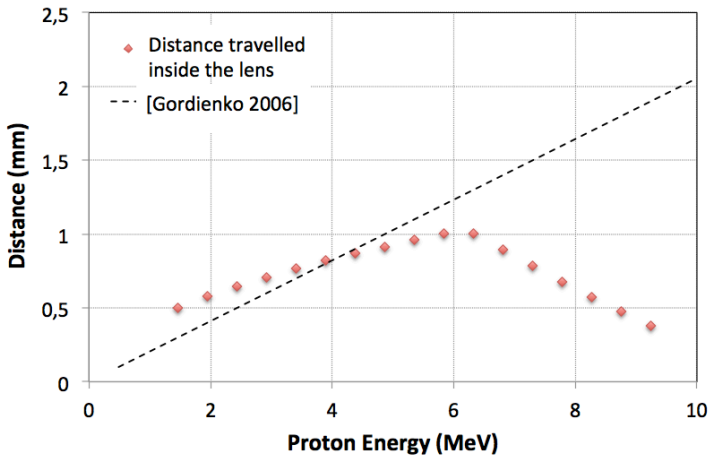

Figure 3.21 *The dotted line is Gordienko's formula (equation 3.19), while the red points represent the distance that a proton of a certain energy travels inside the cylinder while the electric field is acting.*

3.1.3 Filtering of the Proton Spectrum

In the previous section I discussed the effects of the lens on the divergence angle of the proton beam concluding that under our experimental conditions, we were able to collimate the proton beam over a long distance. This effect can be used to filter the proton energy spectrum over a long distance.

Comparing the proton energy spectrum of the case without lens (§ 3.1.1) and of the case with lens (§ 3.1.2), both present the typically TNSA broadband spectra with a quasi-exponential decay. In the case without lens, the number of protons is around an order of magnitude higher than in the case with lens. This means that passing through the cylinder part of the proton beam is lost. However, if on one hand the lens decreases the total number of protons, on the other hand it acts on their spatial density.

The divergence of protons with energy E can be described by the half angle ϑ(E) presented in § 2.1 but as well by the solid angle $\Omega(E)$ of the cone that contains the protons of energy E. The solid angle of the cone that has an angular apex of 2ϑ(E) is:

$$\Omega(E) = 2\pi\big(1 - \cos\big(\vartheta(\mathrm{E})\big)\big). \tag{3.20}$$

It represents the area of a spherical cap on a unit sphere. It can also be calculated by the ratio between the area A_{cap} that the cone intercepts on a sphere of radius R_{sphere}, and this radius squared. For small cone apex, this ratio can be approximated by the ratio between the base area of the spherical cap and the squared distance between the cone vertex and the spherical cap base (see Figure 3.22):

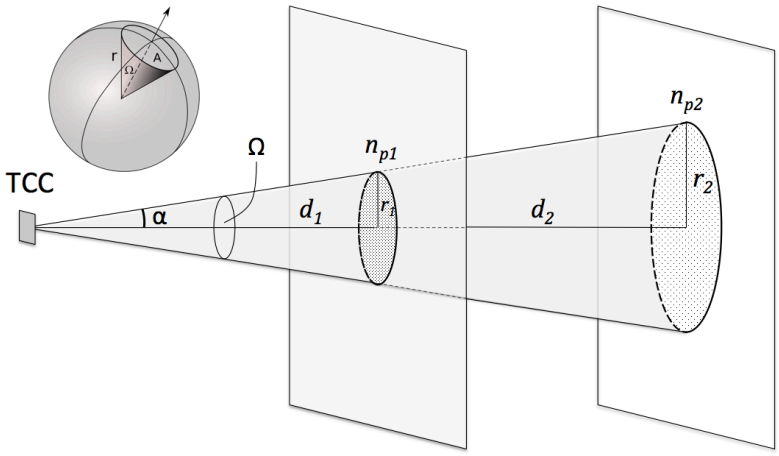

Figure 3.22 *Scheme of the solid angle and proton density over several planes.*

$$\Omega = \frac{A_{cap}}{R_{sphere}^2} \approx \frac{\pi r_{cap}^2}{d^2}. \tag{3.21}$$

Using the solid angle it is possible to define the proton density on a plane perpendicular to the proton beam direction at a distance d from TCC:

$$n_p(E,d) = \frac{N_p(E)}{\Omega(E) d^2}. \tag{3.22}$$

Where $N_p(E)$ and $\Omega(E)$ are respectively the total number of protons of energy E and the solid angle of the cone containing the diverging proton beam of energy E. For a fixed solid angle the proton density decreases like $1/d^2$.

Collimating the proton beam we are modifying the solid angle that contains protons of certain energy. The more an energy is collimated, the more the solid angle is small. For a surface at a fixed distance d from TCC, the proton density of the collimated beam will be $\Omega_{not-coll}/\Omega_{coll}$ times than the proton density of the non-collimated one.

$$\Omega_{coll} \ll \Omega_{non-coll} \implies n_{p_{coll}} \gg n_{p_{non-coll}}. \tag{3.23}$$

The plot of Figure 3.23 presents the ratio between the solid angle of the non-collimated beam and the collimated one versus proton energy. The lens had modified not too much the solid angle of the low energy protons while the ratio is almost 70 for protons between 5.3 and 6.3 MeV. This means that, if for the low energy protons their density is almost the same, for the higher energy protons their density will be almost 70 times higher.

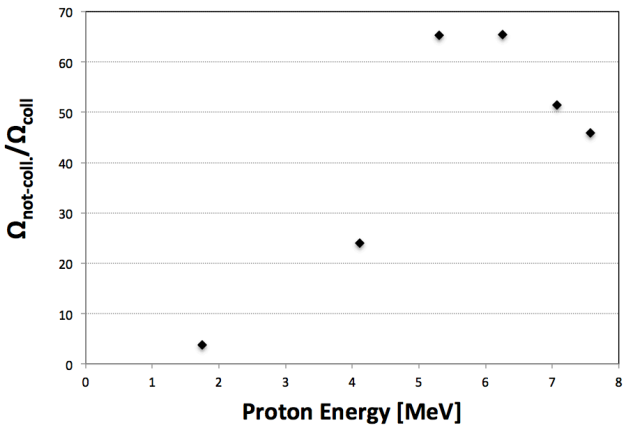

Figure 3.23 *Ratio between the non-collimated protons solid angle and the collimated protons solid angle for various energies.*

$$E_p = 1\ MeV \quad \longrightarrow \quad n_{p_{coll}} \approx n_{p_{non-coll}}\,, \qquad (3.24)$$
$$E_p = 5 - 6\ MeV \quad \longrightarrow \quad n_{p_{coll}} \approx 70\, n_{p_{non-coll}}\,.$$

Considering the total number of protons, the lens did not modify the slope of the energy spectrum decay, it had just shifted the spectrum downward, see the first plot of Figure 3.24. But the proton density (equation 3.22) for a fixed distance for the energy around 6 MeV is widely increased, as is shown in the second plot of Figure 3.24, where the total proton energy density is divided by the solid angle subtended by the signal.

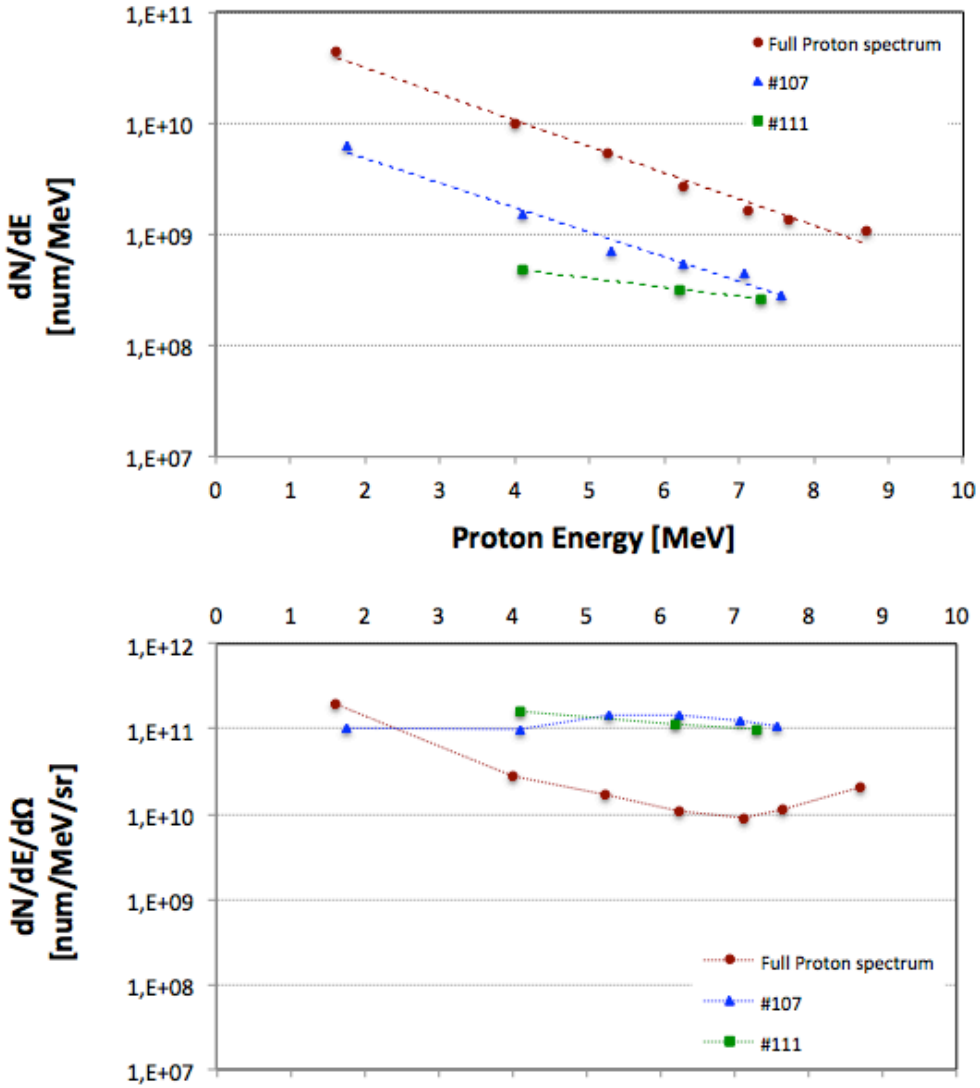

Figure 3.24 *(Top) Full proton energy spectrum. (Below) The energy proton spectrum divided by the solid angle characteristic of each energy. Shot #107 and Shot #111 are the ones described in § 3.1.2, and they represent the collimated proton beam.*

In order to modify the proton spectrum impinging on the LiF, the latter has been moved far away from TCC. In that way we decreased the solid angle $\Omega_{catched}$ by which the catcher is seen from the target, generating a filter for all the proton energies with solid angle $\Omega(E) < \Omega_{catched}(d)$ at distance d. From equation (3.22) we can deduce that the number of protons of energy E impinging on the catcher is:

$$N_{p\ on\ catcher}(E,d) = n_p(E,d)\, A_{catcher} = N_p(E)\frac{\Omega_{catcher}(d)}{\Omega(E)}\ . \qquad (3.25)$$

Therefore the ratio between the solid angle of the catcher at the distance d of the source and the solid angle of the protons having energy E gives the fraction of protons of a certain energy impinging on the catcher. As shown in the second plot of Figure 3.25, proton energy can be selected by modifying the distance between the lens and the catcher.

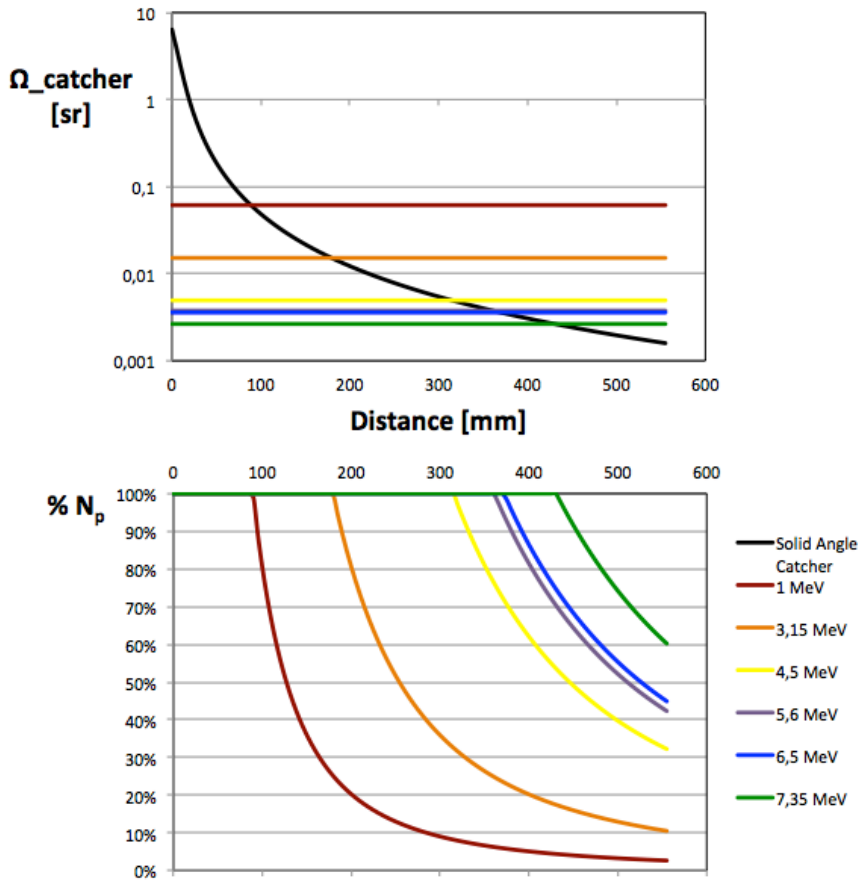

Figure 3.25 *(Top) Solid angle of the catcher as seen from the primary target. The colored lines represent the solid angle of the different energies. (Below) Percentage of how many protons of a certain energy are impinging on the catcher.*

3.1.4 SET-UP C: Neutron Selection

Primary Target:	PET (50 μm of thickness coated with 14 nm Al)
Cylinder:	Al (3 mm length; 940 μm external diameter; 780 μm internal diameter)
Secondary Target:	LiF (25 mm of diameter and 200 μm of thickness)
Beams:	Main and Trigger Beam
Diagnostics:	CR-39, nToF, Bubbles Detector Spectrometers for neutron detection

In the third phase of the experiment we tried to select the neutrons in energy using the proton beams modified by the laser-triggered micro lens. The arrangement inside the chamber was similar to the one of **set-up B** for the lens placement and similar to the one of **set-up A** for the nToF position. In order to take advantage of the proton beam collimation, we moved the LiF at 555 mm from TCC. Figure 3.26 shows a schematic drawing of this last **set-up C**.

Comparing with the set-up A of § 3.1.1, where the LiF was 2 mm after TCC and all the proton beam was collected into the catcher, in this set-up C, only a fraction of the proton beam hits the LiF.

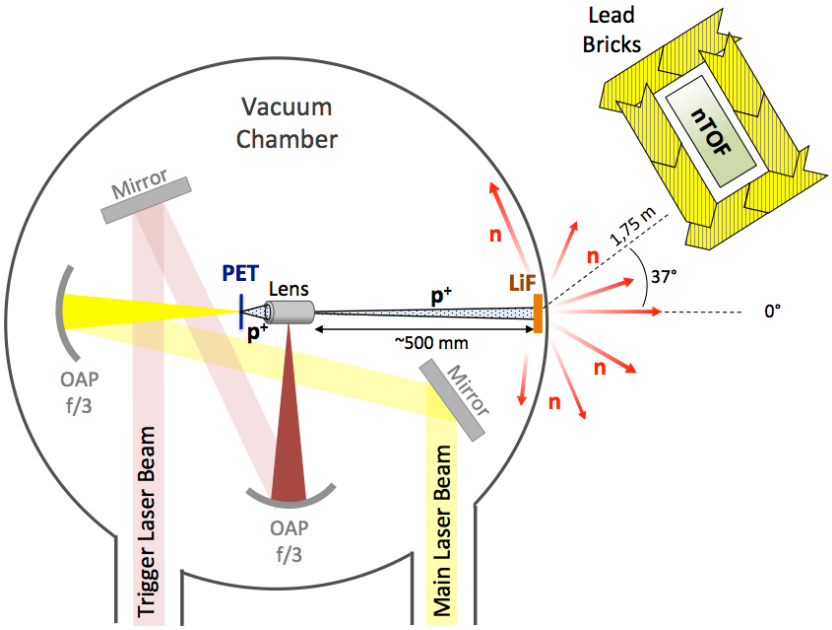

Figure 3.26 *Scheme of set-up C used during the third phase of the experiment.*

From the considerations made in the previous section, to obtain the shape of the proton spectrum in the set-up C as seen by the catcher (in the different conditions explored without and with the lens), it is sufficient to multiply the signals of Figure 3.24 (below) by the solid angle of the catcher at 555 mm:

$$\Omega_{catched}(d = 555\ mm) = 1.59 \times 10^{-3}\ . \qquad (3.26)$$

The resulting proton spectra are shown in Figure 3.27. We can consider these spectra as a credible estimation of the proton spectrum impinging on the catcher in the case of set-up C. The collimated beam of shot #107 and shot #111 (see § 3.1.2) present a completely different trend compared to the full proton spectrum obtained without the lens. Looking at the full proton spectrum obtained without the lens and for the entire solid angle of Figure 3.5, we observe that in the case of set-up A the number of particles varied in the range of $10^{10}\ particles/MeV$ for the low energy protons up to $10^{9}\ particles/MeV$ for the high energy protons. Whereas the simulated spectra for the set-up C shows:

- For the **full proton beam:** a range of particle between $10^{8}\ particles/MeV$ (only for low energies) to $10^{7}\ particles/MeV$
- For the **collimated proton beam:** the number of protons of all energies is of the order of $10^{8}\ particles/MeV$ and, instead of decreasing monotonically, the spectrum presents a maximum around 6 MeV.

These characteristics are visible in Figure 3.27, where is also shown the threshold of 1,88 MeV for the $^{7}Li(p,n)^{7}Be$ reaction that is the principal reaction generating neutron inside the catcher, as shown in §2.1.3.

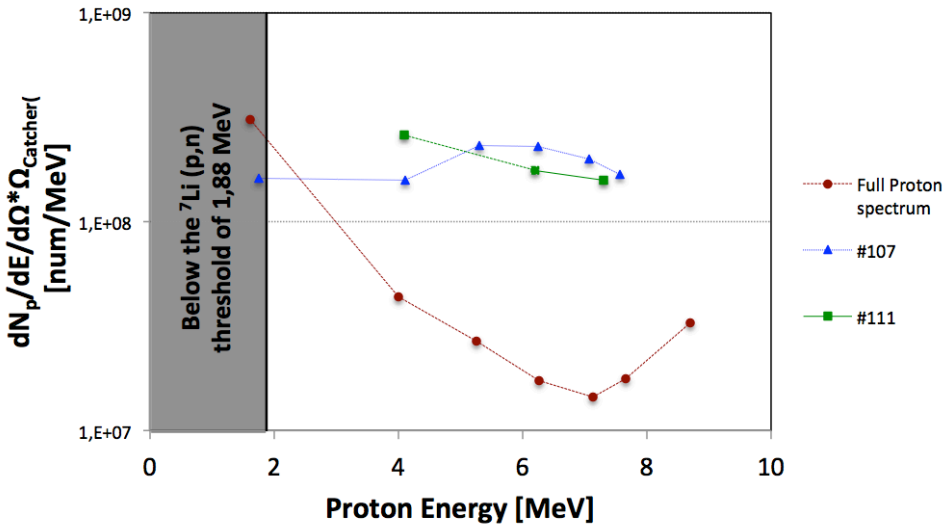

Figure 3.27 *Simulated spectra that should hit the LiF catcher in the set-up C.*

As described in § 3.1.1, in the first phase of the experiment it was critical to detect the number of neutrons using CR-39 and bubbles spectrometers with a correct statistics. It has been necessary in that case to accumulate the signal over several shots. It is obvious that during this third phase of the experiment where the number of protons inside the colliding beam was reduced by a factor 100 for low energy protons and 10 for high energy protons, it was impossible to use these diagnostics. The number of neutrons generated was too low to be detected by CR-39 and bubbles spectrometers with a good statistics. Therefore, during this phase of the experiment, even though these detectors were still used, they did not produce useful data. The number of neutrons produced can only be estimated from the number of protons hitting the target.

Since the aim of this third phase was principally to study the effects of the collimated beam on the neutron spectrum, the nTOF detectors are the dedicated diagnostics. I discuss in the following the results obtained from these diagnostic, making a comparison with the results of § 3.1.1.

These detectors are quite tricky to be used in a laser-plasma interaction environment because they are sensitive not only to neutrons but also to gamma and x-ray radiation. These radiations are generated in high quantity in the zone where the laser interacts with the solid matter of the primary target. They are principally generated by Bremsstrahlung of the hot electrons moving inside the target. Therefore shielding of these detectors from this noisy radiation is crucial to obtain an exploitable neutron signal. During the experiment, we used lead bricks to shield all around the scintillator with 200 mm of Pb.

The neutron spectrum from the same nTOF as used and discussed in § 3.1.1 was analyzed and compared with the signal obtained during the set-up A. We have to note that, if during the set-up A the scintillator was placed at 2.1 m from the LiF position and with an angle of 28° from the 0° forward direction now its position was 1.75 m from the LiF and 37° from the 0° forward direction (see Figure 3.26). The LiF is at the zero position from where the neutrons start to move and this must be taken into account for the evaluation of the time of flight.

Both neutrons signals of set-up A and set-up C have been compared with the case without neutrons signal that is a shot without the catcher in place. During this type of shots, the scintillator only recorded X-rays induced by the electron Bremsstrahlung in the primary target. This signal is used has a fiducial time corresponding to time zero of the laser. The x-ray signal could be higher in the set-up with the lens in place, as two lasers were fired instead of only one.

Figure 3.28 shows the signal of the scintillator in the three cases:

- **(S_0):** without the catcher in place: only gamma and X-ray signal.
- **(S_1):** with the full proton spectrum impinging on the LiF catcher SET-UP A
- **(S_2):** with the spectral modification of the incident proton beam due to the lens collimation - SET-UP C.

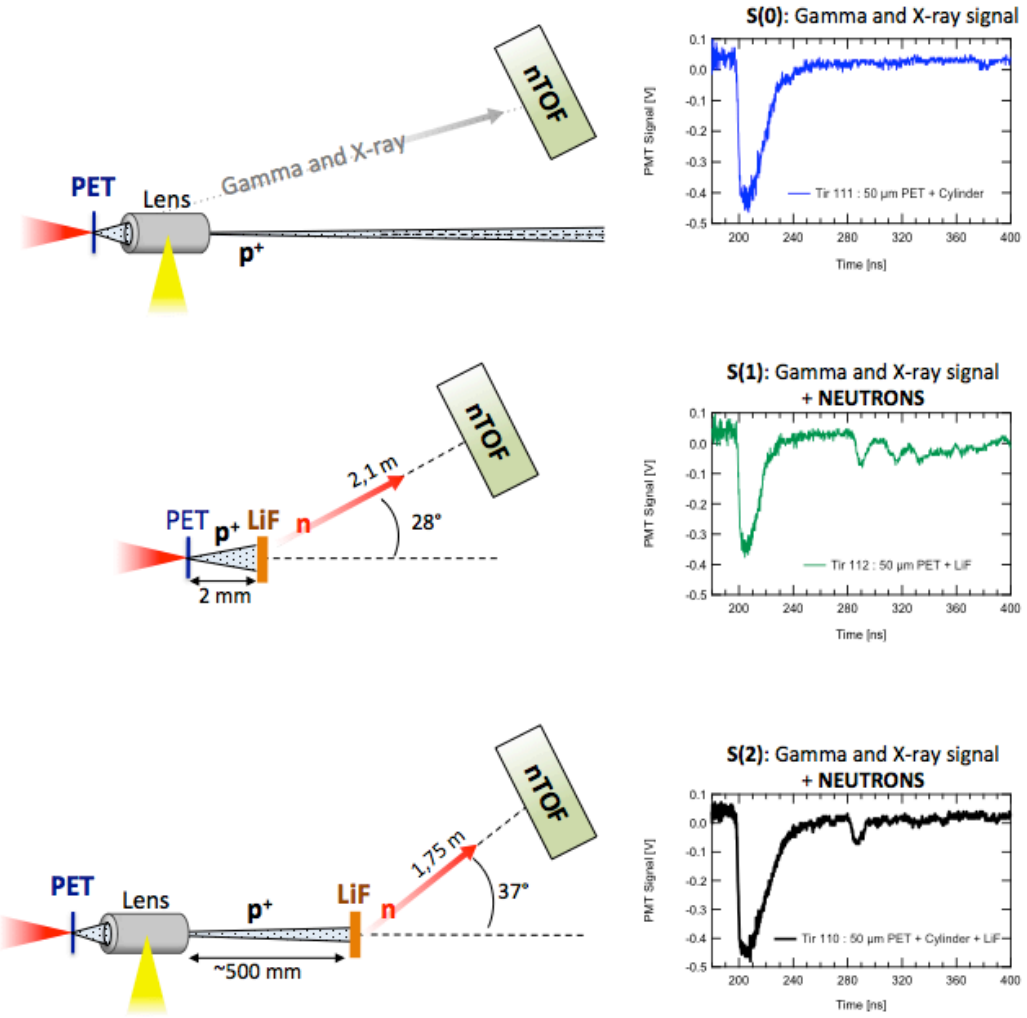

Figure 3.28 *Example of nToF signal in the case without LiF (blue), with neutrons generated by the full proton spectrum (green) and neutrons generated by the modified proton spectrum (black).*

In the top plot (So) of Figure 3.28, only the gamma and the X-ray signal with their decay are visible. It is important to show this non-neutron case to highlight the clean exponential decay of the scintillator signal, i.e. that there are no reflections or spurious signals. The decay is based on the response time of the scintillator.

In Figure 3.29 the three signals are compared on the same graph. The light-colored lines show experimental results when no neutrons are expected (i.e., the SET-UP A for the proton when the RCF stack was used instead of the LiF). The earliest signal, at 10 ns (the peak is not visible with the scale used in this figure), is due, as said, to X-rays induced by electron Bremsstrahlung in the primary target and is used to synchronize to the time zero of the laser.

The dark lines in Figure 3.29 show the experimental signal recorded when using the LiF catcher for neutron production. The upper axis is the neutron energy

that is derived from the location of the nTOF with respect to the LiF and the time of arrival of the neutrons on the detector. We have to take into account, for the (S2) signal, not only the time of flight of the neutron from the LiF to the detector, but also the time of flight of the collimated proton beam from the primary target to the catcher, of the order of 29 ns for 1.88 MeV protons (threshold of the $^{7}Li(p,n)^{7}Be$ reaction) and 13 ns for 9 MeV, the maximum cut-off proton energy.

Neutrons arrive at around 100 ns, corresponding to an energy of 3 MeV. In the (S1) case, the neutron signal extends many hundreds of nanoseconds in time and with energies down to 100 keV. In contrast, the (S2) neutron signal is much shorter in duration and has a significant reduction of lower-energy neutrons due to the modified incident proton spectrum.

The narrow peak in the signal (at 100 ns, with a peak of 2.0 V thus out of the graph) in (S2) is likely due to a single neutron hitting the scintillator. This is because, at this energy (3 MeV), the scattering probability is only 50% in our scintillator and the neutron pulse on the detector is short, only 0.1 n/ns [Higginson *et al.*, 2015]. This explanation is corroborated by the observed similarity between this narrow pulse and the detector's temporal response (both 9 ns FWHM). We note that this statistically limited feature is less important when the energy decreases since the average scattering probability is already 90% at 1 MeV.

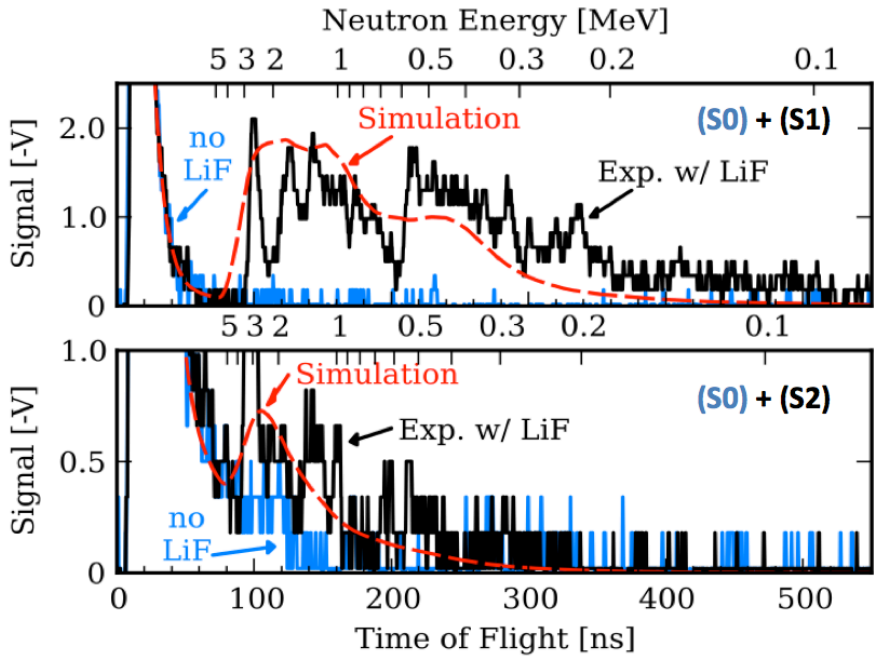

Figure 3.29 *Comparison between the simulated neutron signal (dashed red lines) and the nTOF traces from experimental data: (Top) for neutron production in case (S1) and (Below) for neutron production in case (S2). The (S0) is the reference blue line of the case without neutron production. Time zero corresponds to the arrival of the laser on the PET target..*

MCNP6 Simulation

In order to better understand these signals, the Monte Carlo particle transport code MCNP6 [Pelowitz 2013] was run. This code includes particle scattering, energy loss, and nuclear interactions. The proton-induced nuclear reactions included were $^{7}Li(p,n)^{7}Be$, $^{6}Li(p,n)^{6}Be$ and $^{19}F(p,n)^{19}Ne$, which have cross sections resolved in angle. The simulation did not include reactions producing excited states in the final nuclei or other reaction channels yielding neutrons such as breakup; however, these have cross sections below 10% of the main reactions. When benchmarking the code, we noticed that the standard cross section (ENDF/B-VII.O [Chadwick *et al.*, 2006]) used by the code differed considerably from the experimental data [Liskien *et* Paulsen 1975] [Abramovich *et al.* 1984], as does TENDL-2013 [Koning *et* Rochman 2012] below 15 MeV (see Figure 3.30). Thus, a recently reworked cross section was used instead [Parsons *et* Gale 2015].

The geometry of the simulation reproduced the experimental set-ups with protons injected from the location of the primary target and directed, using straight trajectories, towards a LiF disk at the position of SET-UP A (2 mm from the PET primary target) or the position of SET-UP C (555 mm from PET primary target). The protons were given the measured exponential spectra described in Figure 3.5 for the SET-UP A case simulation. The simulations recorded in that case a neutron yield in the forward direction of 2.8 and 3.9×10^{5} $n/MeV/sr/shot$ that is in the energy range of the CR-39 and bubble detectors, respectively. Therefore is consistent with the experimental measurements shown in § 3.1.1.

To reproduce the neutron time-of-flight data, detectors were placed in the simulations at the same location and dimensions as the scintillators used in the experiment.

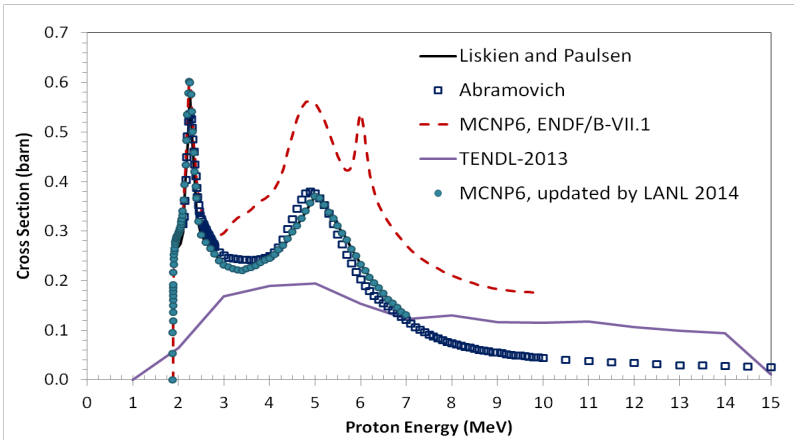

Figure 3.30 *Cross sections of the dominant reaction $^{7}Li(p,n)^{7}Be$. The standard cross section used in MCNP6 code for this reaction was taken from ENDF database and it did not match experimental data [Liskien* et *Paulsen 1975] [Abramovich* et al. *1984]. LANL was able to reanalyze the reaction to give a better fit [Parsons* et *Gale 2015].*

The simulations included the neutron scattering induced from lead shielding along the line of sight from source to detector, as well as scattering sources near the detector (e.g., the steel chamber, concrete walls, concrete floor, and other Pb walls present in the experimental room). MCNP6 collected the number of neutrons passing through the detector and binned them in energy and time. The neutron detector efficiency was determined in the following manner. First, the spectrum of protons scattered by neutrons (at these energies, scattering of C and nuclear processes can be neglected) was determined using other simulations with MCNP6.

Next, the light response (in units of electron-equivalent response) of the protons was determined by applying the light response function from Birks' formula [Craun *et* Smith 1970] (kB value from [Altstadt *et al.*, 2007] for NE-102). Finally, the electron equivalent response was converted to a signal using a calibration performed with a ^{60}Co gamma source to complete the absolute calibration. Additionally, the ^{60}Co source was used to fit the detector's temporal response with two exponential decays, which was then convolved with the calibrated neutron signal to give a simulated signal, as well as an x-ray falloff.

The simulated signals of the simulations are shown as dashed lines in Figure 3.29. These are in agreement with the experimental shape of the data and, especially, the absolute number, which has not been arbitrarily normalized. This agreement highlights the importance of including nearby structures, as we found that these scattering structures (i.e., those not along the direct line of sight) contributed from 40% to 80% of the neutrons detected at 3 MeV in the (S1) and (S3) signals, respectively.

To determine the loss of neutrons through the selection process, we look at the yield of 3 MeV neutrons on the scintillator, which are $4\times10^4\ n/MeV/sr/shot$ for the (S1) signal and $1.2\times10^4\ n/MeV/sr/shot$ for the (S3) signal. This shows that the neutron yield was only reduced to 30% of the original yield, despite the large (0.56 m) distance traveled by the protons. Using the simulations, we investigate the temporal narrowing achieved by placing a virtual detector consisting of a neutron counting sphere of 2.5 mm radius at 0.5 m from the proton emission (i.e., 5 mm from the LiF in the S3 case) to record all of the neutrons that pass through it. This virtual measurement shows a FWHM duration of 30 ns in the (S1) case and 3.4 ns in the (S3) case, thus, temporal narrowing of a factor of about 10. This reduction is due to the energy selection of the protons hitting the LiF. Since the low-energy protons are dramatically reduced the time-of-flight broadening is reduced as well. This duration compares well with existing accelerator driven devices that go from few ns to hundred of ns, as presented in [Altstadt *et al.*, 2007] and references therein. Additionally, we note that moving the LiF slab to 100 mm would lower the pulse to sub-nanosecond duration, while at the same time staying a long distance away from the laser interaction to allow for proper shielding.

3.1.5 Conclusions for the ELFIE experimental campaign

In the previous sections I showed the principal results we obtained during this experimental campaign at ELFIE. Although this experiment was the first test of neutron production in our laboratory and in the facility, and although the research topic was completely new for the majority of the group, it had produced an interesting outcome.

The collimation of a TNSA proton beam over a long distance has been realized, and due to the fact that the collimation is slightly different for different proton energies, we obtained a modification of the proton spectrum over a long distance.

The possibility to produce neutrons on the ELFIE facility using a TNSA proton beam and a LiF catcher has been showed. The neutron flux achieved was about $10^5\ n/MeV$, which is not sufficiently high for real applications of this source in other scientific domains (e.g. neutron radiography), but it is anyway a good starting point for the future.

Using the proton beam collimated by the lens, instead of the normal TNSA proton beam, we have been able to generate a shorter neutron signal from the LiF catcher. We showed that this was due to a change in the proton energy spectrum that leads to a narrowing of the neutron pulse duration. We obtained a neutron pulse duration of about a 3 ns and $10^5\ n/MeV/sr/shot$. Simulations have been performed to qualitatively confirm our results.

This experimental campaign was really short, only two weeks, so we didn't have enough time to test in more detail the lens collimation mechanism (for instance changing the delay between the two beams) or the angular distribution of the neutron source. Therefore, at the end of this experiment we decided to perform a second campaign to investigate thoroughly the possibilities and the limits of proton energy selection by the laser-triggered micro lens and the consequent neutron spectrum modification. The set-up, the implementation and the results obtained in this second campaign are described in the next section.

3.2 Second Experimental Campaign (TITAN)

We performed the second experimental campaign in November 2014 (over 4 weeks) using the TITAN laser platform of the Jupiter Laser Facility (JLF). The Jupiter Laser Facility is an institutional user facility, which is part of the Lawrence Livermore National Laboratory (LLNL) in California (USA).

Titan is a two-beams laser platform. The nanosecond "long-pulse" beam delivers up to 1 kJ at wavelength of 1.053 μm. The "short-pulse" beam is 1-to-10 ps long and has energies up to 250 J, depending on pulse duration. On target, it has a minimum focal spot diameter of a few μm, with intensities up to 10^{21} W/cm^2. The beams can be used together or independently. During our experiment, we only used the short-pulse that was split in two branches after the high repetition rate pre-amplifiers, and before the high-energy amplifier (when the beam is ~ 15 mm in diameter). This way, we could have two beams arriving inside the experimental vacuum chamber, one to accelerate the proton beam and the other one to trigger the micro-lens, as in the ELFIE experimental scheme. This is shown in Figure 3.32. It is important to highlight that, nowadays, the number of laser facilities around the word that allow the simultaneous use of two high intensity (higher than $10^{18}\,Wcm^{-2}$) and short-pulse (less than ps) laser beams, is really limited (e.g. Gemini or ELFIE).

This laser uses the *optical parametric chirped pulse amplification* (OPCPA) technique, where Nd:glass is used as the amplifying medium at a wavelength $\lambda_L = 1054\,nm$. For our experiment, we chose to set the pulse duration to $\tau_L = 650\,fs$. The on-target energy was ~$100\,J$ and we used two f-3 off-axis parabolic mirrors inside the experimental vacuum chamber to focus the beams on the primary target and the cylinder respectively. We obtained an 8 μm FWHM focal spot leading to a peak intensity around $10^{20}\,Wcm^{-2}$. While the energy of the laser pulse in this facility is much higher than on ELFIE, the repetition rate is a bit lower, and the entire laser system takes approximately 30 minutes to cool down before being available for a new shot. Also the process to put under vacuum (before the shot) and vent (after the shot) the chamber is slower compared to ELFIE. Moreover the laser is shared with a second experimental room and this decreases again the number of shots per day for each experiment (maximum 7/8 per day, with only 4 days per week of shooting time). Consequently, during the entire campaign, we carried out around 80 shots.

The time delay between the two beams inside the chamber was obtained with an optical delay line before the compressor. The synchronization between the beams inside the chamber was achieved in a first step by using a streak camera, followed by the interference technique (the same described in the first introductory paragraphs of § 3.1 for the ELFIE experiment) with a precision of a

fraction of the laser pulse duration (~100 fs).

The Titan short laser pulse has a prepulse of 1 mJ (at the lowest peak intensity) up to 18 mJ (at the highest peak intensity) that lasts approximately 2 ns before the peak of the pulse (see Figure 3.31). Because of the extremely high peak laser intensities, even if the prepulse is hundred million times less intense (10^{-8}) than the peak of the main pulse, it can still have intensities up to $10^{12}\ W cm^{-2}$.

The intensity of the TITAN prepulse is lower compared to the ELFIE experiment, but it is still high enough to ionize and ablate material from the target. Since, in general, prepulses come nanoseconds before the main pulse, there is a significant amount of time for the initial target to be heated and to expand. This creates a preplasma that expands in front of the initial target surface over hundreds of microns, and, as already discussed, prevents the use of targets with thickness below 10 μm.

As already mentioned, this second experimental campaign was carried out to improve our understanding of the micro lens and the neutron source modification. The principal aims of this campaign were:

- **Studying the lens focusing mechanism** and try to select specific proton energies with a pinhole (see § 3.2.1 and § 3.2.2).
- Obtaining a **higher neutron flux**. Using a more powerful laser system gave us the possibility to obtain higher maximum proton energies for the accelerated proton beam, and a higher total number of particles (see § 3.2.3).
- Trying to realize a **better selection in energy of the neutron beam** (§ 3.2.4).

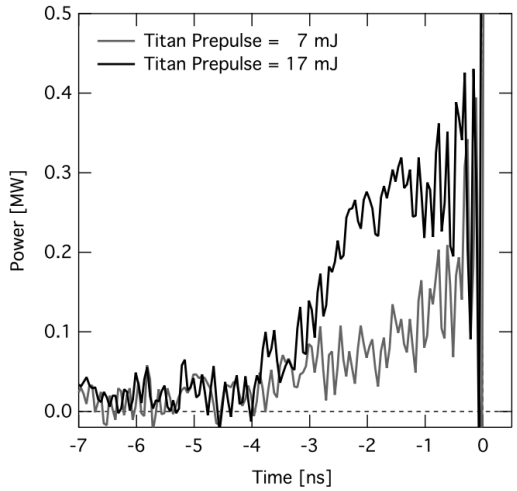

Figure 3.31 *Prepulse levels of the Titan laser short-pulse arm from [D.P.Higginson Thesis 2012] plotted on a linear scale.*

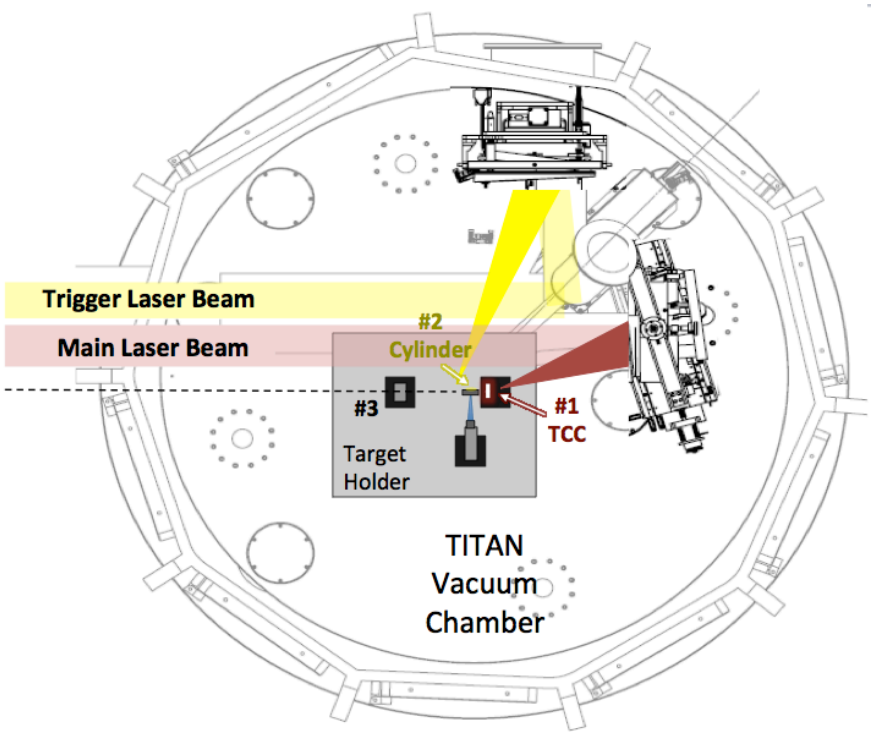

Figure 3.32 *Scheme of how the two beams were focused inside the TITAN vacuum chamber. On the target holder there were three positions: (#1) TCC – where the PET primary target was; (#2) Cylinder-lens position; (#3) where, depending on the requirements, we could put RCF, grid, LiF and pinhole.*

Using the experience acquired during the first campaign, we improved the set-up of the experiment. The target holder has been modified in order to make the alignment stage easier and faster and, to improve the precision of the cylinder alignment. Due to the limited number of shots per day, it was crucial not to waste a lot of shots for the alignment, as was the case during the ELFIE campaign. On the diagnostic side we increased the number of nTOF detectors used for neutron detection, and we decided to test the activation diagnostic both for protons (§ 2.2.1.2) and for neutrons (§ 2.2.2.4).

This experiment has been divided into different experimental phases:

1. Study of the focusing mechanism of the protons.
2. Selection in energy of part of the focused protons.
3. Production of neutrons using a LiF catcher and a full proton energy spectrum.
4. Production of neutrons using a LiF catcher and a selected proton energy spectrum.

In the following sections I detail each of these phases, the experimental data obtained, the experimental difficulties encountered and the state of the analysis of the results up to now.

3.2.1 SET-UP 1: Study of the focusing mechanism of the protons

Primary Target:	PET (23 μm thickness coated with 14 nm Al)
Cylinder:	Al (3 ± 0,1 mm length; 940 μm external diameter; 780 μm internal diameter)
Grid:	100 line per inch (lpi)
Pinhole:	-
Secondary Target:	-
Beams:	Main and Trigger Beam
Diagnostics:	RCF stack for proton detection
	nToF detectors for gamma and background detection

As in the ELFIE experimental campaign, the first step was to characterize the laser accelerated proton beam. As we knew that the shot to shot variation of the laser pulse energy was ~15%, to save on the number of shots, we only made few shots in a configuration similar to the SET-UP A of § 3.1.1 to check the beam quality and the energy proton spectrum.

As said in § 3.1.1, during an experiment on neutron generation, it is better to avoid metal targets to accelerate protons in order to limit the undesired X or gamma radiation from this primary target. We tested two plastic materials: 23 μm of aluminized PET (*polyethylene terephthalate*) and 12.5 μm of aluminized PolyP (*polypropylene*). We decided to use the first one (as during the ELFIE experiment) that was more rigid and less difficult to align, and as already mentioned, using the micro-lens device, it is crucial to have the possibility to align the primary target with respect to the cylinder as precisely as possible.

The proton spectrum generated from the 23 μm of aluminized PET was recorded by a RCF stack positioned 35 mm away from the primary target. The RCF pack was composed of 30 HD-810 films. After the 20th layer, the RCF films were alternated with 500 μm of PET in order to limit the number of films we had to use (see Figure 3.33). The films showed signals up to the 26th layer, which is equivalent to a maximum proton energy of around 30.5 MeV.

With the same program as described in § 3.1.1, we obtained the proton energy spectrum shown in Figure 3.34. The proton spectrum, $\frac{dN_p}{dE}(E)$, was well-fit using an exponential spectrum:

$$\begin{aligned} &for\ E < E_{max} && \frac{dN_p}{dE}(E) = \frac{N_0}{T}\exp\left(-\frac{E}{T}\right), \\ &for\ E > E_{max} && \frac{dN_p}{dE}(E) = 0\,. \end{aligned} \tag{3.27}$$

Where E is the proton energy, $N_0 = 2.14\times10^{12}$ the total proton number, $T = 6.3\ MeV$ the slope temperature, and $E_{max} = 30.5\ MeV$ is the cut-off or maximum proton energy. For us, this was the reference **full proton spectrum**.

As shown in Figure 3.33, the proton beam was larger than the size of the RCF. Therefore, in this case, it was not possible the retrieve the half-angle divergence as a function of the proton energy. Also in this case, due to the use of a plastic target, the full proton beam is clearly not uniform.

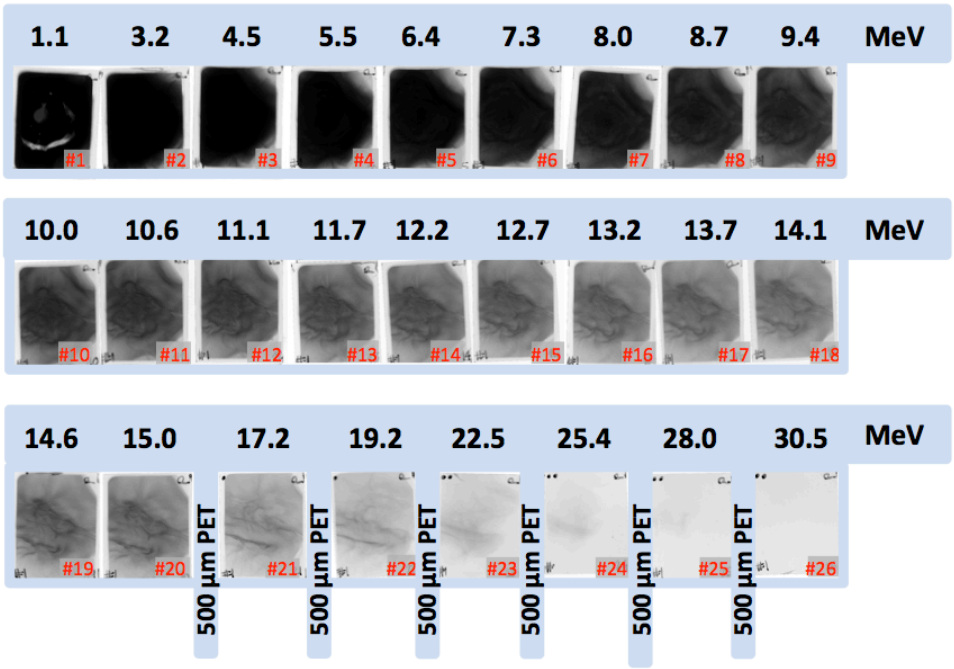

Figure 3.33 *RCF stack of the full proton spectrum obtained from a 23 µm aluminized PET primary target.*

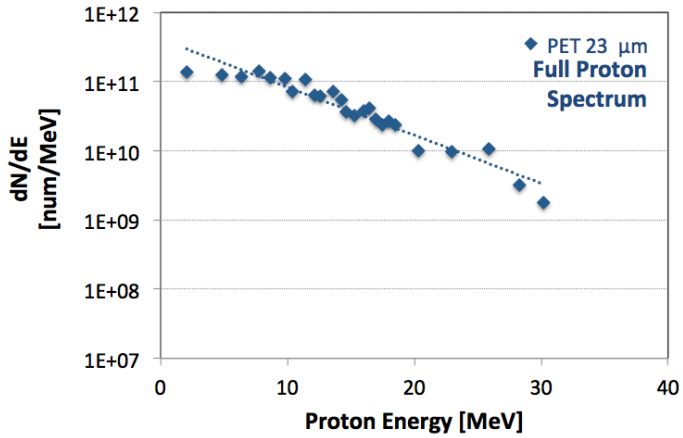

Figure 3.34 *Full proton spectrum obtained from the RCF stack of Figure 3.33.*

The activation of the RCF layers was measured using the NATALIE system [Tarisien *et al.*, 2011], as described in § 2.2.1.2, but unfortunately the results from this diagnostic are not yet available.

After these first shots dedicated to the measurements of the full proton spectrum achievable on the TITAN facility, we carried out a systematic study of the focusing mechanism of the lens by varying:

- The timing between the main and the trigger beam.
- The energy of the trigger beam.

We used an aluminum hollow cylinder of the same dimensions than the one used during the ELFIE campaign, and we put it 1 mm away from the primary target.

Note that it was not possible to position the RCF stack as close to the target-cylinder as in the ELFIE experiment. Indeed, in this case, the RCF stack would be too close to the focus point of the protons and it would be damaged by the high proton flux, making the data non-exploitable. Nevertheless, to try to record some information close to the focus point, we used the autoradiography technique. Namely we put a stack of copper foils instead of the RCF stack. Protons with energy higher than 2 MeV produce nuclear reactions in copper ($^{65}Cu(p,n)^{65}Zn$; $^{63}Cu(p,n)^{63}Zn$). Both *zinc* isotopes produced by the reactions are unstable and decay 100% via electronic capture emitting gamma rays. An image plate superposed on the copper foils then measured the radioactive decays of the activated nuclei, thus giving information on the proton spatial distribution. Analyzing the scans of the image plates, we measured a proton beam diameter of about 200 µm at 9 mm from the primary target, and 5 mm from the end of the cylinder.

Alternatively, in order to obtain information about the proton beam divergence, we used a grid. During each shot, we positioned a grid between the end of the cylinder and the RCF stack, as shown in Figure 3.35. We varied the distances between the end of the cylinder and the grid, in order to investigate the proton beam at different positions.

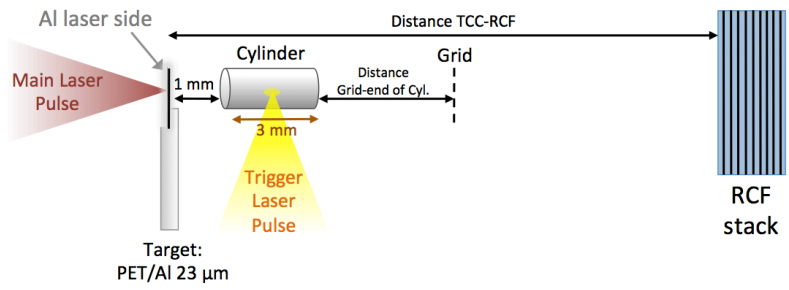

Figure 3.35 *Set-up used for the focusing study. The distance between the end of the cylinder and the grid, and the distance between TCC and the RCF stack were varied depending on experimental conditions.*

Considering the very good laminarity of a TNSA proton beam, as described in § 2.1.1, we assumed that the trajectories of protons of a given energy do not cross. This hypothesis allows us to infer the possible focus position of each proton energy E_p, by looking at the projection of the grid on the RCF layer corresponding to the energy E_p.

In particular, we investigated three time delays between the main laser pulse and the trigger laser pulse, also varying the energy of the trigger beam for one of these delays. The following table describes the experimental conditions of some of the shots which will be discussed later.

ΔT [ps]	Trigger Pulse Energy	Distance TCC-grid [mm]	Shot
90 ps	Full Energy	25 mm	Shot #34
			Shot #40
		10 mm	Shot #39
	½ Energy	25 mm	Shot #48
	¼ Energy	25 mm	Shot #50
63 ps	Full Energy	25 mm	Shot #35
50 ps	Full Energy	25 mm	Shot #36

Table 3.1 *Parameters for the study of proton focusing as shown in Figure 3.35.*

Before discussing the analysis of the shots presented in table 3.1, it is useful to estimate the typical parameters of the plasma expansion inside the cylinder. This can be done with the procedure used in § 3.1.2 to estimate the values for the ELFIE experiment. Both the values for the ELFIE and TITAN experiments are presented in table 3.2.

While for the ELFIE campaign, we concluded that the total duration of the lens action was around 30 ps, with a similar method we can estimate that, on TITAN, the lens switched off between 15 and 20 ps after it was triggered.

The main difference in the parameters is due to the larger number of hot electrons on TITAN because of both the larger laser energy and the better absorption efficiency.

	ELFIE	**TITAN**
Laser Intensity I_0	$3.6\times10^{19}\ Wcm^{-2}$	$10^{20}\ Wcm^{-2}$
Laser pulse energy E_{laser}	$10\ J$	$33\ J$
Laser pulse duration τ_{laser}	$0.35\ ps$	$0.65\ ps$
Hot electron spread time τ_{spread}	$10\ ps$	$10\ ps$
Hot electron temperature $k_B T_{e0}$	$740\ keV$	$1033\ keV$
Laser conversion efficiency f	0.35	0.75
Total number of electrons N_{e0}	3×10^{13}	1.6×10^{14}
Electron density n_{e0}	$4\times10^{23}m^{-3}$	$8.2\times10^{24}m^{-3}$
Debye Length λ_D	$10\ \mu m$	$2.6\ \mu m$
Ion-acoustic velocity c_s	$8.4\times10^{-3}\ mm/ps$	$9.9\times10^{-3}\ mm/ps$
Ion plasma frequency ω_{pi}	$8.3\times10^{11}\ rad/s$	$3.8\times10^{12}\ rad/s$
Final velocity v_{final}	$3.2\times10^{-2}\ mm/ps$	$5.2\times10^{-2}\ mm/ps$
Transient electric field duration τ_E	$\sim14\ ps$	$\sim7\ ps$

Table 3.2 *Comparison between the estimations of the plasma expansion parameters of the two experimental campaigns.*

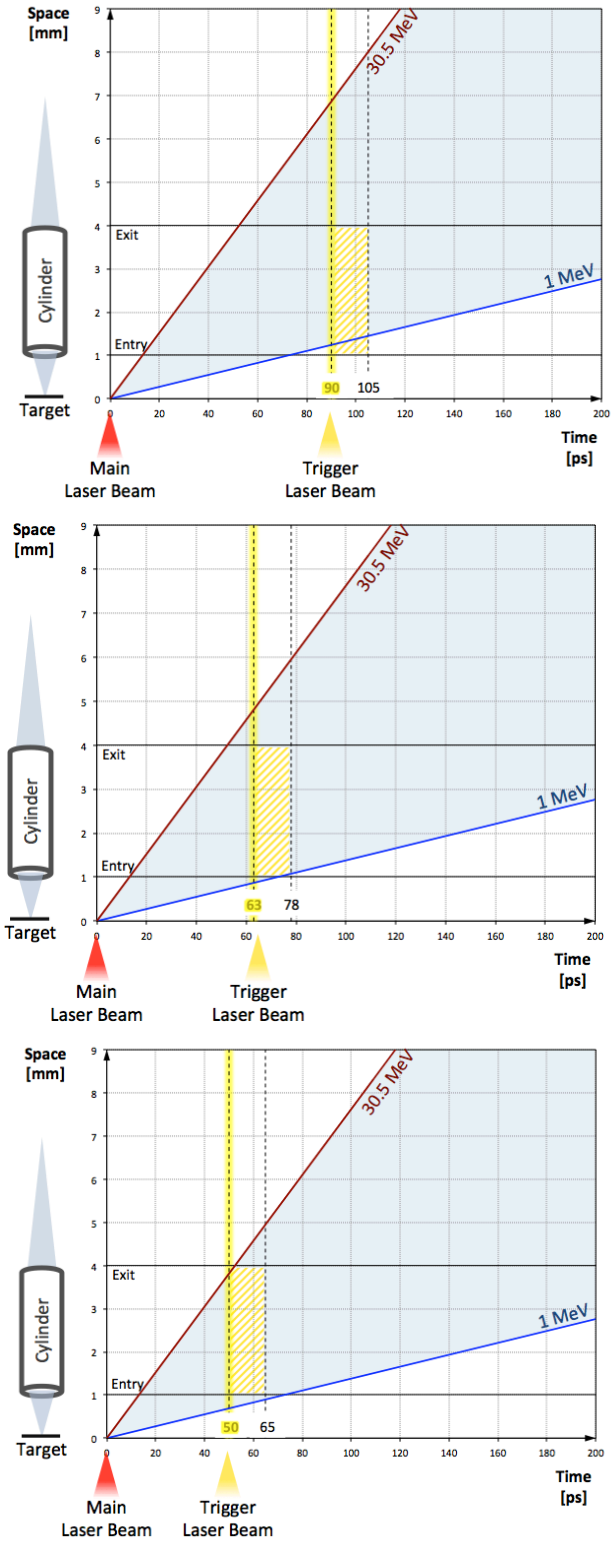

Figure 3.36 *Space vs. time graph of protons flying from the main source to and through the cylinder, for three time delays between the two beams (90 ps; 63 ps; 50 ps). The light blue cone represents the debunching over time and space of the proton beam.*

The study of the proton beam propagation up to the RCF films has been done thanks to a "ray-tracing" program specifically written for this purpose. To obtain the focusing position of protons of different energies, a procedure has been developed to analyze the RCF images that contain the projection of the grid:

1. The centre of the proton beam is identified.
2. The different grid points (i, j) are identified with respect to the centre (0,0).
3. For each point, the equation of the straight line passing by the point on the RCF and the corresponding point on the real grid is defined
4. For each plane (x, y) perpendicular to the direction z of proton propagation a ***mean distance*** is defined as:

$$d_{mean}(z) = \frac{\sum d_{ij}(z)\, w_{ij}}{num.points} \ . \qquad (3.28)$$

   Where d_{ij} is the distance from the point (i, j) to the axis (0,0) multiplied by a weight[3] w_{ij}. Indeed, the idea of using such a weight is to privilege the protons that have been really deviated inside the cylinder.
5. The program plots the ***mean distance*** d_{mean} as a function of the position z along the axis. The position where the value of d_{mean} is minimum is considered as the position of the focus point for a given energy.

For each energy, observing the projection of the grid on the RCF, it is easy to distinguish the part of the proton beam that has been effectively deviated by the lens.

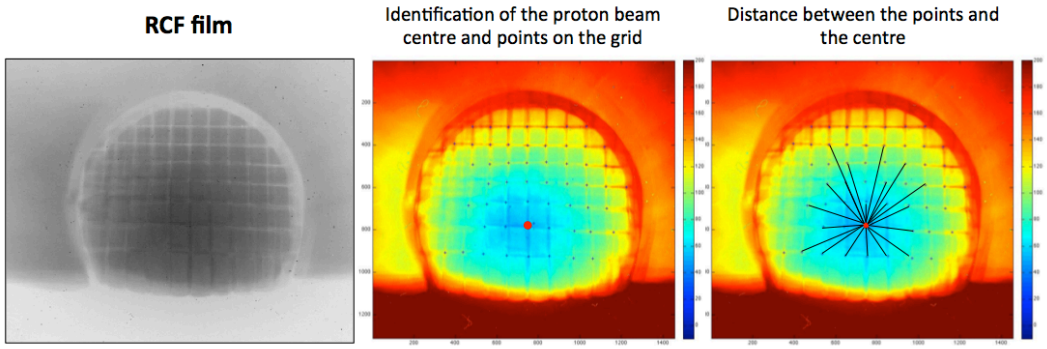

Figure 3.37 *Example of RCF image analysis (Shot #34 – 2nd RCF layer).*

[3] The weight is a function of $1/d$ where d is the distance from the centre $(0; 0)$.

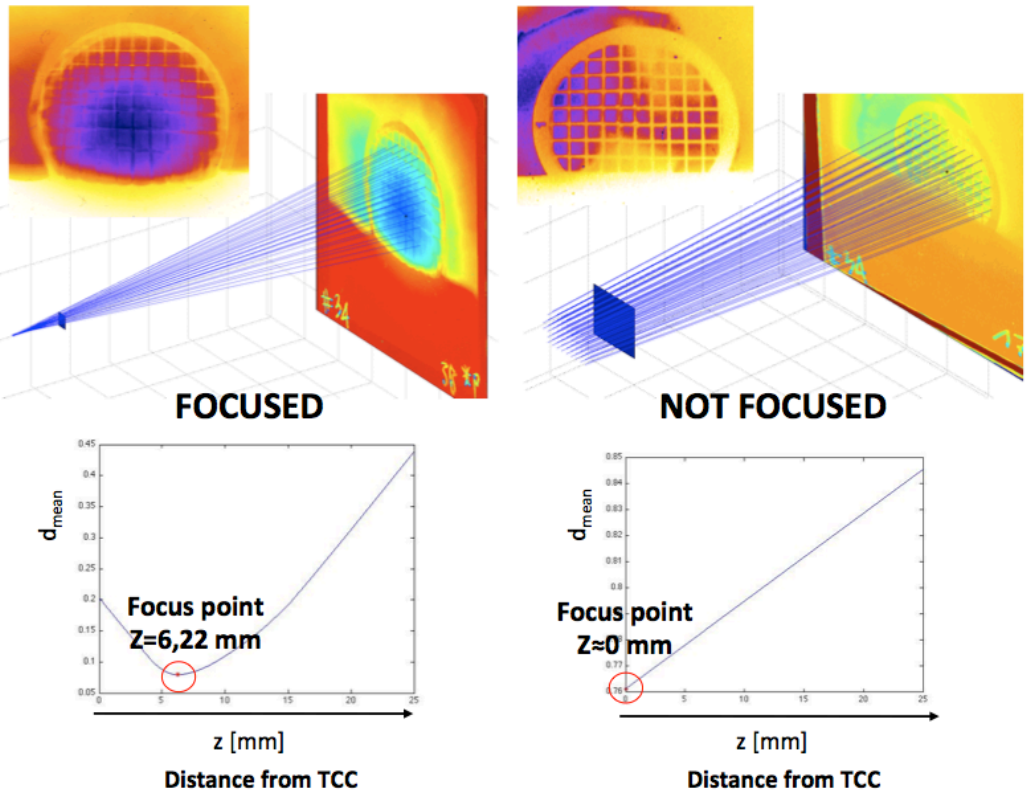

Figure 3.38 *(Top) Ray-tracing from the grid projection on the RCF to the real position of the grid. (Below) Plot of the d_{mean} as a function of the distance z from TCC (z=0).*

Analyzing the projection of the grid on a RCF film, three possible cases were identified:

1. The grid projection was not deformed; the d_{mean} position was around the zero point (TCC and primary target position).
2. The grid projection was only slightly deformed; the d_{mean} position was inside the cylinder.
3. The grid projection was very deformed; the d_{mean} position was outside the cylinder.

Case (1) corresponds to proton energies that have not been affected by the action of the lens. These protons leave the cylinder before the arrival of the trigger pulse. Case (2) corresponds to proton energies that have been partially affected. In this case, as represented in Figure 3.39 (green), the divergence of the proton beam is modified but not enough to focus the protons after the cylinder. Case (3) corresponds to protons that were actually focused.

Following these criteria, the shots presented in Table 3.1 have been analyzed. The results of the analysis are presented in Figure 3.40 for a time-delay of 90 ps; Figure 3.41 for a time-delay of 63 ps and Figure 3.42 for a time-delay of 50 ps.

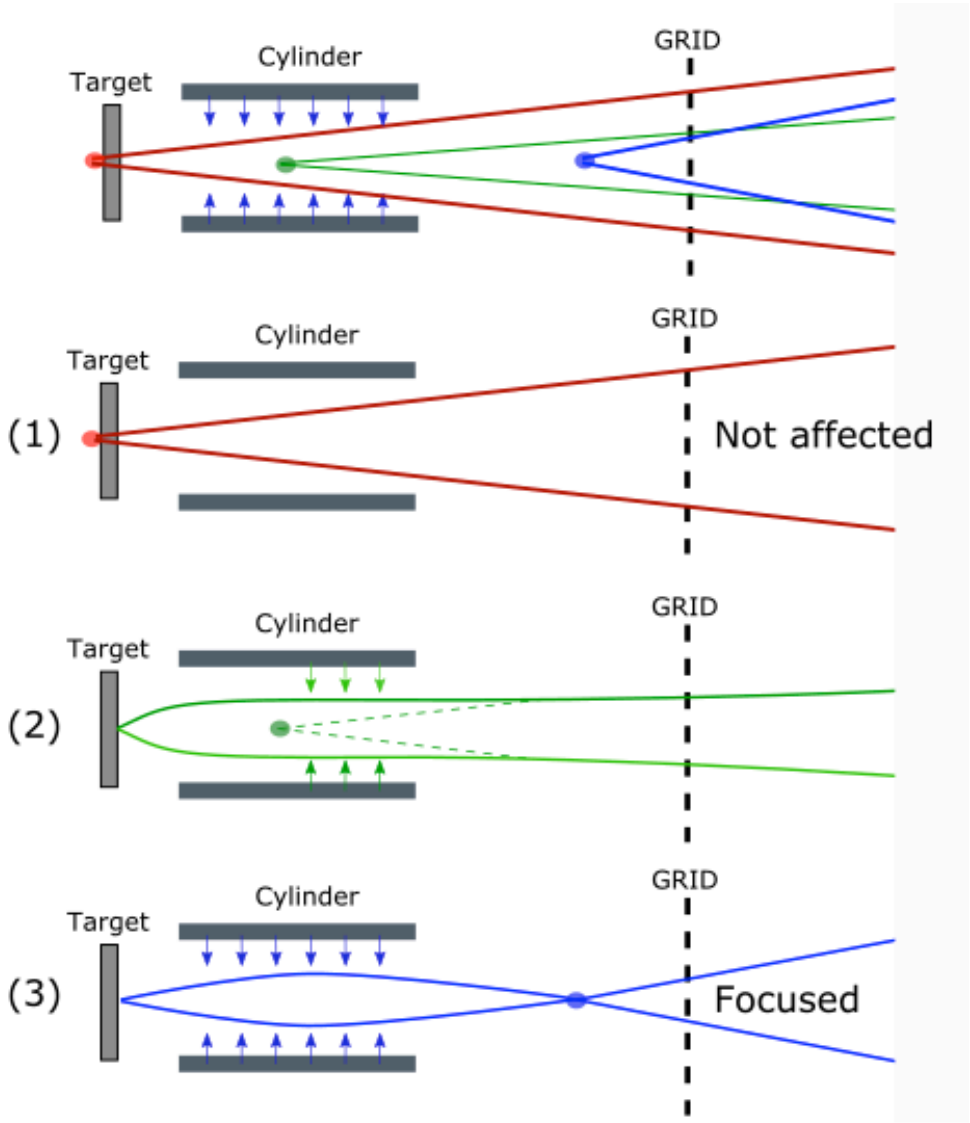

Figure 3.39 *Scheme of the possible effects of the lens on the protons. (1 – red) The protons with high energy pass thought the lens before it is triggered and are not affected by the transient electric field. (2 – green) The protons that only partially feel the electric field are collimated. (3 – blue) The protons that fell all the duration of electric field are focused.*

As shown in the three space vs. time graphs of Figure 3.36, only in the $\Delta t = 90\ ps$ case part of the proton beam (all energies higher than 10.4 MeV) was already outside the cylinder when it has been triggered. This is clearly shown in Figure 3.38, where the yellow zone represents the proton energies that have been influenced by the electric field inside the lens. The 80% zone indicates proton energies that have been affected for at least 80% of the duration of the lens action. The 20% zone represents the proton energies that were already close to the end of the cylinder when it was triggered, therefore they go out from the lens before it switched off. They were influenced by the electric field only for 20% of its duration.

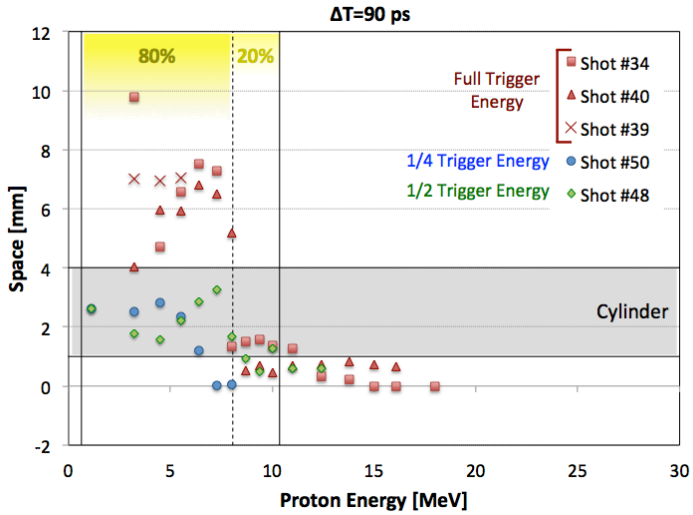

Figure 3.40 *Focus position for protons of different energies. Position 0 corresponds to the location of the protons sources (the PET target). Delay between the main pulse and the trigger pulse $\Delta t = 90\ ps$. (Red) Full trigger laser pulse energy (33 J). (Green) Half of the trigger pulse energy (16 J). (Blue) Quarter of the full trigger pulse energy (8 J).*

As already said, for the time delay of 90 ps, we have also varied the energy of the trigger pulse. In Figure 3.40, the full energy case is represented with the red points, the half-energy case with the green points, and the quarter-of-energy case with the blue points.

In the full-energy trigger pulse case, the analysis shows that we were able to focus proton energies affected at least for the 80% of the electric field duration. The focus points of the different energies varied in a range of a few mm, between 5 and 8 mm. The protons that have spent only 20% of the electric field duration inside the cylinder were partially focused. The high-energy protons exiting the lens before it was triggered were not affected at all.

Decreasing the energy of the trigger pulse, we were no longer able to focus the protons.

The analysis of the results obtained at $\Delta t = 63\ ps$ and $\Delta t = 50\ ps$ (in Figure 3.41 and Figure 3.42 respectively) shows that in these cases, we were able to focus the whole range of proton energies.

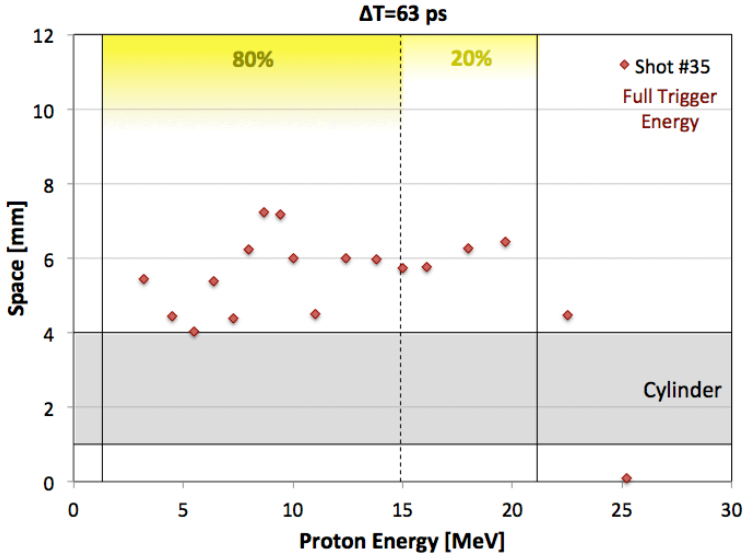

Figure 3.41 *Focus position for protons of different energies. Position 0 corresponds to the location of the protons source. Delay between the main pulse and the trigger pulse* $\Delta t = 63\ ps$.

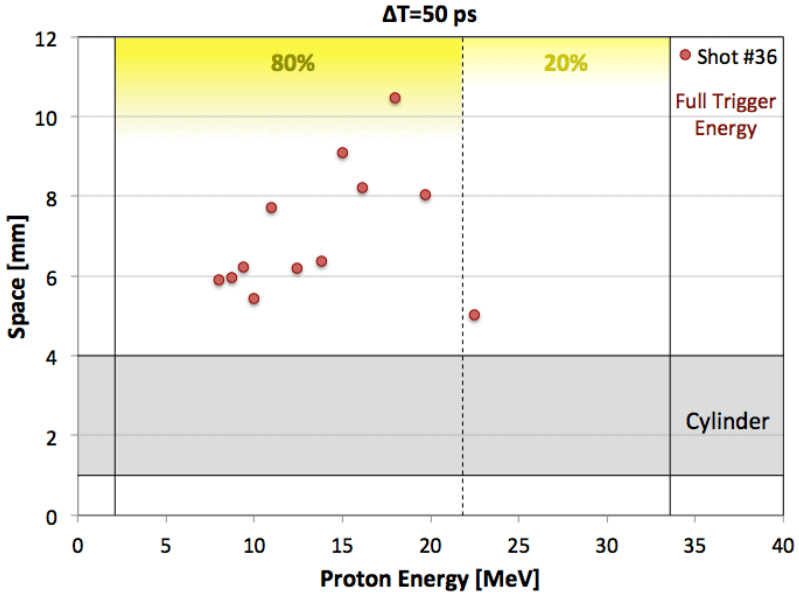

Figure 3.42 *Focus position for protons of different energies. Position 0 corresponds to the location of the protons source. Delay between the main pulse and the trigger pulse* $\Delta t = 50\ ps$.

3.2.2 SET-UP 2: Selection in energy of part of the focused protons energy spectrum

Primary Target:	PET (23 μm of thickness coated with 14 nm Al)
Cylinder:	Al (3 ± 0.1 mm length; 940 μm external diameter; 780 μm internal diameter)
Grid:	-
Pinhole:	Plastic HDPE
Secondary Target:	-
Beams:	Main and Trigger Beam
Diagnostics:	RCF stack for proton detection
	nToF for gamma and background detection

In the previous section, I presented the results of the focusing study that have shown that when we obtained the focusing of the proton beam, the focus point was located a few millimeters after the end of the cylinder. Moreover, the distances between the focus points of the different proton energies were in the order of millimeters.

Thus, the spatial separation between the focus points of different proton energies was relatively small while the range of energies actually focused was large. Therefore the pinhole alone could not allow a real energy selection of the protons. Indeed, it was not possible to discriminate with certainty between a focus position and another.

In order to achieve a possible energy selection of the protons, we chose to increase the time-delay between the main pulse and the trigger pulse up to 160 ps. In this way, as shown in Figure 3.43, the range of proton energies inside the cylinder while the electric field was acting was narrower. Only protons with energies between 0.2 MeV and 3.28 MeV were inside the cylinder when it was triggered. And only the energies between 0.2 MeV and 2.33 MeV stayed inside the cylinder for at least 80% of the electric field duration. Therefore, this choice of time-delay allowed us to focus only energies up to around 3 MeV. The choice was motivated by the maximum of the cross-section of the $^{7}Li(p,n)^{7}Be$ reaction being located at 2.2 MeV (see Figure 3.30).

Thanks to the focusing study shots described in the previous section, we observed that the focus position of the proton energies focused by the lens was a few millimeters after the end of the cylinder. Therefore, we positioned a pinhole as close as possible to the focus point position (10 mm from the primary target, i.e. 6 mm after the end of the cylinder).

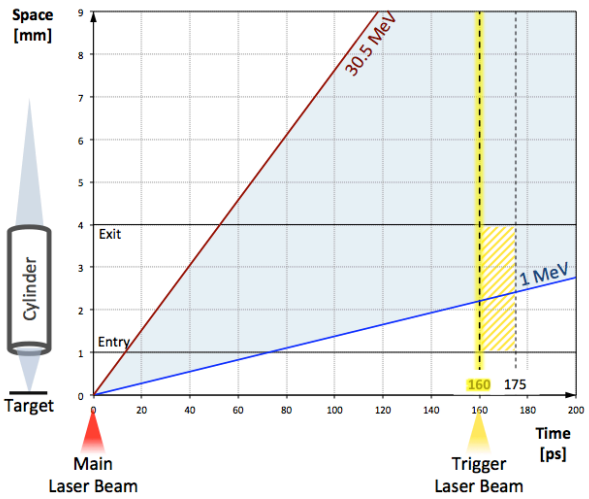

Figure 3.43 *Space vs. time graph of the protons for* $\Delta t = 160\ ps$.

We observed the resulting signal after the pinhole with an RCF stack. Since we were interested in the very low energy part of the proton spectrum, we divided the first RCF of the stack into four quarters putting filters of different thicknesses in front of each quarter (39 μm Al, 52 μm Al, 62 μm Al, 82 μm Al), as shown in Figure 3.44. This allowed us to see slightly different proton energies in each quarter, as shown in Figure 3.45.

At the beginning, we had planned to use metallic pinholes with a very good hole precision. Unfortunately, during the experiment, we observed that the use of this kind of pinhole generates a very large background noise on the nToF detector. Therefore, we chose to manufacture a plastic pinhole (HPDE material) in the workshop of the facility. We obtained a pinhole diameter of around 300 μm.

The RCF stack of Figure 3.45 shows that only protons having energies between 2 and 3 MeV generate a signal larger than the hole of pinhole projection. This means that only these energies were focused at the pinhole position. For all the other energies only the hole projection is visible.

This allowed us to conclude that using this set-up we were able to select in particular protons having energies up to 3 MeV.

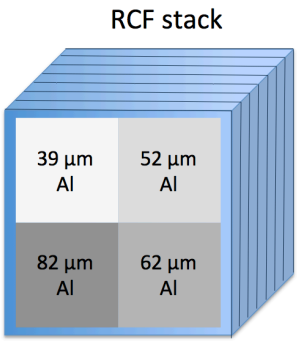

Figure 3.44 *RCF stack with different filter thickness in front of each quarter.*

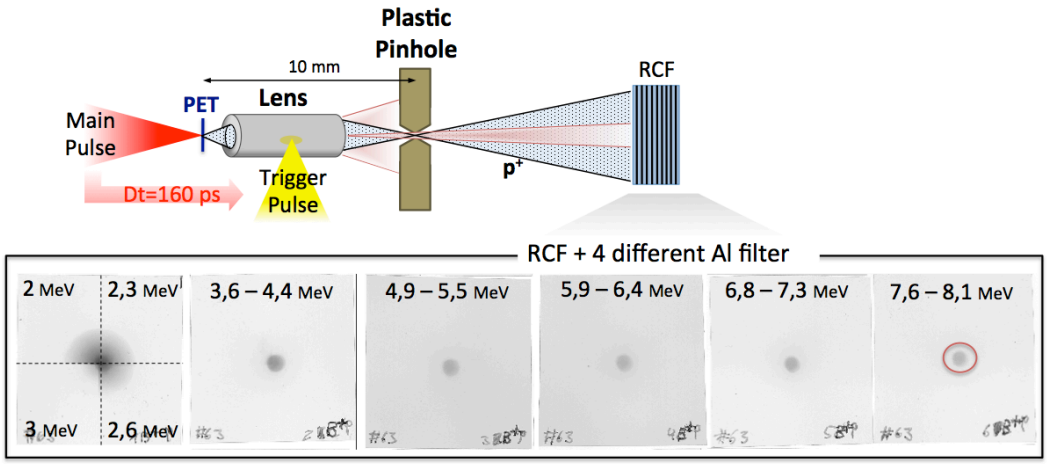

Figure 3.45 *(Top) Set-up of the proton selection using the pinhole. (Below) Proton signal on the RCF stack positioned after the pinhole.*

3.2.3 SET-UP 3: Production of neutrons using a LiF catcher and a full proton energy spectrum

Primary Target:	PET (23 μm of thickness coated with 14 nm Al)
Cylinder:	-
Grid:	-
Pinhole:	-
Secondary Target:	LiF
Beams:	Only Main Beam
Diagnostics:	CR-39, Bubble Detectors, Activation Sample, nToF Detectors

Similarly to the neutron production carried out during the ELFIE experiment and discussed in § 3.1.1, during this second campaign we performed a series of shots in which the full proton spectrum was impinging on the catcher. In this configuration we only used the main beam. Therefore, the set-up was only composed of the primary target and the LiF catcher. The LiF was a disk of 1 inch in diameter and 2 mm in thickness located 20 mm away from the primary target (the whole proton beam hits the LiF catcher).

Since the shock due to the impinging proton beam could damage the catcher, the LiF disk was glued on an aluminum support in order to avoid the dispersion of possible broken pieces inside the vacuum chamber.

To measure the neutron yield, we implemented a variety of diagnostics. We used both CR-39 and bubble detectors, as during the ELFIE campaign (§ 3.1.1). Moreover, a fruitful collaboration with the CENBG group and the *Lower Background Facility* of the LLNL allowed us to test activation diagnostics and the direct measurement of the neutron generation by measuring the amount of residual ^{7}Be produced in the LiF slab. Neutron time-of-flight (nToF) detectors were used as well to provide a measurement of the neutron spectrum at multiple angles.

Neutron production measurement via residuals in LiF

As detailed in § 2.2.2.4, it is possible to obtain information on the produced neutrons by studying the activation of the LIF catcher. Indeed, each reaction that takes place inside the catcher generates a residual. An estimation of the total neutron production can be inferred from the measurement of the activity of the residual isotopes.

At the beginning, we considered the neutrons to be generated from the catcher only by the following reactions:

$$^{7}Li + p \longrightarrow {}^{7}Be + n, \tag{3.29}$$

$$^{6}Li + p \longrightarrow {}^{6}Be + n, \tag{3.30}$$

$$^{19}F + p \longrightarrow {}^{19}Ne + n. \tag{3.31}$$

And, as said in § 2.2.2.4, among these reactions only the ^{7}Be residual had a long half-life of 53.22 days that allowed us to detect this isotope after the shot. The half-lives of both ^{6}Be and ^{19}Ne are shorter than 20 seconds, and thus too short to allow measurements ex-situ due to the long time (~ 10 min) needed to vent the chamber.

The decay of the *LiF* catcher after the shot and the activation spectrum measured with the germanium detector are presented in Figure 3.46. The gamma emission from the sample has been detected using the germanium detector of the low background facility of the Lawrence Livermore National Laboratory (LLNL).

Due to the high maximum proton energy achieved, the reactions (3.29), (3.30) and (3.31) were not the only possible ones.

During the experiment we also observed the reaction:

$$^{19}F + p \longrightarrow {}^{18}Ne + 2n. \tag{3.32}$$

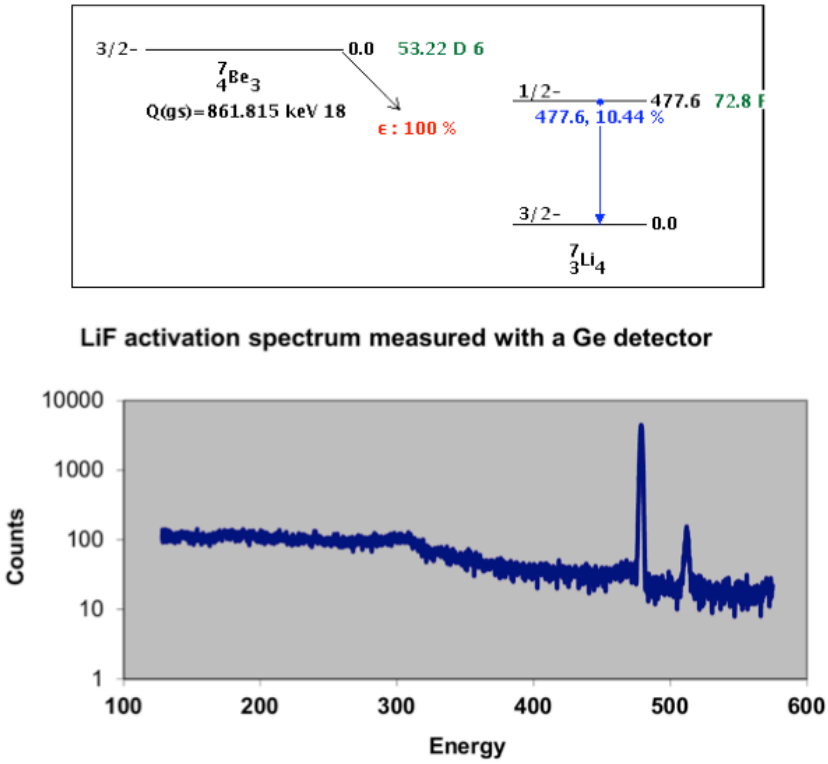

Figure 3.46 *(Top) Scheme of decay of the ^{7}Be residual. (Below) Example of the activation spectrum measured with the germanium detector. The higher peak (477 keV) is due to the ^{7}Be decay and the lower peak (511 keV) is due to the β^{+} decay of the ^{18}F.*

This reaction has a threshold of around 16.5 MeV. The generated residual is the ^{18}Ne that decays as:

$$^{18}_{10}Ne \xrightarrow{1.667\ s} {}^{18}_{9}F + e^{+} + \nu_e \quad followed\ by$$
$$^{18}_{9}F \xrightarrow{109.77\ m} {}^{18}_{8}O + e^{+} + \nu_e\ . \tag{2.33}$$

Indeed, our CENBG collaborators had measured the β^{+} decay of the $^{18}_{9}F$ produced by the decay chain of ^{18}Ne[4] (see second peak of Figure 3.46).

We analysed the activity of two shots obtaining the following values:

	Activity [Bq]	Total Neutron Number [n/shot]	Total Neutron Number [n/sr/shot]
Shot #25	230	1.5×10^{9}	1.2×10^{8}
Shot #42	291	1.9×10^{9}	1.5×10^{8}

[4] The decay of the ^{18}Ne is too short to be measured.

Therefore, during this campaign we measured a number of neutrons per steradian[5] two orders of magnitude larger than in the first campaign.

In order to check the validity of our experimental measurements, we used Monte-Carlo simulations to estimate the total number of neutrons produced by the measured full proton spectrum of Figure 3.33 and Figure 3.34. We obtained a total neutron number of 10^9 and an activity of 300 Bq, which is consistent with the activation measurement of the ^7Be residual.

Neutron measurements via activation

If the direct measurement of the activation of the LiF catcher gives information about the total amount of neutrons produced, the measurement of the activation of sample materials irradiated by the neutron source is an indirect method to obtain information on the total neutron yield. However, it can yield information regarding the neutron spectrum. This is due to the energy dependence of the cross-sections in different materials (see Figure 3.48). Choosing the appropriate materials, it is possible to cover different zones of the spectrum.

We studied the activation of various materials, in particular the isotopes: ^{115}In, ^{27}Al, ^{56}Fe. Indeed, we put a stack of the activation materials after the LiF catcher. The stack was composed of:

- An ***indium*** cylindrical puck (thickness =3 mm, radius = 25 mm, ρ = 7.31 g/cm^3).
- A steel slab that we approximate as ***iron*** (thickness =12.5 mm, area = 20x30 mm^2, ρ = 7.87 g/ cm^3).
- An ***aluminium*** cylindrical puck (thickness = 10 mm, radius = 25 mm, ρ= 2.69 g/ cm^3).

At the end of the stack we positioned the CR-39. The stack was placed in the forward direction at 0° from the axis of the proton propagation and at a distance of either 45 or 205 mm from the front of the indium to the LiF (see Figure 3.47).

The possible neutron induced reactions for the three materials used were:

$$^{115}In + n \longrightarrow {}^{115}In^* + n, \tag{3.34}$$

$$^{56}Fe + n \longrightarrow {}^{56}Mn + p, \tag{3.35}$$

$$^{27}Al + n \longrightarrow {}^{27}Mg + p. \tag{3.36}$$

[5] Since the neutron production is not isotropic, this is only a rough estimation.

All the residuals of reactions (3.34), (3.35) and (3.36) decay with β^- mode (see Table 3.3), with the cross-sections shown in Figure 3.48.

The counting of the β^- decays of the residuals has been carried out with the NATALIE system, and the results are presented in Table 3.4.

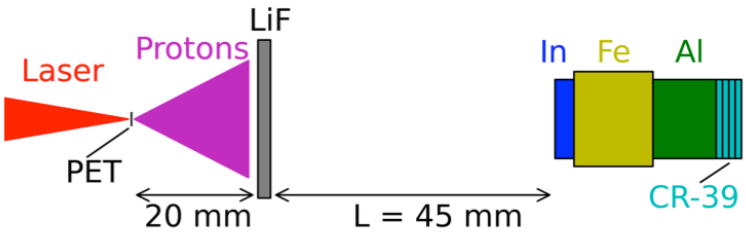

Figure 3.47 *Set-up of the activation stack.*

Residual	ΔE [MeV]	$T_{1/2}$	Decay Mode	Gamma Energy [keV]
$^{115}In^*$	−89.2001	4.486 h	β^-: 100%	336
^{56}Mn	−56.9108	2.379 m	β^-: 100%	566
^{27}Mg	−14.5866	9.46 m	β^-: 100%	840

Table 3.3 *Residuals of the activation materials used during the experiment.*

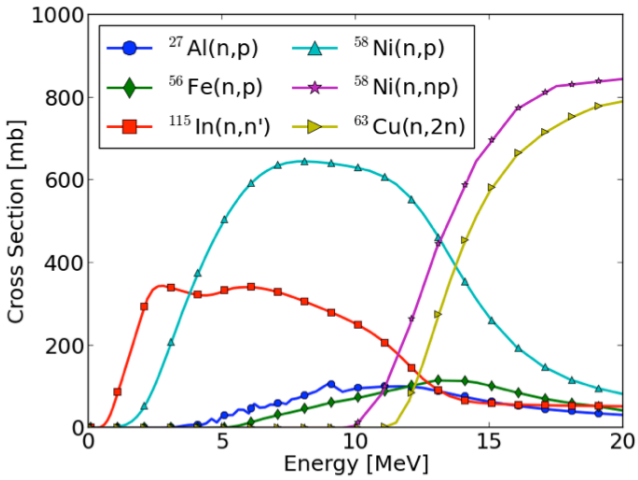

Figure 3.48 *Cross-sections of the activation materials used for neutron induced reactions.*

Shot	Element	Distance [mm]	A(0) [Bq]	N [n]	N/dΩ [n/sr]
Shot #25	Al	220.5	Too Low		
	Fe	208			
	In	205	0.8	1.9×10^{5}	8.1×10^{4}
Shot #42	Al	60.5	45	3.7×10^{4}	
	Fe	48	3.42	4.6×10^{4}	1.9×10^{6}
	In	45	7.52	1.8×10^{5}	1.3×10^{7}

Table 3.4 *Results of the activation measurements. A(0) is the activity, N the number of the activated residuals and N/dΩ the activated residuals per solid angle.*

As shown in Figure 3.47, a stack of 4 CR-39 pieces was also placed after the activation stack at 0°. Other stacks of CR-39 were positioned at 18°, 90° and 138°. For each stack only the 2nd, 3rd and 4th pieces were analyzed, with a procedure similar to the one described in § 3.1.1. The results obtained are presented in Table 3.5.

	Angle [deg]	Distance [mm]	Measurements [track]	Measurements/dΩ [track/sr]
Shot #25	0°	232	214	2.7×10^{5}
	18°	232	86	1.1×10^{5}
	90°	277	12	2.1×10^{4}
	138°	151	88	5.9×10^{4}
Shot #42	0°	72	327	3.9×10^{4}
	18°	–		
	90°	277	71	1.3×10^{5}
	138°	–		

Table 3.5 *Experimental results from the CR-39 stacks. The tracks are counted over 25 photographs of 0.57 mm^2 area on 3 pieces stacked behind each other.*

The results of the activation data analysis and of the CR-39 stack analysis have been compared with the neutron energy spectrum obtained with a MCNP6 simulation. The input of the Monte-Carlo simulation was the full proton spectrum of Figure 3.33 and 3.34.

The simulated neutron spectrum has been normalized by the number of neutrons measured from the ^{7}Be residual [Higginson *et al.*, in preparation]. The average energy of neutrons contributing to the tracks formation in CR-39 or to the activation in the samples was retrieved from the simulation.

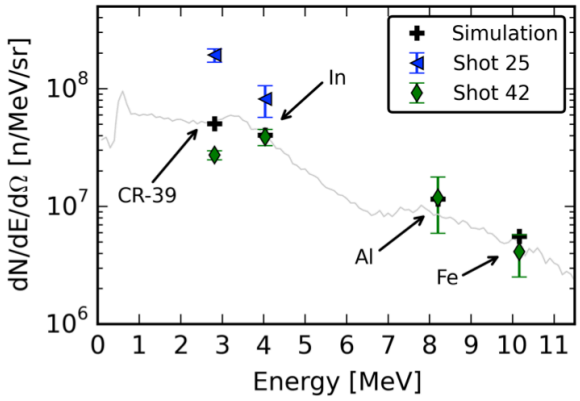

Figure 3.49 *Neutron energy spectrum at 0°. The gray line shows the spectrum determined from the MCNP6 simulations which has been normalized by the number of neutrons inferred from the ^{7}Be residual activity. The different markers represent the average energies and the neutron fluences inferred from the activation material and CR-39 analysis [Higginson* et *al., in preparation].*

In Figure 3.49, the simulated neutron energy spectrum at 0° is compared with neutron fluences at different energies obtained from the activation data and the CR-39. We see that the agreement is good, which therefore validates each of these methods in characterizing the neutron source.

3.2.4 SET-UP 4: Production of neutrons using a LiF catcher and a selected proton energy spectrum

Primary Target:	PET (23 μm of thickness coated with 14 nm Al)
Cylinder:	Al (3 ± 0.1 mm length; 940 μm external diameter; 780 μm internal diameter)
Grid:	-
Pinhole:	Plastic HDPE
Secondary Target:	LiF (2 mm thickness)
Beams:	Main and Trigger Beam
Diagnostics:	CR-39, Bubble Detectors, Activation Sample, nToF detection

Using the set-up discussed in § 3.2.3, we obtained a selection of the protons up to 3 MeV. We decided to use this modified proton spectrum to generate neutrons as well and characterize the output neutrons.

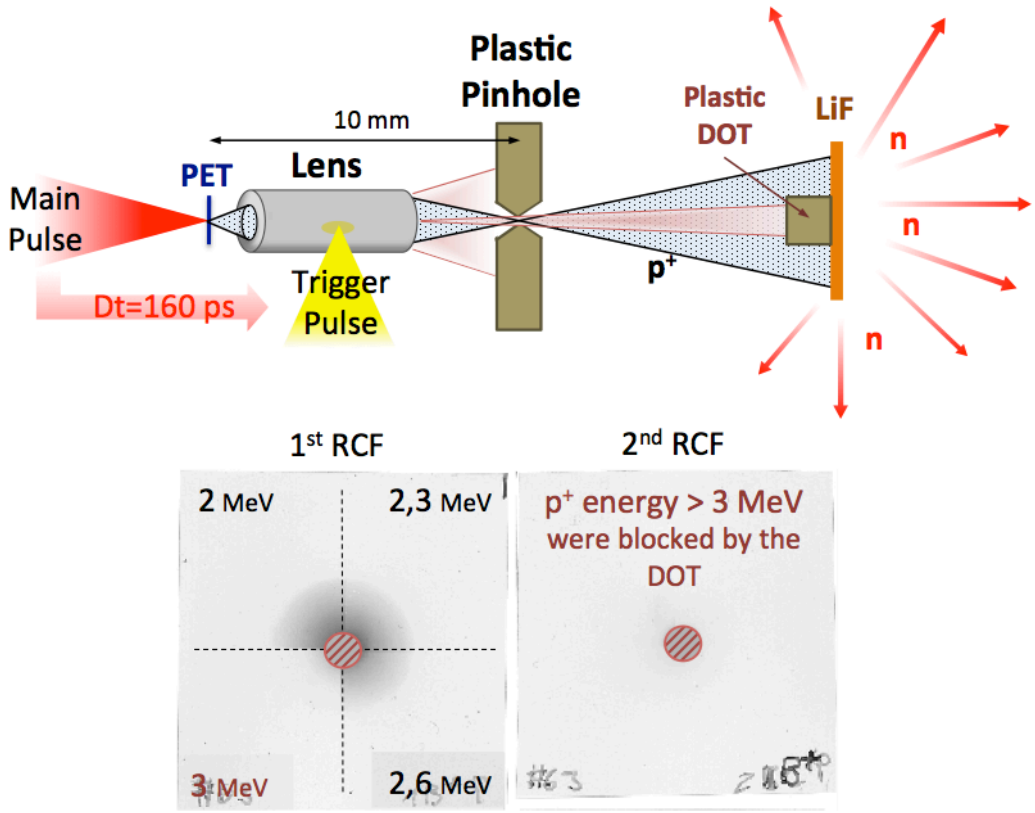

Figure 3.50 *(Top) Set-up of neutron generation using the pinhole and the plastic dot in front of the LiF. (Below) The central part of the proton beam is blocked by the dot. The blocked zone is shown on the first and second RCF stack of Figure 3.45 (SET-UP 2).*

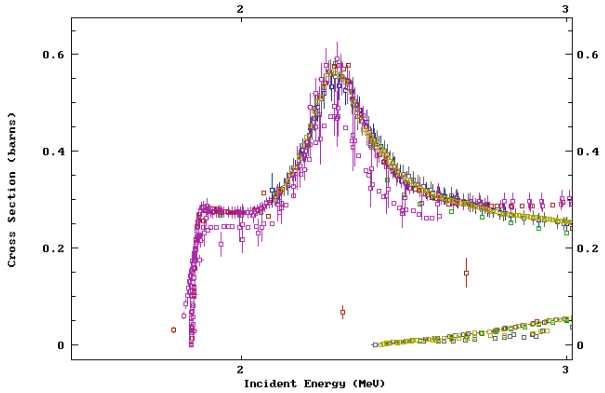

Figure 3.51 *$^{7}Li\ (p,n)^{7}Be$ cross section in the proton energy range between 1.88 MeV and 3 MeV [Parsons* et *Gale 2015].*

Since the protons with energies higher than 3 MeV were still able to pass through the hole of the pinhole, we decided to modify the set-up of the LiF, putting a plastic dot in the center of our LiF catcher, as shown in Figure 3.50 (top). In this way, we wanted to avoid that even a small part of protons with energies higher than 3 MeV were hitting the catcher, see Figure 3.50 (below).

We should obtain in this way neutrons due to protons with energies between the $^{7}Li\ (p,n)^{7}Be$ reaction threshold of 1.88 MeV and 3 MeV (see cross-section in Figure 3.51). At the same time we could avoid all the other reactions ($^{6}Li\ (p,n)^{6}Be$; $^{19}F\ (p,n)^{19}Ne$; etc.) that have a threshold higher than 3 MeV. The downside of this choice was that we drastically decreased the number of protons that were impinging on the LiF catcher. As discussed in § 3.2.3, in the case of a full proton spectrum impinging on the catcher we measured around $10^{9}\ n/shot$.

As will be discussed in the next section, the data from the nToF detectors are not yet fully analyzed. So we cannot give in this manuscript a quantitative description of the neutron spectrum measured by the nToF detectors. Nevertheless, a qualitative comparison between the neutron spectrum of set-up 3 (obtained using the full proton spectrum, see § 3.2.3) and the neutron spectrum of set-up 4 described in this section (obtained using the selected proton spectrum) can be made observing Figure 3.52. We can see a trend, as in the ELFIE experiment, in reducing the temporal width of the nTOF signal when energy-selecting protons. However, as discussed in the following section, issues remain in the analysis.

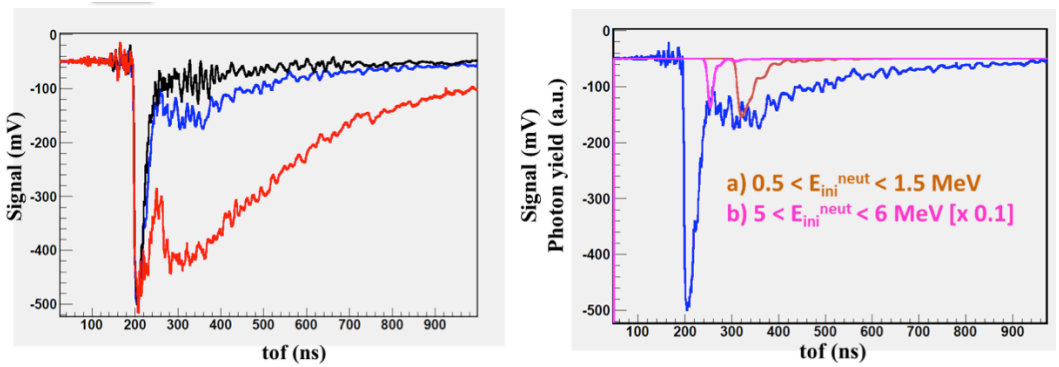

Figure 3.52 *(Left) Experimental data obtained from one detector with the full energy spectrum of accelerated protons impinging on the LiF target (set-up 3 - red signal), with energy selected protons on the same LiF target (set-up 4 - blue signal) and without LiF target (black signal). (Right) The experimental signal in blue (set-up 4) is compared with simulations of photon yield in the scintillator for incident neutrons with energies in the range [0.5; 1.5] MeV (orange line) and [5; 6] MeV (pink line).*

3.2.5 Open Problems for the Data Analysis

Proton

We had planned to measure the proton spectrum using the activation technique (as described in § 2.2.1.2) applied to a stack composed of various types of RCF (HD-810, HD-V2, EBT2), Ni foils and Cu foils. The stack was composed of 35 layers, while the NATALIE system only includes 16 counting stations. Therefore, we measured several (mostly consecutive) layers together. The layers measured together were not always of the same material or of the same type of RCF and it was the first time that NATALIE was used in that way. The unfolding program used up to that moment was not suitable anymore to deduce the incident proton energy distribution from the activation measurements.

Furthermore, it was also the first time that NATALIE was used to characterize protons with a maximum cut-off energy as high as 30.5 MeV (it was around 16 MeV in previous studies). Due to this high maximum cut-off energy, the number of possible reactions inside the stack foils was larger compared to previous studies. These possible reactions are presented in Table 3.6. In order to analyze and estimate the induced radioactivity, these additional reactions must be taken into account.

	Isotope	NA	Reaction	Threshold (MeV)	σ_{max} (mb)	Product	$T_{1/2}$ (min)
RCF	^{18}O	0.2 %	(p,n)	2.57	400	^{18}F	109.77
	^{16}O	99.6 %	(p,a)	5.55	180	^{13}N	9.96
	^{14}N	99.6 %	(p,a)	3.13	240	^{11}C	20.33
	^{13}C	1.1 %	(p,n)	3.24	196	^{13}N	9.96
	^{12}C	98.9 %	(p,pn)	20.29	92	^{11}C	20.33
			(p,γ)	0	≈1	^{13}N	9.96
Copper	^{65}Cu	30.85 %	(p,pn)	10.06	529	^{64}Cu	762,06
			(p,p3n)	29.12	160	^{62}Cu	9.67
			(p,3n)	22.32	165	^{63}Zn	38.47
			(p,4n)	29.12	≈1	^{62}Zn	551,16
			(p,p4n)	38.144	≈1	^{61}Cu	199,98
	^{63}Cu	69.1 %	(p,n)	4.22	546	^{63}Zn	38.47
			(p,pn)	11.03	584	^{62}Cu	9.67
			(p,2n)	13.47	124	^{62}Zn	551,16
			(p,p2n)	20.05	147	^{61}Cu	199,98

Table 3.6 *Possible reactions inside the foils of the stack during the TITAN campaign. The highlighted reactions are the ones taken into account in previous studies.*

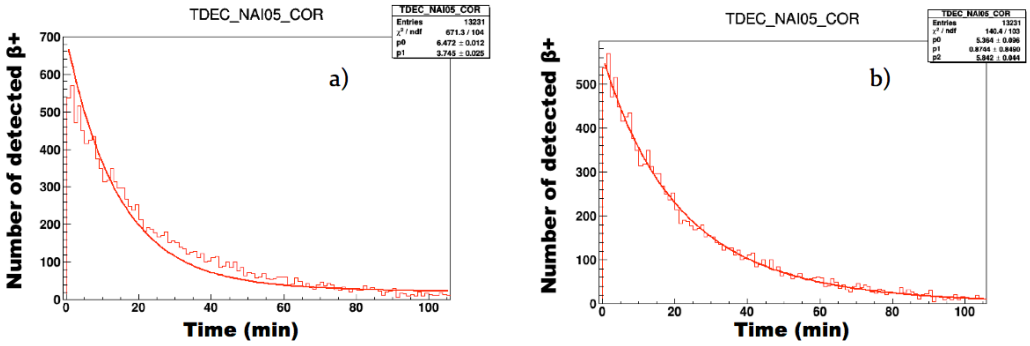

Figure 3.53 *Radioactive decay measurement of a RCF film taking into account a) only ^{13}N and ^{18}F radioisotopes and b) ^{13}N, ^{18}F and ^{11}C radioisotopes.*

For example, in the past studies, the analysis of the proton-induced activation in the RCF only took into account the creation of two radioisotopes: ^{13}N and ^{18}F [Plaisir thesis 2010]. But analyzing the results of the TITAN campaign, it appeared that this was not sufficient to reproduce the experimental evolution of the β^+ counting versus time. In this case, it has been necessary to also take into account the ^{11}C radioisotope, leading to a much better fit of the results (see Figure 3.53).

As evidenced in Table 3.6, in past experiments where the maximum proton cut-off energy was around 16 MeV, there were only 4 possible reactions for the RCF and 1 for the copper foils. On the contrary, for the TITAN experiment where the cut-off energy was larger, we may have to consider 6 reactions for the RCF and 9 reactions for the copper foils. The corresponding cross sections associated to the 6 RCF reactions are shown in Figure 3.54.

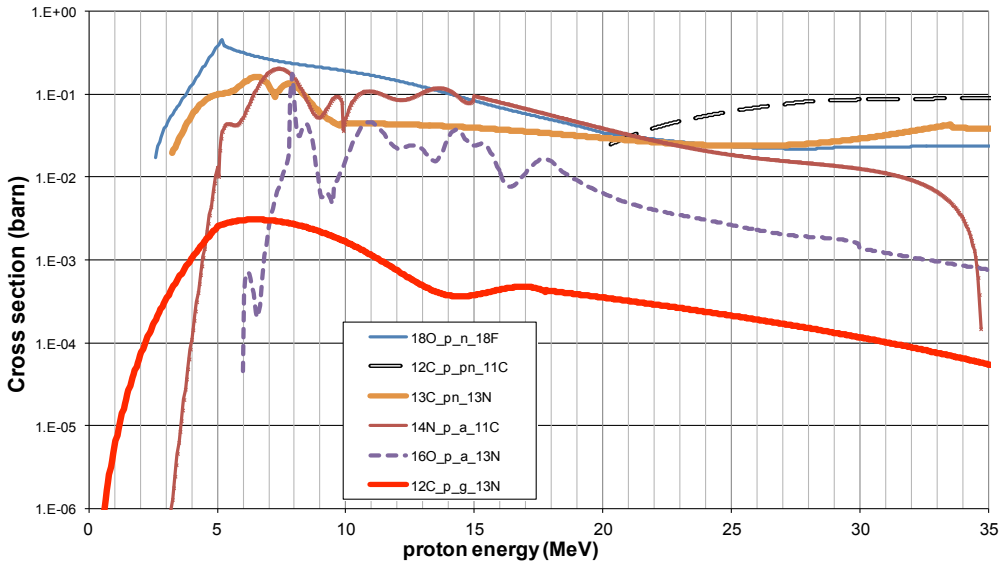

Figure 3.54 *Cross sections of involved nuclear reactions when a RCF is activated by protons [ENDF].*

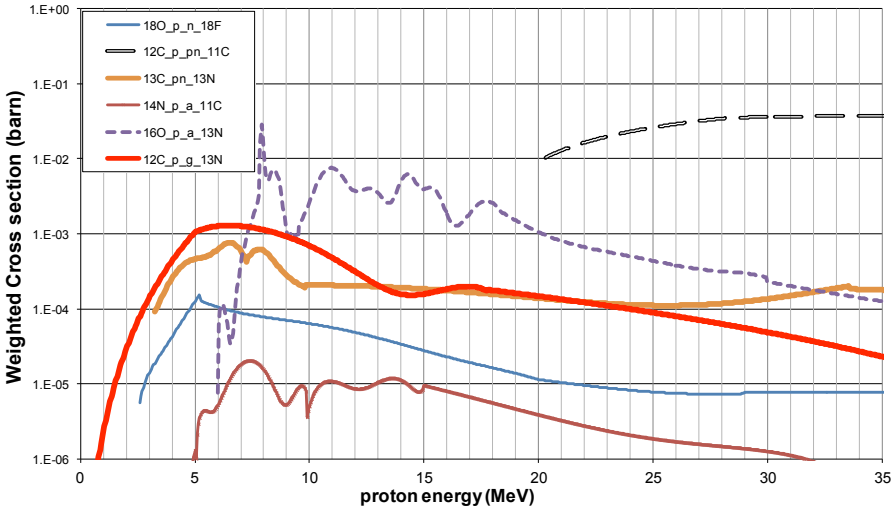

Figure 3.55 *Cross sections of the involved nuclear reactions multiplied by the fraction of the target isotope present in a RCF film.*

To really estimate the importance of each nuclear reaction, one also has to take into account the composition of the analyzed layer. For example, in the case of EBT radiochromic films, even if the nuclear reaction on ^{14}N has a high cross section, the proportion of nitrogen atoms in a EBT film is only 0.01% so that this reaction does not significantly influence the results. In order to obtain a "weighted cross sections", the cross section of each reaction on different radioisotopes must be multiplied by their proportion in the film (see Figure 3.55).

Observing the figure, the energy domain of the protons can be divided in three regions:

- $E_p \lesssim 7\ MeV$: The ^{12}C(p,γ)^{13}N and ^{13}C(p,n)^{13}N reactions are dominant.
- $7\ MeV \lesssim E_p \lesssim 20\ MeV$: The reaction ^{16}O(p,α)^{13}N gives most of the information about the proton energy distribution.
- $E_p \gtrsim 20\ MeV$: The ^{12}C(p,pn)^{11}C reaction is dominant.

The reactions leading to the emission of several ejectiles are not so commonly studied in nuclear physics. That's why we cannot find their cross sections in a standard nuclear data base such as [EXFOR]. We thus had to perform a deep bibliographic study to find the measured nuclear cross sections in some articles of the 1960's and 1970's.

For all these reasons, the unfolding of the data has been harder than expected and the required deep modifications of the unfolding program are still in progress by our collaborators at CENBG. Hence, all the shots have not been yet analyzed. Nevertheless, this experiment led to an extension of the working domain in nuclear analysis, and it revealed the necessity to take more nuclear reactions into account in order to get a more precise determination of the proton energy spectrum.

Neutron

As previously described, the detection of the neutrons was done using activation measurements, bubble detectors and CR-39. We have also used the time of flight technique. We put 11 plastic scintillators BC-400 (with size of $4\times4\times12\ cm^3$) coupled to type XP2972 photomultiplier tubes at different angles according to the proton beam direction. Since the scintillators respond not only to neutrons, but also to X-rays and γ-rays, a shielding was necessary, as in the case of the ELFIE experiment. Otherwise, the strong flash that follows the interaction of the laser beam with the primary target would saturate the detectors and they would not be active at the time of arrival of neutrons. In order to minimize the detection of X-rays and γ-rays, lead bricks were placed around the scintillators. The lead shielding was set principally in the direction towards the experimental chamber, with thicknesses ranging between 20 cm and 40 cm for the different detectors. A schematic representation of the nToF set-up is presented in Figure 3.56.

Knowing the response of the BC-400 scintillator, the amplitude of the experimental signal can be converted to a number of scintillation photons.

The scintillator signals showed a big amount of low energy neutrons (see Figure 3.52). The presence of these neutrons was not expected. Therefore, before to analyze the signals of the different set-ups, we focused our attention to find a possible explanation for this long tail of low energy neutrons.

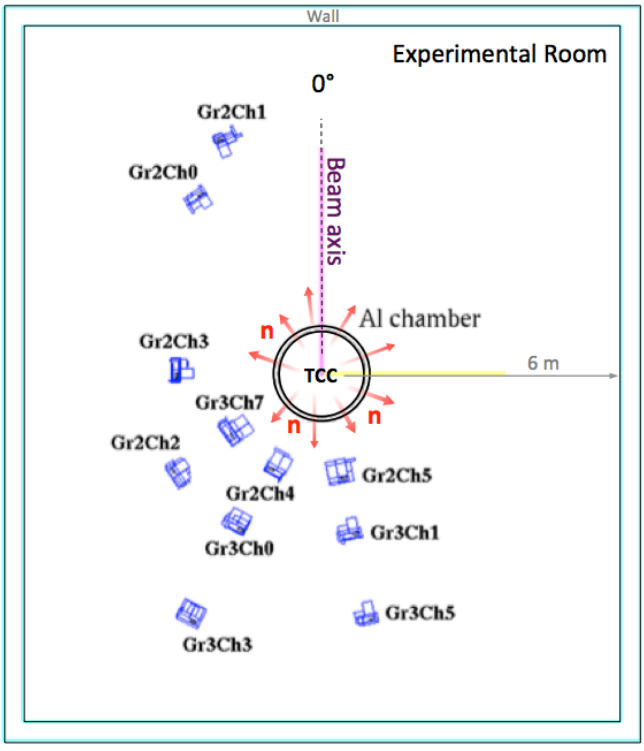

Figure 3.56 *Set-up of the nToF detectors inside the experimental room.*

Two possible explanations can be that either we really generated these low neutrons or a lot of the neutrons were scattered prior detection thus arriving later in time on the scintillators. Both cases correspond to an observed significant number of events at high values of TOF. Another possible explanation of this effect is a saturation of the detector in the intense neutron flux.

A set of Geant4 simulations was performed reproducing the experimental conditions [Kisyov *et al.*, 2015]. The results suggest that most of the neutrons were scattered mainly from the lead shielding. This effect can lead to a shape similar to the experimentally observed one, but a possible saturation of the detectors in the intense neutron flux is also not excluded as a possible explanation. Future studies will shed light on this effect.

3.2.6 Conclusions for the TITAN Experimental Campaign

In the previous sections I showed the principal results we obtained during the second experimental campaign at TITAN. In § 3.2.1, I presented the focusing effect of the lens and how it has been studied using grids. For all the proton energies affected by the electric field at least for the 80% of its duration, we observed a focalization after the lens. The position of the focus point was in a range of few millimeters for all the focused energies. We do not have precise information about the exact dimension of the proton beam at the focus point position. However, thanks to the autoradiography data we can assert that it was smaller than 200 μm.

In § 3.2.2, I showed how we obtained a selection of the proton beam. We increased the time delay between the main laser pulse and the trigger laser pulse up to 160 ps, so that only protons with energies lower than 3 MeV were focused by the lens. We put a plastic pinhole at the focus point position after the cylinder. This way, we blocked the majority of the beam for all the non-focused proton energies. Therefore, we selected in particular the protons having energies up to 3 MeV.

Concerning the neutron production, we used a pitcher-catcher set-up: the full TNSA proton spectrum hit the LiF catcher. We measured the activation of the LiF residuals. We obtained a total number of produced neutrons of the order of 10^9 n/shot, that is two orders of magnitude higher than for the ELFIE campaign. The analysis of activated materials gave us a rough idea of the neutron spectrum characteristics. Using the full proton spectrum we produced neutrons up to about 10 to 20 MeV.

We tested the possibilities to modify the neutron spectrum using the selected proton beam of § 3.2.2.2. A precise and quantitative description of the neutron spectrum can only be done exploiting the nToF data. Since these data must yet be completely understood, the results obtained are not presented in this manuscript.

Chapter 4

Conclusions and Perspectives

In conclusion, I presented in this thesis a study of the effects of a laser-triggered micro lens on a proton beam and an innovative approach to improve the characteristics of a laser driven neutron source.

The first experimental campaign carried out at the ELFIE laser facility has shown the possibility to use the micro lens to collimate over a long distance a usually diverging TNSA proton beam (§ 3.1.2). This feature is very attractive for all the applications that need to exploit the interaction of a laser-plasma accelerated proton beam with a target while avoiding the copious and undesirable radiation resulting from the laser-plasma interaction. Indeed the laser-plasma interaction zone, where the protons are accelerated, is the principal zone where gamma rays and x-rays are generated due to the Bremsstrahlung. Since the proton beam is collimated, a large spatial separation can be managed between the zone where the proton beam is created and the zone where the proton beam hits a possible secondary target. This allows shielding this zone more easily. For instance, all the biological studies of the interaction between a laser-plasma accelerated ion beam and a biological sample (see for example [Bin *et al.*, 2012]) could exploit this set-up, thus avoiding to expose the sample to the gamma and X-rays coming from the laser-plasma interaction zone.

During our experiment, we took advantage of this feature to modify the neutron spectrum generated by the proton beam. The collimation can be used not only to make the proton beam interacting with a secondary target far away from where it is created but also to spatially modify the proton spectrum. This is due to the limited temporal window over which the electric field acts inside the lens. The protons are collimated differently depending on their energy, allowing to spatially filtering the beam (§ 3.1.4).

The second experimental campaign at the TITAN laser facility has evidenced how the proton beam passing through the micro lens can be not only collimated but really focused by increasing the intensity of the laser that triggers the microlens. Further and more detailed investigation should be realized to

understand the behavior of the focusing points and how the emittance of the proton beam is influenced by the lens. Our experimental data show a small spatial separation between the focusing points of the different energies. This has been the principal cause that prevented us to use efficiently the proton energy selection using a pinhole. Performing further experiments to obtain larger distances between the focusing points for the various energies (as shown by [Toncian *et al.*, 2011]) could give the possibility to test the pinhole energy selection concept in better conditions.

Since one of the major difficulties we met during our experiments was to predict precisely the behavior of the lens device, a perspective for the future will be to improve our modeling. Indeed, it will be useful to work out a detailed model of the cylindrical expansion of the plasma inside the cylinder. At the same time, it will be interesting to realize a systematic and thorough experimental investigation of how all the parameters of the cylinder-lens influence the collimating-focusing process. This could be tested by modifying the material, the length, the diameter and the wall thickness of the cylinder. All these studies will give a better understanding of the lens behavior and will lead to a better control of the device.

Concerning neutron production, a narrowing of the neutron spectrum has been clearly showed in the first experimental campaign (§ 3.1.4). On the other hand, the second experimental campaign has showed all the difficulty to detect neutron signals in a high radiation environment like a high-intensity laser facility. The fact that, in this kind of facility, the number of shots per day is nowadays quite limited makes it hard to set all the diagnostic normally used in nuclear physics. All our collaborators in the domain of nuclear physics have faced the same problems. Indeed, they are used to work in a classical accelerator environment where the possibility of collecting data is almost unlimited and where achieving an appropriate shielding for the diagnostics is not an issue. The use of laser-plasma interaction for studies in nuclear physics is relatively recent. Therefore, a lot of new aspects must be taken into account, like the possible saturation of the diagnostics under high flux conditions. For sure, all the upcoming high-intensity and high-repetition-rate laser facilities like Apollon will help to improve the use of high-intensity lasers for nuclear physic experiments, developing the contribution that laser-plasma physics can give to nuclear physics.

Although we faced difficulties, our second experimental campaign has opened interesting perspectives.

The activation diagnostic has showed the presence of interesting uncommon nuclear reactions.

The need to simulate the neutron spectrum achievable with a broad TNSA proton spectrum has evidenced the limits of the known cross sections used inside the MCNP code.

This kind of experiment can also be a test bed for all the diagnostics needed in the future large laser facilities that are under construction like Apollon or ELI.

Finally, concerning the future possible use of a laser neutron source for real applications (as the ones described in § 1.1), we have to take into account that the flux achievable today is still too low. Several experiments designed to improve the neutron flux have already been performed and the maximum flux of 10^{10} n/sr has been obtained in [Roth *et al., 2013*] at the TRIDENT facility of *Los Alamos National Laboratory* (LANL).

In order to increase the neutron flux, practicable approaches can be:

- For the pitcher-catcher configuration: improve the number of protons using other laser ion acceleration mechanisms such as RPA (§ 1.4.2) [Kar *et al.*, 2012] and BOA (§ 1.4.4) [Roth *et al., 2013*].
- For the single thick target case: improve the number of accelerated D^+ ions [Krygier *et al.*, 2015].

Also in that case, new opportunities will be opened by the emergence of new high-intensity and high-repetition-rate laser facilities.

List of publications

Related to the experimental campaigns described in this manuscript

Temporal Narrowing of Neutrons Produced by High-Intensity, Short-Pulse Laser
D. P. Higginson, L. Vassura, M. M. Gugui, F. Negoita, S. Brauckmann, C. Diouf, A. Green, S. Kar, H. Petrascu, S. Sofia, M. Borghesi, O. Willi, and J. Fuchs
Phys. Rev. Lett. 115, 054802 (2015),
http://journals.aps.org/prl/abstract/10.1103/PhysRevLett.115.054802

Time of Flight Measurements for Neutrons, Produced in Reactions, Driven by Laser-Target Interactions at PW level
S. Kisyov, F. Negoita, M. M. Gugiu, D. P. Higginson, L. Vassura, M. Borghesi, L. Bernstein, D. L. Bleuel, B. L. Goldblum, A. Green, F. Hannachi, S. Kar, H. Petrascua, D. Pietreanu, L. Quentin, M. Schroer, M. Tarisien, O. Willi, P. Antici, J. Fuchs
International Conference on Laser Applications at Accelerators, LA3NET 2015

Related to other works

Evidence of resonant surface wave excitation in the relativistic regime through measurements of proton acceleration from grating targets
T. Ceccotti, V. Floquet, A. Sgattoni, A. Bigongiari, O. Klimo, M. Raynaud, C. Riconda, A. Heron, F. Baffigi, L. Labate, L. A. Gizzi, L. Vassura, J. Fuchs, M. Passoni, M. Kveton, F. Novotny, M. Possolt, J. Prokupek, J. Proska, J. Psikal, L. Stolcova, A. Velyhan, M. Bougeard, P. D'Oliveira, O. Tcherbakoff, F. Reau, P. Martin and A. Macchi
Phys. Rev. Lett. 111, 185001 (2013)

Amplification of ultra-short light pulses by ion collective modes in plasmas the use of damage-less optics for high laser intensities
A. Frank, J. Fuchs, L. Lancia, G. Lehmann, J.-R. Marqu`es, G. Mourou, C. Riconda, K.H. Spatschek, T. Toncian, L. Vassura, S. Weber, and O. Willi
Eur. Phys. J. Special Topics 223, 1153–1156 (2014)

Micro-sphere layered targets efficiency in laser driven proton acceleration
V. Floquet, O. Klimo, J. Psikal, A. Velyhan, J. Limpouch, J. Proska, F. Novotny, L. Stolcova, A. Macchi, A. Sgattoni, L. Vassura, L. Labate, F. Baffigi, L. A. Gizzi, Ph. Martin, T. Ceccotti
Journal of Applied Physics 08/2013; 114(8):083305

Laser plasma proton acceleration experiments using foam-covered and grating targets
Sgattoni, T. Ceccotti, V. Floquet, A. Bigongiari, M. Raynaud, C. Riconda, F. Baffigi, L. Labate, L. A. Gizzi, L. Vassura, J. Psikal, L. Stolcova, A. Velyhan, M. Bougeard, P. Martin, I. Prencipe, A. Zani, D. Dellasega, A. Macchi, M. Passoni
Proc SPIE 05/2013

Characterisation of deuterium spectra from laser driven multi-species sources by employing differentially filtered image plate detectors in Thomson spectrometers
Alejo, S. Kar, H. Ahmed, A. G. Krygier, D. Doria, R. Clarke, J. Fernandez, R. R. Freeman,J. Fuchs, A. Green, J. S. Green, D. Jung, A. Kleinschmidt, C. L. S. Lewis, J. T. Morrison, Z. Najmudin, H. Nakamura, G. Nersisyan, P. Norreys, M. Notley, M. Oliver, M. Roth, J. A. Ruiz, L. Vassura, M. Zepf, and M. Borghesi
Review of Scientific Instruments 85, Accepted 7 August 2014

Calibration of Time Of Flight Detectors Using Laser-driven Neutron Source
S.R. Mirfayzi, S. Kar, H. Ahmed, A.G. Krygier, A. Green, A. Alejo, R. Clarke, R.R. Freeman, J. Fuchs, D. Jung, A. Kleinschmidt, J.T. Morrison, Z. Najmudin, H. Nakamura, P. Norreys, M. Oliver, M. Roth, L. Vassura, M. Zepf, M. Borghesi
Rev. Sci. Inst. 86, 073308 (2015); http://dx.doi.org/10.1063/1.492308

Selective Deuterium Ion Acceleration Using the Vulcan PW Laser
A.G. Krygier, J.T. Morrison, S. Kar, H. Ahmed, A. Alejo, R. Clarke, J. Fuchs, A. Green, D. Jung, A. Kleinschmidt, Z. Najmudin, H. Nakamura, G. Nersisyan, P. Norreys, M. Notley, M. Oliver, M. Roth, L. Vassura, M. Zepf, M. Borghesi, and R.R. Freeman
Phys. Plasmas 22, 053102 (2015), http://dx.doi.org/10.1063/1.4919618

Signatures of the self similar regime of strongly-coupled Stimulated Brillouin Scattering for efficient short laser pulse amplification
L. Lancia, A. Giribono, L. Vassura, M. Chiaramello, C. Riconda, S. Weber, A. Castan, A. Chatelain, A. Frank, T. Gangolf, M. Quinn, J. Fuchs, and J.-R. Marques
UNDER REVIEW on Phys. Rev. Lett.

Talk

EMMI Workshop on High Energy Density Plasma Diagnostics at FAIR
GSI Darmstadt Sept.30 – Oct. 02 2013
Narrow band neutron sources produced by ultra intense laser

23ème Congrès SFP Toulouse 2014
13-15 Mai 2014
Improvement of neutron sources produced by ultra intense laser using a laser-triggered micro-lens
L. Vassura, D. P. Higginson, F. Negoita, D. Bleuel, J. A. Green, M. M. Gugiu, F. Hannachi, H. Petrascu, D. Pietreanu, A. M. Schroer, M. Tarisien, S. Kar, M. Borghesi, O. Willi, P. Antici
and J. Fuchs

41st EPS Conferenze on Plasma Physics 2014
Berlin 23-27 June 2014
Improvement of neutron sources produced by ultra intense laser using a laser-triggered micro-lens
L. Vassura, D. P. Higginson, F. Negoita, D. Bleuel, J. A. Green, M. M. Gugiu, F. Hannachi, H. Petrascu, D. Pietreanu, A. M. Schroer, M. Tarisien, S. Kar, M. Borghesi, O. Willi, P. Antici and J. Fuchs

Poster

22ème Congrès SFP Marseille 2013
1-5 Juillet 2013
Amplifying at high energy short laser pulses using SBS-based plasma amplifiers

Forum ILP 2014, ''Laser & Plasma'', 2 au 7 février 2014, Orcières, France.
Improvement of neutron sources produced by ultra intense laser using a laser-triggered
micro-lens
L. Vassura, D. P. Higginson, F. Negoita, D. Bleuel, J. A. Green, M. M. Gugiu, F. Hannachi, H. Petrascu, D. Pietreanu, A. M. Schroer, M. Tarisien, S. Kar, M. Borghesi, O. Willi, P. Antici and J. Fuchs

NIF and JLF User meeting, 10 au 13 février 2014, LLNL, Livermore, USA.
Improvement of neutron sources produced by ultra intense laser using a laser-triggered micro-lens
L. Vassura, D. P. Higginson, F. Negoita, D. Bleuel, J. A. Green, M. M. Gugiu, F. Hannachi, H. Petrascu, D. Pietreanu, A. M. Schroer, M. Tarisien, S. Kar, M. Borghesi, O. Willi, P. Antici
and J. Fuchs